Title
High Performance Dispenser Printed Thermoelectric Generators

Author
Madan, Deepa

Publication Date
2013

Peer reviewed|Thesis/dissertation

High Performance Dispenser Printed Thermoelectric Generators

by

Deepa Madan

A dissertation submitted in partial satisfaction of the
requirements for the degree of
Doctor of Philosophy

in

Mechanical Engineering

in the

Graduate Division
of the
University of California, Berkeley

Committee in charge:

Professor Paul K. Wright, Chair
Professor James W. Evans
Professor Lisa A. Pruitt

Fall 2013

High Performance Dispenser Printed Thermoelectric Generators

Abstract

High Performance Dispenser Printed Thermoelectric Generators

by

Deepa Madan
Doctor of Philosophy in Mechanical Engineering

University of California, Berkeley

Professor Paul K. Wright, Chair

Thermoelectric generators can potentially be used to generate electricity from this low-grade waste heat and play an important role in powering the condition monitoring sensors. This work presents a novel method to synthesize thermoelectric materials to print scalable thermoelectric generator (TEG) devices in a cost effective way. The main focus of this work is performance advancements of dispenser printed composite thermoelectric materials and devices. Thermoelectric device design for condition monitoring applications, novel composite thermoelectric materials and cost effective and scalable manufacturing methods are foundational aspects of this work.

WSNs are a promising technology for ubiquitous, active monitoring in residential, industrial and medical applications. A current bottleneck for widespread adoption of WSNs is the power supplies. While the power demands can be somewhat alleviated through novel electronics, any primary battery will have a finite lifetime. This can pose a major problem if the network is large or the nodes are located in difficult to reach areas. Battery replacement is thus undesirable, costly, and inefficient for large-scale deployments of WSNs. Thermal energy is an attractive option to power WSNs due to the availability of low-grade ambient waste heat sources.

TEGs provide solid-state energy by converting temperature differences into usable electricity. These solid-state TEGs have great appeal due to their silent nature, have no moving parts and are CO_2 emission free. In order to be used for powering the condition monitoring WSNs, the TEG should be able to provide certain average power at desired voltage levels. Based on heat transfer TEG design, high voltage output requires large number of couples packed in a small area in addition to high Seebeck coefficient and high temperature difference across the device.

The performance of TEGs devices depends on both material properties and device geometry. The efficiency of TEG is governed by the dimensionless figure of merit, ZT, which depends on material properties. It has been challenging to increase ZT beyond

1 for commercial thermoelectric materials like Bi_2Te_3 as n-type and $Bi_{0.5}Sb_{1.5}Te_3$ as p-type, since the thermoelectric parameters of ZT are generally interdependent. There are challenges on the device design side as well. The electrical resistance and the temperature difference across the device depend on the element length of the device. Electrical resistance increases with increase in element length resulting in lower power output. Temperature difference across the device increases with increase in element length resulting in higher power output. Therefore, a trade-off occurs between device element length and power output, which ultimately depend on the TEG application. Therefore, an application specific optimized device length is required to maximize power output.

Devices, utilizing waste heat to generate power, should be low cost in order to be competitive. Traditional pick and place methods to manufacture TEG devices are labor, materials and energy intensive. Whereas, the micro-fabrication technology involves expensive and complicated processes like lithography and thin-film deposition and is limited to micro-scale regime. These methods have limited cost-effective scalability for manufacturing of application-specific TEGs. The limitations of the commonly used manufacturing technologies provide an opportunity for additive manufacturing methods such as direct-write printing. Printing utilizes additive processing steps, thus reducing materials waste and cost per unit area. It is an automated process that can be used to print high-aspect-ratio devices with minimum labor.

Printing of high-aspect-ratio TEG devices requires thermoelectric materials that are readily synthesized, air stable, and solution-process able to create patterns on large areas. In this regard, polymer thermoelectric composites are very attractive, as they require relatively simple manufacturing processes. While the ZT of inorganic composite materials may be lower than that of conventional materials, the reduction of manufacturing costs associated with printing is significant. As a result, the cost of energy generated from TEGs is improved through printed manufacturing. In this work, we utilize a custom developed dispenser printer to print high-aspect-ratio planar single-element TEGs. Off the shelf, Bi_2Te_3 and Sb_2Te_3 were chosen as the starting thermoelectric material because of high ZT values at room temperature. The maximum ZT at room temperature for an n-type Bi_2Te_3-epoxy composite and p-type Sb_2Te_3-epoxy composite cured at 250 °C was 0.16 and 0.18. Mechanical alloy and additives helped to improve the ZT for n and p-type thermoelectric composite materials to 0.2 and 0.18 respectively. Single element n-type planar prototype device was printed on a custom designed flexible polyimide substrate to form a TEG. The device produced 25μW at 0.23mA and 109mV for 20K temperature difference. These results indicate an areal power density of 130μW/cm^2, which is quite close to ideal power density 135μW/cm^2. Similarly p-type planar prototype device produced

20.5μW power at 0.15mA and 130mV for 20K temperature difference and areal power density of 150μW/cm^2.

We have explored Bi as n-type thermoelectric composite material as it is easily and cheaply available and its toxicity is less as compared to commonly used thermoelectric materials like Bi_2Te_3. We present a unique way of fabricating circular TEGs using dispenser-printing methods, which can be easily mounted on hot surface or wrapped around pipe carrying hot fluid to generate electricity to power condition monitoring sensors. In order to realize practical thermoelectric devices, both p-type and n-type elements connected in series are essential to achieve reasonable efficiency. Therefore, Bi-epoxy has been used as n-type composite thermoelectric material and MA $Bi_{0.5}Sb_{1.5}Te_3$ with 8wt% extra Te epoxy composites as p-type thermoelectric material to print circular TEGs. The maximum power output of 130μW at 70K temperature difference is achieved for a 10-couple device that resulted in measured power density (1230μW/cm^2).

The TEG device design was designed based on n and p-type composite thermoelectric film properties and optimized thermo-element leg length obtained was 3.5mm. The Flexible PCB consisting of nickel and gold plated copper traces on a flexible polyimide substrate was built by Rigiflex Technology Inc. Thick gold plated nickel and copper metal contacts resulted in reduced electrical contact resistance between metal contacts and printed TE elements. Flexible polyimide has low thermal conductivity that helps to maintain temperature difference across the device, electrical insulation helps to separate the gold contacts and high temperature tolerance make curing feasible for printed elements at high temperature. The 50-couple prototype device produced a power output of 33μW at 0.75mA and 43mV for a temperature difference of 20K resulting in a device areal power density of 280μW/cm^2. TEGs were mounted on hot surface pipes and without controlling the cold side temperature; power measurements with variable load resistance were done. At 100 °C hot surface temperature, 33μW of maximum power has been obtained. Power generated by these TEG devices is sufficient to charge batteries used in condition monitoring WSNs on the hot surfaces of equipment. While the efficiency of printed thermoelectric composites is not as high as that of some state-of-the-art materials with high figure of merit, the results are encouraging. The ease of processing and device fabrication with printed materials provides deployment advantages over such materials.

I will forever be thankful to my eternal father for instilling a desire and paving my way to follow my dreams. I dedicate this thesis to HIM.

Contents

List of Figures

List of Tables

Acknowledgments

I feel incredibly proud to be a part of the University of California at Berkeley, and such a supportive and cooperative research group. I feel blessed for all the encouragement, resources and guidance I received from many wonderful people here.

In particular, I would like to express my heartfelt gratitude to my dissertation chair Paul Wright for his valuable advice, enduring support, and confidence in me. I am eternally grateful to him for providing the golden opportunity to pursue PhD under his supervision. Without his constant encouragement this dissertation would not have become what it is today.

James Evans provided his valuable insights to steer this project in the right direction. I am afraid I do not have words to express my thanks for his valuable research advice and guidance to make this project successful. It is unimaginable how much time and effort he had to spend to discuss, proofread, and correct all my work.

I would like to extend my sincere thanks to Lisa Pruitt for providing valuable comments on my research as my orals and dissertation committee member.

Before this dissertation started to be imagined, I was introduced to Paul Wright by Ramamoorthy Ramesh for a research staff position. I extend my thanks to him.

I owe big thanks to my fellow colleague at BMI lab. Mike Koplow and Alic Chen provided the necessary training by pouring all their relevant knowledge about this project on me. I am especially thankful to Alic Chen for his help, advice, and thought provoking discussions. I am also thankful to Zuoqian Wang, my fellow lab member and a very good friend, for his innovative ideas, and supportive gesture that greatly contributed to this dissertation. I would also like to extend my thanks to Kevin Huang, Brian Mahlstedt, Jonathan Brown, Michael Nill, Rich Winslow, Jay Keist, Christine Ho, and Rei-Cheng Juang for their contribution to this dissertation. Dan Chapman deserves big thanks for providing all the needed resources in a smooth and timely manner. I wish all of you very successful careers.

The decision to undergo a doctoral study was only possible with the love, support, appreciation, and encouragement of my loved ones. I express my deepest gratitude to my parents and siblings for showering their unconditional love, and having faith in my abilities. It was Shubhranshu, my husband, who encouraged me to take the challenge of a doctoral study. He is a strong pillar of my life. Without his love, support, and constant guidance this dissertation would not have materialized. I am thankful to God, for showering his love in the form of my darling daughter, Sakshi. I am really blessed to have you as my daughter. You are a true source of joy for us. I wish you all the success in your life.

I hope I can pay forward to society whatever good things I have received from my advisors, my fellow colleagues, and from my loving family.

Chapter 1

Wireless Sensor Networks and Thermoelectricity

1.1 Introduction

Wireless sensor networks (WSNs) are an autonomous monitoring technology for residential, industrial and medical applications. Batteries have traditionally been used to meet the low power requirements of these WSN devices. However they have finite lifetimes that are often less than the programmed life of the WSN. Battery replacement is thus undesirable, costly, and inefficient for large-scale deployments of WSNs. To provide power for WSNs, this research considers the use of low-grade waste heat sources in residential and commercial settings. Thermoelectric generator (TEG) devices are attractive potential power sources because they directly convert thermal gradients into electrical power, providing power while temperature gradients are present. This chapter introduces WSNs and thermal energy harvesting. An introduction of the thermoelectric effects and a summary of the best available thermoelectric materials for low waste heat application is also presented.

1.2 Wireless Sensor Networks

WSNs are devices that perform measurements in their specific environment and are not connected to the acquisition unit. The typical characteristics of WSN are autonomous power supplies, and the ability to measure and transmit data. Research has shown that WSNs can be used for measurement of quantities in mobile devices, protected environments, and places where electrical energy is absent [74, 100]. WSNs

are particularly useful in places where wires are difficult to use as connection between the sensor and the data acquisition unit. For example, they can be used in implantable devices [44, 84], rotating machinery [45], and sealed environments [109]. In the food industry, WSNs can improve the shelf-life labels by letting both consumers and producers know when the packaged food is fresh and safe. In some fields, sensors are used in broad temperature ranges, extreme humidity, and corrosive conditions [19, 20, 38, 90, 91]. Structural health monitoring of bridges, pipes, and buildings [66], and monitoring of climate conditions and pollution are some common examples [61]. WSNs can also be used to detect leaks and emissions in a co-generation plant, refinery, or chemical plant [11, 12].

WSNs are a collection of small, wireless platforms connected into a distributed local area network. Each platform, also known as a node, consists of a radio transceiver, a micro-controller, an energy source, and one or more sensors and/or actuators depending on the application [37, 97]. Commercial WSNs typically use primary batteries as the power source [1, 29]. WSNs usually have average power consumptions in microwatts. It is due to their low power sleep states and short transmit pulses. However, the peak power consumption can be high (in milliwatts) [30]. The lifetime of the node depends on the duty cycle, and the amount of data being sensed and transmitted. Primary batteries often have finite lifetime that may be less than the life of the node. Additionally, primary batteries can be bulky and heavy. Battery replacement is undesirable, expensive, and inefficient for large-scale use of WSNs. Power sources that are self-sustained and can provide perpetual power to the nodes are desirable. A long life and small size are particularly useful for deployment of WSNs in hard to access areas.

Energy scavenging devices that scavenge energy from their environment are being developed as power sources for WSNs [71, 77]. Thermal energy harvesting is a good option to power WSNs due to the availability of low-grade waste heat sources in residential, industrial, and other places. Thermoelectric power generation provides solid-state conversion of heat into electrical power by utilizing the Seebeck effect. The next section describes thermoelectric effects, including the Seebeck effect.

1.3 Thermoelectric Effects

Thermoelectric effects describe the interaction and conversion between heat and electricity in solids, which can be summarized by Seebeck, Peltier, and Thomson effects. Together these three effects are known as thermoelectric effects [54, 78]. Based on these effects, thermoelectric devices have been developed and deployed for power generation, temperature sensing, and cooling [15].

The Seebeck effect is the voltage developed when the junction of two dissimilar materials are kept at different temperatures as shown in figure 1.1. The measured output voltage (V) is approximately proportional to the temperature difference ($\triangle T$) between the two junctions [54].

$$V = \alpha_{ab} \triangle T$$

α_{ab} is the proportionality constant and is known as the Seebeck coefficient. α_{ab} is a relative quantity and is associated with the properties of materials A and B. The unit for α_{ab} is V/K and its value is positive if the majority charge carriers are holes, and negative if they are electrons. Generally, insulators have large Seebeck coefficients followed by semiconductors, semi-metals and metals.

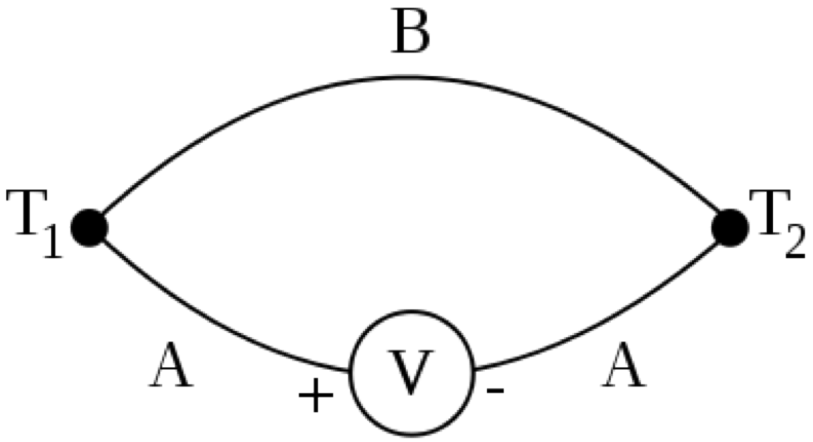

Figure 1.1: Schematic of the Seebeck effect.

When a temperature difference is applied across a material, a carrier concentration gradient develops. Charge carriers are generated at the hot side, and are diffused to the cold side creating an internal electric field. This electric field resists further carrier diffusion from the hot side to the cold side. The steady state electrochemical potential difference between the two ends at different temperature is the Seebeck voltage [78]. A thermoelectric device operating in the Seebeck mode converts heat into electricity, and is known as a thermoelectric generator (TEG).

Instead of applying a temperature difference across the TEG, voltage can also be applied to the circuit. Electric current that flows around the circuit will result in heat absorption at one junction and heat dissipation at the other due to thermal transport by moving electrons. Consequently, one junction will become cold and other will become hot. The total heat absorption (or dissipation) Q is given by

$$Q = \pi_{ab} I$$

where π_{ab} is the Peltier coefficient and I is the electric current in the circuit.

The Seebeck effect and the Peltier effect can only be observed in a system that consists of at least two different materials. However, the absorption (or dissipation) of heat along a single material can occur when the material is subjected to a temperature difference and electric current simultaneously. The total heat absorption (or dissipation) is given by

$$Q = \beta I \triangle T$$

where β is referred to as the Thomson coefficient. Together these effects are known as thermoelectric effects [78].

1.4 Thermoelectric Materials

A dimensionless figure of merit (ZT) is commonly used to assess the effectiveness of the thermoelectric material. It is defined as

$$ZT = \frac{\alpha^2 \sigma}{\lambda} T.$$

Efficient thermoelectric materials should have high Seebeck coefficients (α) to provide sufficient voltages, high electrical conductivities (σ) to allow for electron transport, and low thermal conductivities (λ) to minimize heat losses and maintain good temperature difference across the device [78]. These properties depend on the carrier concentration.

Using the electron transport models,[83] the Seebeck coefficient can be approximately written as

$$\alpha = \frac{8\pi^2 k_B^2}{3eh^2} m^* T \left(\frac{\pi}{3n}\right)^{\frac{2}{3}} \tag{1.1}$$

where k_B is the Boltzmann constant, e is the electron charge, h is Planck's constant, n is the carrier concentration, m^* is the effective mass of the charge carrier, and T is the temperature. It is clear from the above expression that a high Seebeck coefficient requires low carrier concentration.

The electrical conductivity can be described as

$$\sigma = ne\mu = \frac{1}{\rho} \tag{1.2}$$

where ρ is the electrical resistivity, and μ is the carrier mobility. Electrical conductivity increases with increase in the carrier concentration.

From equation 1.1 and equation 1.2, it is clear that it is very difficult to have high Seebeck coefficient and electrical conductivity at the same time. Figure 1.2 shows the variation of Seebeck coefficient and electrical conductivity versus carrier concentration. Seebeck coefficient decreases with increase in the carrier concentration whereas electrical conductivity increases with increase in the carrier concentration. It is desired to have high power factor, $\alpha^2\sigma$, in order to achieve high ZT. The power factor is typically optimized through doping of narrow-band semiconductor materials to adjust the carrier concentration. The highest power factor is typically achieved for carrier concentrations between 10^{19} and 10^{21} per cm^3 [83, 92].

In addition to high Seebeck coefficient and high electrical conductivity, a low thermal conductivity, λ, is desired for good thermoelectric materials. Thermal conductivity of a material can be written as

$$\lambda = \lambda_e + \lambda_l$$

where λ_e is the electronic thermal conductivity and λ_l is lattice thermal conductivity of the material. Both electrons and phonons (lattice vibrations) contribute to the thermal conductivity of a material. The electronic thermal conductivity results from charge carriers transporting heat, and is directly related to the electrical conductivity through the Wiedemann-Franz law:

$$\lambda_e = L\sigma T = ne\mu LT \tag{1.3}$$

where L is Lorentz factor for free electrons [10]. Equation 1.3 implies that high electrical conductivity materials have high thermal conductivity as well. The three thermoelectric properties α, σ, and λ are interdependent. Therefore, it is hard to change only one property without changing the others. For example, increasing the number of charge carriers not only increases electrical conductivity but also increases thermal conductivity and decreases Seebeck coefficient. The most efficient thermoelectric materials with the highest ZT values are doped semiconductor materials with high power factors in conjunction with low lattice thermal conductivity [72, 83]. Moreover, electrical conductivity and carrier concentration can be easily changed for semiconductors by changing the doping type and doping concentration. The contribution of electrons to thermal conductivity is not dominant for semiconductors. Therefore, a change in doping concentration has a small effect on thermal

conductivity. Optimization of doping concentration is an important aspect of developing thermoelectric materials.

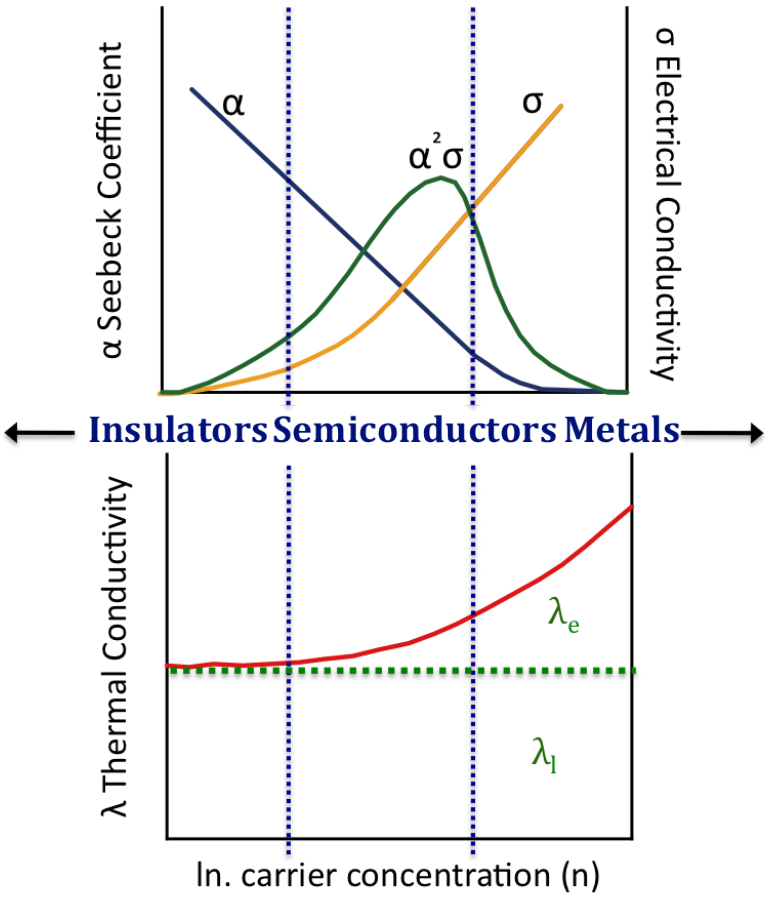

Figure 1.2: Thermoelectric material properties as a function of carrier concentration. Adapted from [78].

Figure 1.3 shows the figure of merit for various n-type and p-type state of the art thermoelectric materials as a function of temperature. The individual materials properties and the figure of merit are highly dependent on the operating temperature of the device. Over the last several decades, the non-dimensional figure of merit has remained at a maximum value of about one. $Bi_2Te_3$and Sb_2Te_3-based alloys are considered as the most ubiquitous thermoelectric materials for near room temperature applications with ZT around one. First investigated in the 1950's [23, 76] as

promising thermoelectric materials, Bi_2Te_3 and its alloys are still the predominant thermoelectric materials today [83, 92, 94].

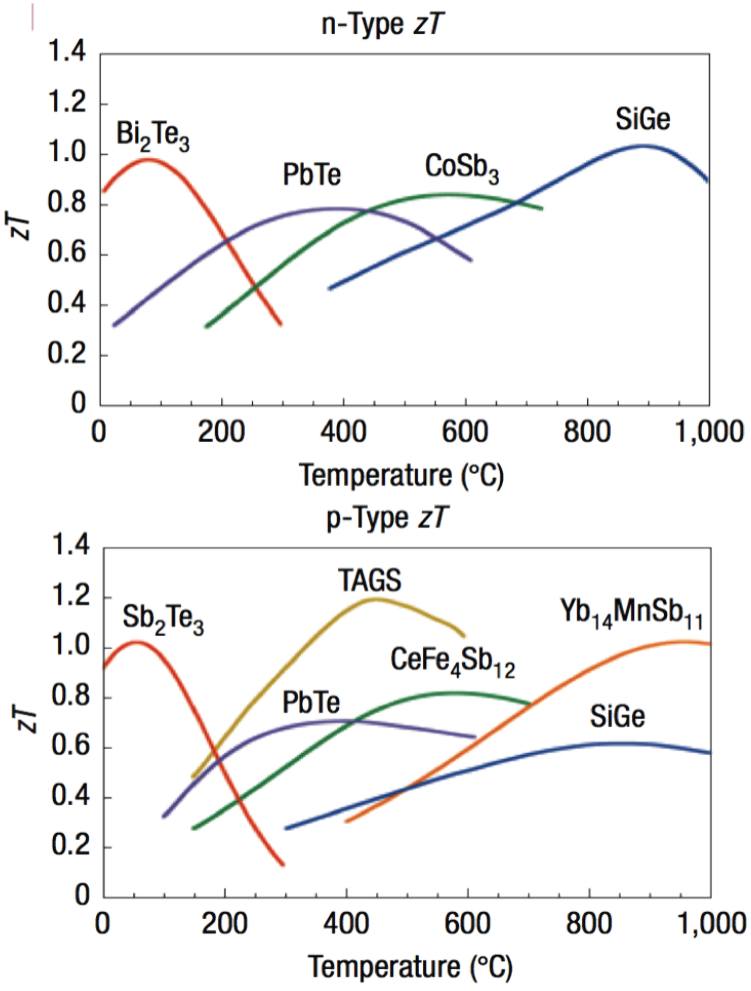

Figure 1.3: ZT as a function of operating temperature for n-type and p-type state of the art thermoelectric materials. Adopted from [83].

Recent research has led to the discovery and characterization of a new generation of high temperature thermoelectric materials: skutterudites, thin-film superlattice materials, quantum well materials, and PbAgSbTe (LAST) compounds and their derivatives [28]. These materials have either demonstrated ZT of ~1.5-2 or shown great promise for higher ZT approaching 3 or 4. Quantum well materials include

0-dimensional (0-D) dots, 1-dimensional (1-D) wires and 2-D thin-film materials [16, 60, 93]. While these developments have only recently emerged from various research institutions, the potential for their future adoption in commercial technologies is promising. For powering wireless sensor nodes from thermal gradients near room temperature, Bi_2Te_3, Sb_2Te_3, and $Bi_{0.5}Sb_{1.5}Te_3$ are the best known bulk materials. In this work, we use these materials and optimize their properties to achieve high ZT and fabricate high performance TEGs.

Chapter 2

Thermoelectric Generator Design and Manufacturing

2.1 Overview

The main focus of this research is to develop novel thermoelectric materials which can be easily printed using dispenser printer to fabricate a thermoelectric generator (TEG). These TEGs can be used for powering condition monitoring wireless sensor nodes used in residential and industrial buildings. It is typically assumed in the existing literature that a constant temperature difference is available across the device. However, in practical situations such as exhaust pipes, engine manifolds of automobiles, and steam pipes it is not possible to maintain the ambient side temperature. Therefore, it is difficult to maintain constant temperature difference between the hot and cold surfaces without using any external power source. In these scenarios the use of TEGs to generate useful energy requires examination.

This chapter introduces some basic concepts about TEGs, followed by heat transfer modeling to find the actual available thermal energy from low waste heat sources. Based on the actual temperature difference available across the TEG, a basic device design is investigated to optimize power output. A review of commonly used manufacturing methods and their shortcomings, to produce an optimized device design TEG, is presented. Finally, an additive manufacturing technique is proposed, for maximizing power output of these TEGs.

2.2 Operating Principles of TEG

TEGs function based on the Seebeck effect, which has been discussed in chapter 1. Figure 2.1 shows a schematic for a thermoelectric couple. In this unit cell, an n-type element and a p-type element are used. As shown in the figure, the n and p elements are connected electrically in series and thermally in parallel, with a metal connecting the elements and the gap between them. When a temperature gradient is applied across two dissimilar materials, an open circuit voltage can be measured. The open circuit voltage of the generator can be written as

$$V_{op} = m\alpha_{n-p}\triangle T_g \tag{2.1}$$

where m is the number of couples, α_{n-p} is the Seebeck coefficient, and ΔT_g the temperature drop across the generator.

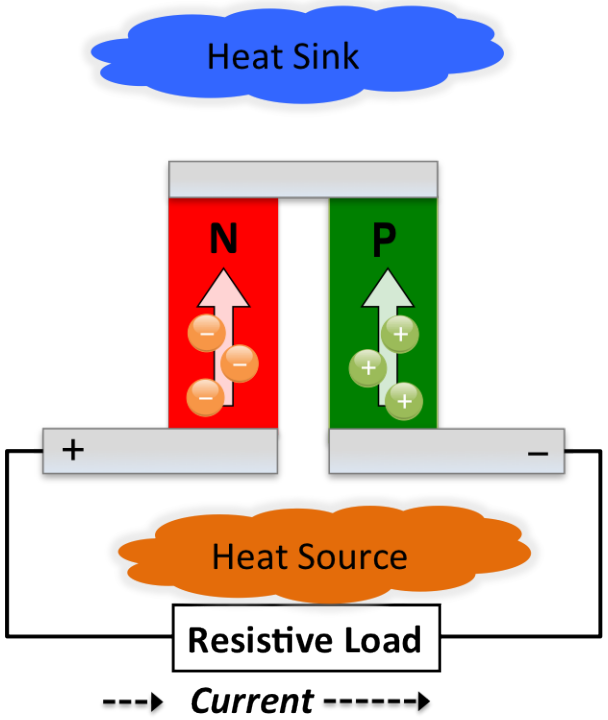

Figure 2.1: Basic configuration for a thermoelectric device.

The devices are configured in this way to ensure that holes and electrons move in the opposite direction in the electric circuit, but in the same direction in the thermal

circuit as shown in Figure 2.1. The voltage generated across the n and the p-type adds up since the elements are connected electrically in series. A large number of n and p-type elements are used to enhance the voltage output. Figure 2.2 shows an image of a typical thermoelectric device. Ceramic substrates are used to maintain good temperature difference across thermoelements, and electrical insulation between thermoelements and metal contacts.

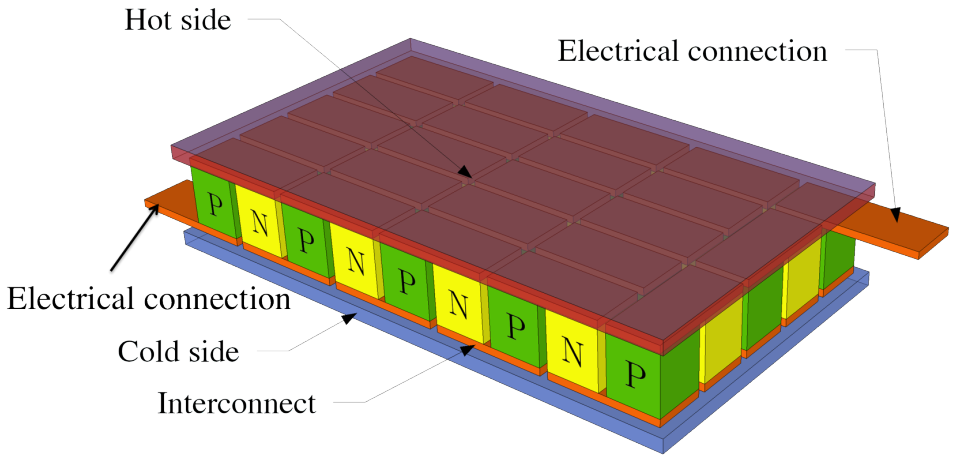

Figure 2.2: Schematic of a thermoelectric device.

2.3 Heat Transfer Modeling

In designing TEGs for autonomous wireless sensor network devices, it is important to know the temperature difference available from the low waste heat in residential and industrial applications. A survey was conducted to measure the temperature difference available around pipes carrying hot fluid in the University of California, Berkeley co-generation plant. The temperature differences vary significantly depending on physical location of the pipe, type and thickness of insulation around the pipe, and ambient environments. Temperature difference in the range of 30-50K was observed around pipes carrying hot fluids.

In research on TEGs, it is common to maintain the hot and cold side temperatures using external power sources. However, in real situations (such as exhaust pipes, engine manifolds of automobiles, and steam pipes) it is not possible to maintain the ambient side temperature. In these situations the use of TEGs to generate useful energy requires examination of actual temperature difference across the TEGs.

Figure 2.3 shows the scenario where temperature difference across hot and cold side is the same as the temperature difference across the device. However, the actual temperature difference available across the TEG device may be different. Figure 2.4 shows the schematic of this situation.

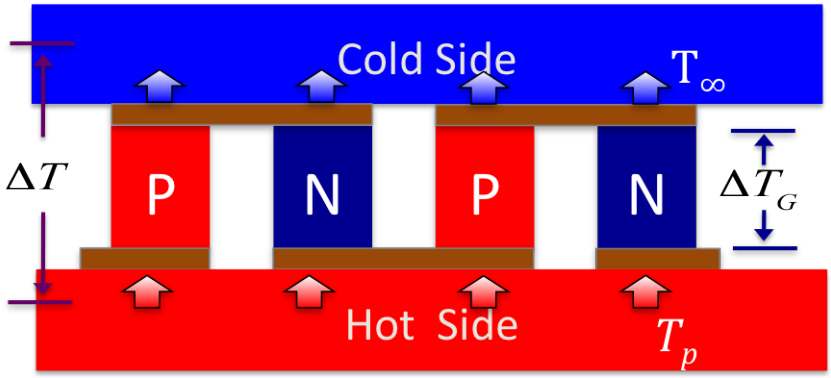

Figure 2.3: Schematic of a thermoelectric device under applied temperature difference.

Consider a differential element dx. At steady state, the amount of heat going in is equal to the amount of heat going out. Although heat in is only through conduction the heat out is due to conduction as well as convection. For first order approximation, natural heat transfer coefficient is assumed to be constant and heat conduction is assumed to be one dimensional. The following analysis has been adapted from [35]. The energy balance equation can be written as

$$q_x = q_{x+dx} + dq_{conv} \tag{2.2}$$

where

$$q_x = -\frac{(kA_c dT)}{dx},$$

$$dq_{conv} = hdA_s \left(T - T_\infty\right),$$

$$q_{x+dx} = -kA_c \frac{dT}{dx} - k\frac{d}{dx}\left(A_c \frac{dT}{dx}\right) dx$$

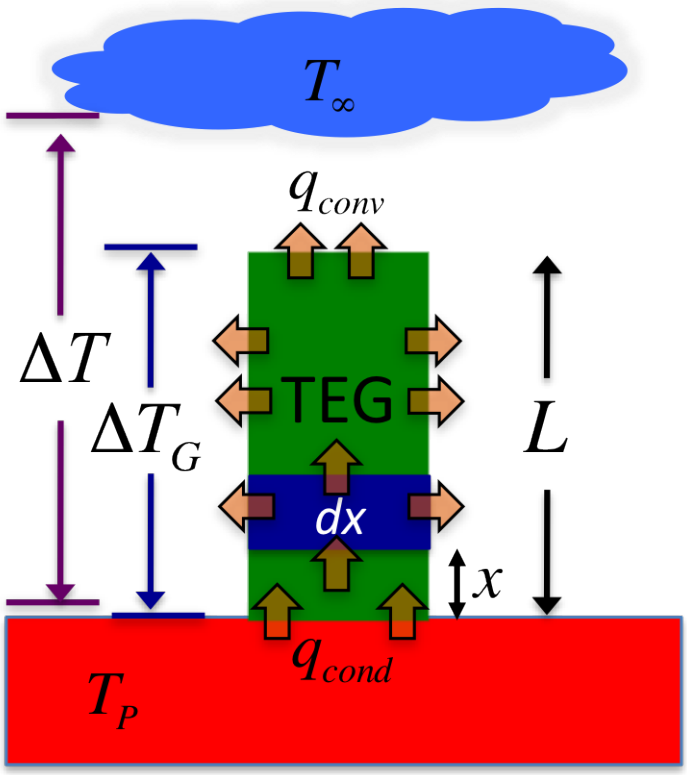

Figure 2.4: A thermoelectric device under applied temperature difference in the practical situation.

where A_c is the cross-sectional area and is constant, $A_s(= Px)$ is the surface area measured from base to x, and P is the thermoelement perimeter.

Substituting all these values into energy balance equation and canceling the common terms, we get

$$\frac{d}{dx}\left(A_c\frac{dT}{dx}\right) - \frac{h}{k}\frac{dA_s}{dx}(T - T_\infty) = 0$$

or,

$$\frac{d^2T}{dx^2} + \left(\frac{1}{A_c}\frac{dA_c}{dx}\right)\frac{dT}{dx} - \left(\frac{1}{A_c}\frac{h}{k}\frac{dA_s}{dx}\right)(T - T_\infty) = 0.$$

For the uniform rectangular fin shown in figure 2.4 the base temperature is $T = T_P$ and it extends to fluid of temperature $T = T_\infty$.

Since

$$\frac{dA_c}{dx} = 0;\ \frac{dA_s}{dx} = P$$

the above equation reduces to

$$\frac{d^2T}{dx^2} - \frac{hP}{kA_c}\left(T - T_\infty\right) = 0. \tag{2.3}$$

A new parameter, θ, is defined to simplify the equation 2.3

$$\theta = T\left(x\right) - T_\infty.$$

Equation 2.3 simplifies to

$$\frac{d^2\theta}{dx^2} - m^2\theta = 0 \tag{2.4}$$

where

$$m^2 = \frac{hP}{kA_c}.$$

Equation 2.4 is a linear homogenous second order differential equation and its general solution is given by

$$\theta\left(x\right) = C_1 e^{mx} + C_2 e^{-mx}. \tag{2.5}$$

To evaluate the constants C_1 and C_2, it is necessary to specify the boundary conditions. In our case the boundary conditions are

1. The temperature at the base of the TEG, which is in contact with the hot surface is given by, $T = T_P$ at $x = 0$. Therefore,

$$\theta_P = T_P - T_\infty = C_1 + C_2.$$

2. Only convection takes place at the tip, at $x = L$, of the TEG

$$-kA_c\frac{dT}{dx} = hA_c\left\{T\left(L\right) - T_\infty\right\}$$

or,

$$h\theta L = -k\frac{d\theta}{dx}.$$

Substituting this value into the equation 2.5, we get

$$h\left(C_1 e^{mL} + C_2 e^{-mL}\right) = km\left(C_2 e^{-mL} - C_1 e^{mL}\right).$$

Solving for C_1 and C_2, we get

$$\frac{\theta}{\theta_P} = \frac{cosh\, m\,(L-x) + (h/mk)\, sinh\, m\,(L-x)}{cosh\, mL + (h/mL)\, sinh\, mL} \equiv S. \tag{2.6}$$

Substituting θ and θ_P in equation (2.6), we get

$$T = T_\infty + (T_P - T_\infty)\, S$$

It is clear from equation 2.6 and figure 2.5 that there is relationship between temperature (T) and position in the leg (x).

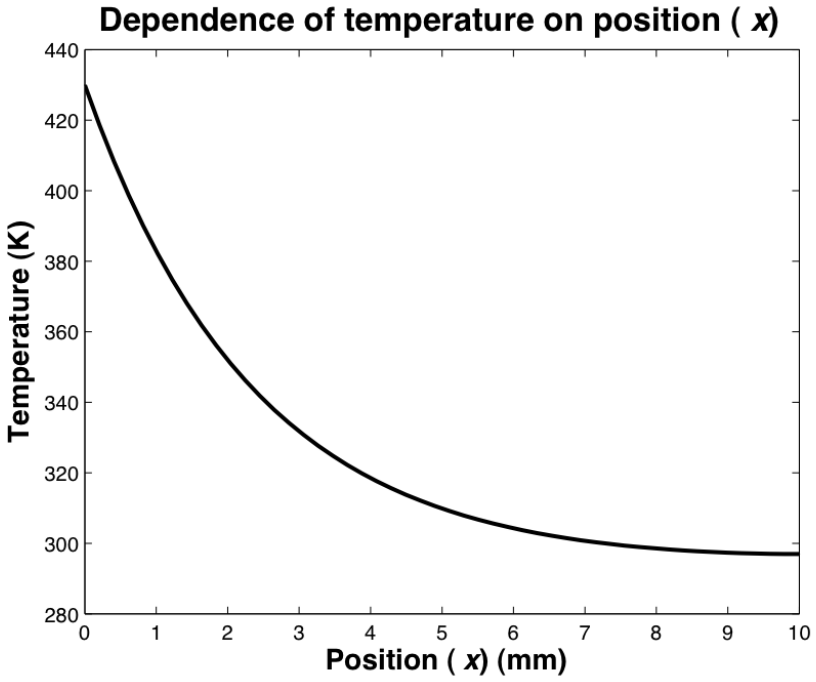

Figure 2.5: Dependence of temperature on position.

Figure 2.6 shows that the temperature difference keeps on increasing with the leg length of TEGs. In the next section, we will see that it is not possible to keep on increasing the leg length to attain highest temperature difference $\triangle T_G (= T_P - T)$.

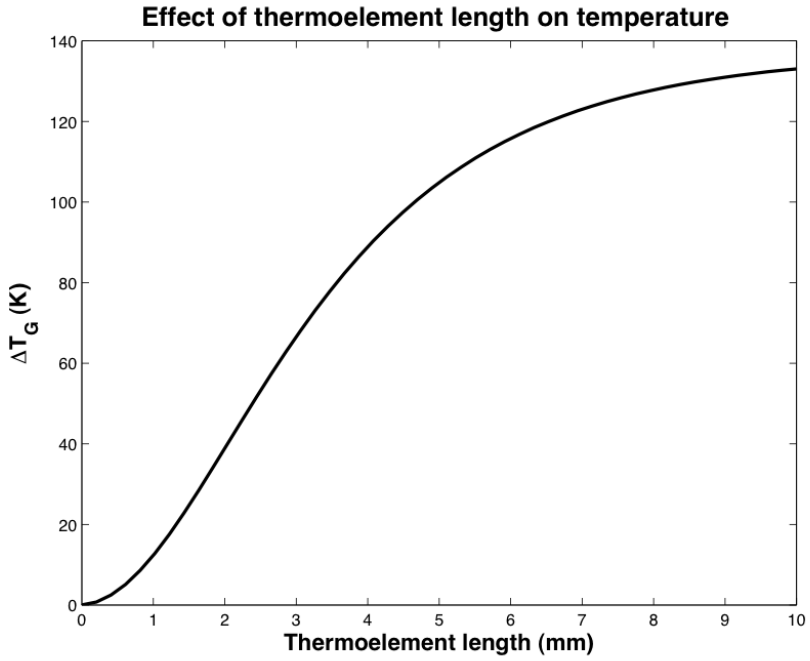

Figure 2.6: Dependence of temperature difference on thermo-element leg length.

2.4 Thermoelectric Generators Design

The temperature difference and the leg length of the TEG is related to its power output. Since the maximum power occurs at matched load resistance, the closed circuit voltage at maximum power is half the open circuit voltage. Power output of a thermoelectric generator can be approximated as,

$$P_{max} = \frac{V_{op}^2}{4R_{in}} \tag{2.7}$$

where V_{op} is given by equation 2.1 and R_{in}, the internal resistance of the device, is given as

$$R_{in} = \rho \frac{mL}{A}. \tag{2.8}$$

ρ is the electrical resistivity of the material, L is the thermo-element length in the direction of heat flow, and A is the cross-sectional area of the element. This assumes that the resistances of the metal interconnects and contact resistances are negligible.

Substituting V_{op} from equation 2.1, and R_{in} from equation 2.8 in equation 2.7, we get

$$P_{max} = \frac{m\alpha_{n-p}^2}{8L}\sigma A \triangle T_g^2. \tag{2.9}$$

The power output of a TEG is a function of the thermoelectric materials properties. It also depends on the number of couples and the temperature difference across the generator. Therefore, the TEG device design is dependent on both the geometry and the thermoelectric materials properties [21, 88]. The device electrical resistance must be low to maximize power output, requiring short element lengths. However, small element lengths pose difficulties in maintaining temperature differences across the device. Therefore, a trade-off occurs between the device element length and the power output, which ultimately depend on the TEG application. The variation of power output with thermo-element leg length is calculated using equation 2.6, equation 2.9, and the standard bulk materials properties of Bi_2Te_3. The cross-sectional area of the TEG device is assumed to be (0.5mm×100μm). Results are shown in Figure 2.7.

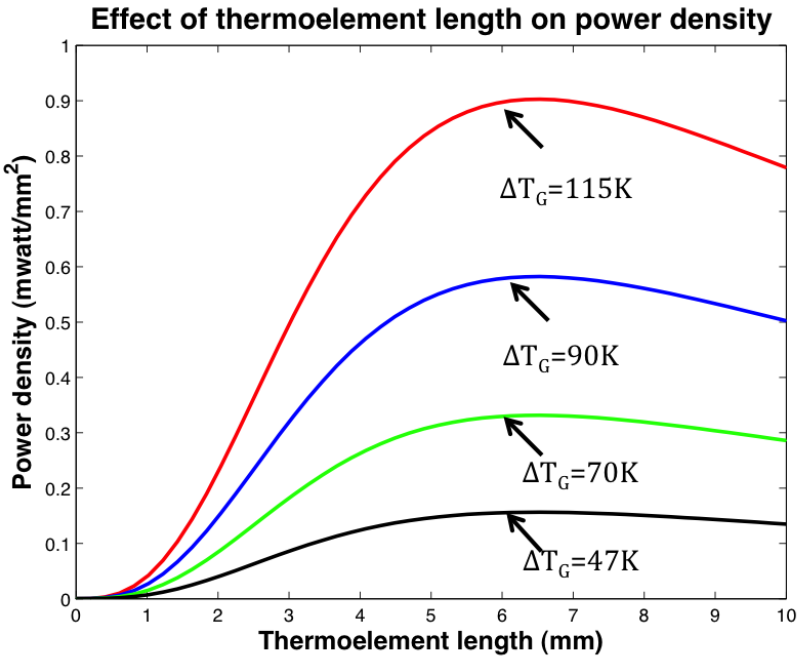

Figure 2.7: Variation of power density with thermo-element leg length.

From figure 2.7, it is clear that the maximum power occurs when the leg length is 6.5mm. Further increase in the leg length results in lower power output due to increase in the electrical resistance of the device. It can also be noted from figure 2.7 that the power output increases with increase in the temperature difference. However, as discussed in the previous section, the temperature difference also depends on the leg length. Therefore, power output ultimately depends on the leg length of the TEG. Thus, an optimal TEG requires high aspect ratio elements. To meet the wireless sensor network (WSN) voltage demand, TEGs require a large number of couples packed in a small area in addition to high Seebeck coefficient and high temperature difference across the device [98].

2.5 Existing Manufacturing Methods and Limitations

Having understood the design requirements, we now explore some commonly used manufacturing methods, and their limitations, to fabricate TEGs.

2.5.1 Bulk Device Manufacturing

In the manufacturing of bulk thermoelectric devices (Figure 2.2) n or p-type ingots are used to make thermo elements. These ingots may be produced using a single crystal Czochralski puller. Ingots are then cut into bars and diced into elements.The thermo elements made from ingots are bonded onto substrates with metal contacts (typically nickel plated copper) [55].

Since elements made from ingots are usually brittle fabrication of high aspect ratio TEGs is challenging. The cross-sectional area of the element is limited by the manufacturing process. This manufacturing technique is labor intensive. Most commercial manufacturers still use pick and place methods. As a result, full automation becomes difficult to achieve and the manufacturing costs are high. The bulk device manufacturing is limited to low-density arrays with low aspect ratios. This method has limited cost-effective scalability for manufacturing of application-specific TEGs.

2.5.2 Thin film Devices

Semiconductor manufacturing techniques have been used to overcome the size limitations of bulk manufacturing techniques. Micropelt has fabricated thin film thermoelectric elements using sputtered Bi_2Te_3 elements [5, 4]. It is not possible

to fabricate thermo-elements taller than a few microns using the thin film fabrication technique. Conventional micro-fabrication technology involves expensive and complicated processes like lithography and thin-film deposition and is limited to the micro-scale regime.

2.6 Additive Printing

The limitations of the available manufacturing technologies provide an opportunity for additive manufacturing methods such as a direct-write printing. Printing involves the deposition of synthesized thermoelectric inks, which consist of active TE materials in organic or polymer binders in slurry form. It eliminates the need for expensive processing steps such as lithography, chemical vapor deposition and etching. It utilizes additive processing steps, thus reducing materials waste and cost per unit area. It is easy to fabricate high aspect ratio and high density arrays using printing methods. Printing is also an automated process that requires minimal labor in scaled manufacturing.

Several researchers have previously investigated printed thermoelectric materials using different printing methods and ink recipes. Table 2.1 lists various materials properties for the previous printed thermoelectric references, which are described in this section. None of the inorganic thermoelectric materials thus far has shown figure of merits that rival bulk Bi_2Te_3 (ZT = 1). The pastes are cured or sintered at low temperatures (<300°C) and construction of the TEGs can be readily scaled to mass manufacturing. While the ZT of inorganic composite materials may be lower than that of conventional materials, the reduction of manufacturing costs associated with printing is significant. As a result, the cost of energy generated from TEGs is improved through printed manufacturing.

2.7 Dispenser Printing

For additive printing of the TEG, a dispenser printer was used. This dispenser printer was previously developed in the lab and has been used for the fabrication of solid-state capacitors [31], batteries [86], and printable magnetic materials [48]. Figure 2.8 shows an image and schematic of the dispenser printer. A brief summary of the design and specifications is presented. Details are available in the previously published literature [7]. The resolution of the printer stage is 0.03μm and the repeatability is 5μm. The resolution of the stage controller is 1μm. The printer can be used for deposition of inks in the viscosity range of 100-10,000cP. Typical feature

Materials-Polymer	ΔT	Papers	Power factor	Power density
PEDOT-PSS	30K	Bubnova (2011)	350μW/m-k^2	0.27μW/cm^2
Bi_2Te_3-Epoxy Sb_2Te_3-Epoxy	20K	Chen (2011)	150μW/m-k^2	75μW/cm^2
Sb-Ethylene Glycol Bi-Ethylene Glycol	5K	Weber (2006)	9.5μW/m-k^2	2μW/cm^2
Bi_2Te_3-Butadiene		Miyazaki (2003)	146μW/m-k^2	
$Bi_{0.5}Sb_{1.5}Te_3$- Polystyrene		Navone (2010)	6μW/m-k^2	
Cs_2CO_3-C_{60}		Sumino (2011)	20.5μW/m-k^2	

Table 2.1: Previous research related to printed thermoelectric slurries.

sizes of 10-200μm thickness can be printed using the printer. Process parameters such as shot pressure, tip size, rheology of the ink, and shot spacing can be used for optimization of feature size.

2.8 Conclusion

1. The actual temperature difference available across the device is different from the temperature difference available between hot and ambient side in low waste heat applications.

2. Based on this temperature difference available across the device, TEG device design has been proposed to optimize power output. High aspect ratio and high density array TEGs are desired.

3. Traditional pick and place thermoelectric designs lack the geometries and manufacturing scalability that can be found in printed device designs.

4. Thin film micro fabrication methods to fabricate TEGs involve expensive and complicated thin film deposition, lithography, and etching that can be easily substituted by cost effective additive manufacturing techniques.

5. A method for fabricating TEGs is proposed using dispenser printed techniques. Dispenser printer can be used to fabricate a flexible, scalable and high array density TEG device.

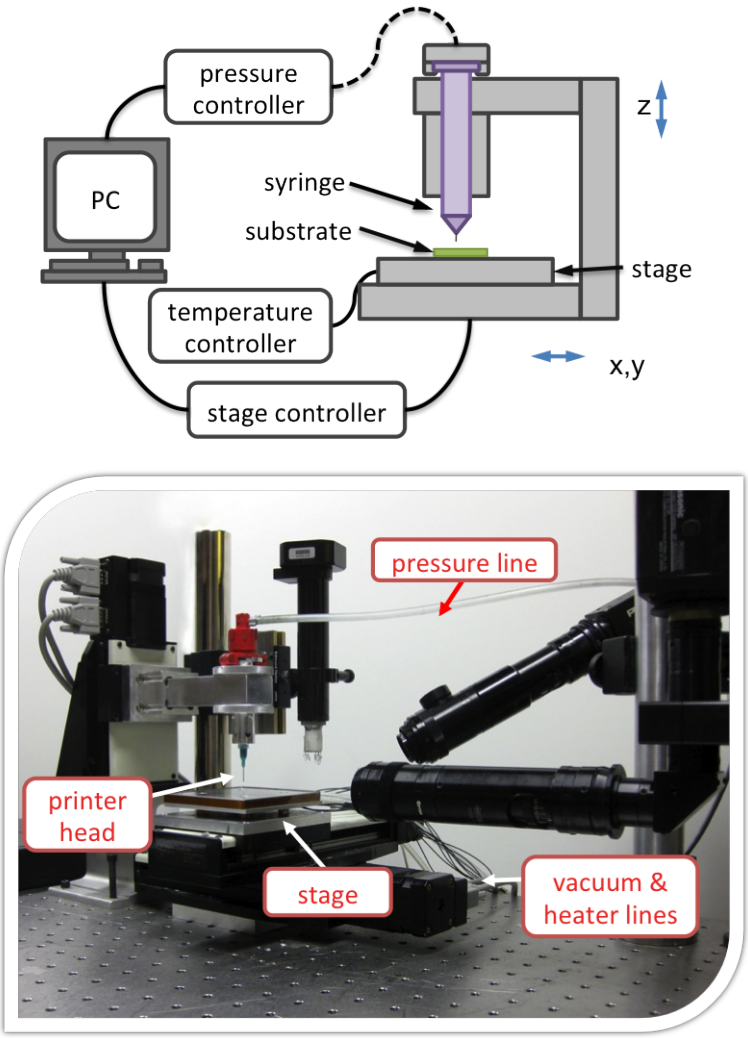

Figure 2.8: Schematic and image of dispenser printer.

Chapter 3

Printable Bi_2Te_3 and Sb_2Te_3 Composite Slurries

3.1 Overview

Printing of high-aspect-ratio TEG devices requires thermoelectric materials that are readily synthesized, air stable, and solution processable to create patterns on large areas. In this regard, polymer thermoelectric composites are very attractive, as they require relatively simple manufacturing processes. Because printed electronic materials are traditionally synthesized as composite materials, printable thermoelectric materials can be developed using established percolation theories and methods. This chapter focuses on the optimization of the synthesis and processing parameters to maximize the ZT for dispenser printed films.

3.2 Thermoelectric Composite Slurries

In order to fabricate thermoelectric devices using printing, printable thermoelectric materials must first be developed. Printing involves the deposition of synthesized thermoelectric inks, which consist of active thermoelectric materials in organic or polymer binders in slurry form[6, 58, 81, 98, 110]. Slurries provide easy flexible methods for producing composite materials. They are advantageous because they easily create homogenous mixtures and can be cured under low to moderate temperatures allowing for a wide range of substrate choices. Active particles consist of various conductive thermoelectric materials, while the polymer matrix acts as a binder [32, 49, 75, 89]. Figure 3.1 shows a schematic of ink processing and printing

steps. In the next section we discuss epoxy polymer as a binder, and Bi_2Te_3 and Sb_2Te_3 as active filler particles.

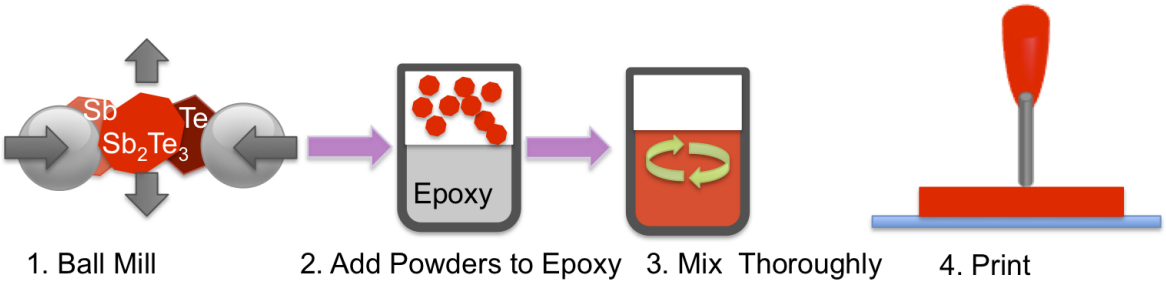

Figure 3.1: Ink making processing steps.

3.2.1 Epoxy Binders

Epoxy resin systems are proven polymer systems and are commonly used in commercially available electrically conductive adhesives for printed circuit boards (PCB) and thermal interface materials (TIM) [40, 49, 68, 73, 80, 101]. The epoxy matrix, when cured, provides the mechanical adhesion with minimal cure shrinkage and high mass loading [101]. The binder has a low thermal conductivity, which is desirable for thermoelectric materials, but does not aid in the electrical conductivity or Seebeck coefficient. The epoxy system used in this work was chosen particularly for its low viscosity and extended shelf-life[49, 53]. Relevant materials properties and the curing schedule with epoxy are listed in the results and discussion section of this chapter. The epoxy system was formulated based on the monomer diglycidyl ether of bisphenol f epoxy resin (chemical formula shown in figure 3.2) (EPON 862, Hexion Specialty Chemicals, Inc.) and methylhexahydrophthalic anhydride (MHHPA, Dixie Chemicals, Inc.) as the hardener. The ratio of epoxy-to-hardener was 1:0.85 based on the equivalent weight. 1-cyanoethyl-2-ethyl-4-methylimidazole (2E4MZCN, Sigma-Aldrich, Inc.) was used as the catalyst and 10-20 wt% of butyl glycidyl ether (Heloxy 61, Hexion Specialty Chemicals, Inc.) was employed in the resin blend as a reactive dilutant to adjust the viscosity of the slurry to the desired properties. Low percentages of organic solvents were also used to both extend the shelf-life of the epoxy system and adjust the viscosity for printing.

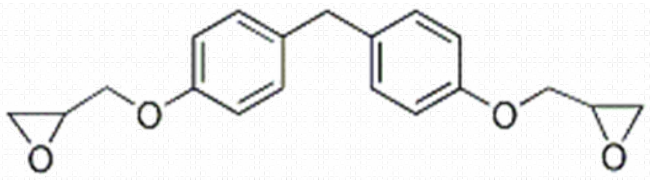

Figure 3.2: Bisphenol F diglycidyl ether epoxy (EPON862).

3.2.2 Active Particles

Bi_2Te_3 as n-type and Sb_2Te_3 as p-type are the most efficient thermoelectric materials at room temperature. They were used as a starting point for creating inks. As will be discussed in the following section, there were improvements in ZT for p-type composite materials due to sintering happening at high curing temperature while no improvement in ZT has been observed for n-type material. Se doped n-type inks were created by mechanical alloying. Additionally, mechanically alloyed (MA) p-type bismuth antimony telluride has also been explored to make it more cost effective and improve the thermoelectric properties. We present the details of the mechanical alloying of n and p-type thermoelectric materials in chapters 4 and 5.

3.3 Printable Composite Materials Synthesis

Bulk 80-100 mesh (150-180 micron) n and p-type powders were purchased from Super Conductor Materials, Inc (SCM, Inc. Suffern, NY). To achieve the 100-200 micron thick films, 50-100 micron sized printer tips are required to dispense the materials. The size of the printer tip limits the maximum particle size of the active component. Empirical testing in the laboratory has shown that the average particle size needs to be smaller than the tip size by an order of magnitude to allow for continuous printing without clogging. Sub-micron and nanoparticles may allow for optimum dispensing, however the resulting slurries were found to have high electrical resistivity. Additionally, the increased surface-to-volume ratio of the particles limits high mass loading in the composite system. Empirical tests have suggested that powders with an average particle size of 10μm produce optimal composite properties and are suitable for continuous dispensing without clogging the tip [8, 49, 53]. To produce 10μm average particles, bulk 80-100 mesh Bi_2Te_3 (n-type) and Sb_2Te_3 (p-type) powders purchased from SCM, Inc. were processed using a high-energy planetary ball-mill (Torrey Hills ND 0.4L). The starting powders were placed in 100ml stainless steel jars with 3mm stainless steel balls at a ball-to-powder mass ratio of 10:1.

Isopropanol was used as a wet-grinding agent with a 1:1 solvent-to-powder weight ratio. The jars were then placed in the planetary ball mill and run at 180 rpm for 30 min. All materials preparation and extraction were performed under a dry argon environment to prevent oxidation of materials. The particle size distribution of the powders was measured using a Coulter LS-100 laser diffraction particle size analyzer. The resulting average particle size after ball milling is approximately 10μm while the bulk of the particles range between 3μm and 30μm.

To make dispenser printable slurries, active particles need to be mixed in polymer binder with some solvents. According to the percolation theory, when the volume of conductive filler particles is above certain percolation threshold, a network of conductive filler is formed throughout the composite systems [51]. Empirical studies, in our case, show that active particles to epoxy volume ratio should be at least 36% to 64% in order to form the conductive path. An increase in the volume ratio of active particles beyond 40% resulted in cracking of the cured film. The epoxy resin system (active particles to epoxy volume ratio of 40% to 60%) as a polymer binder resulted in compact films with high mass loading (82%) of active particles and overall good thermoelectric properties with minimal cure shrinkage. The slurry was mixed using a vortex mixer for about 1-3 hours with regular pause intervals and ultrasonic bath for 15 minutes to disperse the particles. The thermoelectric inks were then printed on glass substrates to form 100-120μm thick films using dispenser printing, and cured at 250°C or 350°C for 12 hours to form solid thick films.

3.4 Materials Characterization

A modulated differential scanning calorimeter (DSC, Model 2920, TA Instruments) was used to study the curing profile of the polymer matrix. The onset peak and disintegration temperatures from the exothermic and endothermic diagrams were recorded and analyzed. The morphology of grains and grain boundaries were observed using a scanning electron microscope (JSM-6490 LV). Electrical conductivity measurements of the printed thermoelectric materials were carried out using the Van der Pauw method to determine the sheet resistance of the materials. Seebeck measurements were performed using a custom Seebeck testing system to determine the voltage output of the material for a given temperature difference (ΔT). Both the electrical conductivity and the Seebeck coefficients of the materials were measured at various temperature set points ranging from room temperature to 150 $^\circ$C. This allowed for materials characterization at temperature ranges of low-grade heat applications. For each temperature set point, up to 70 measurements were taken for each sample. All measurements were taken in a thermally insulated Faraday cage to

limit sources of error from the ambient environment. The Hall coefficients, carrier concentration, and carrier mobility of the samples were measured at room temperature using an Ecopia HMS-3000 Hall effect measurement system; a magnetic field of 0.6 T and electrical current of 10 mA were applied.

Thermal conductivity measurements were performed using two different bulk thermal conductivity measurement methods. The first method was using an Anter Corp. Model 2021 steady-state thermal conductivity tester. Since measurements of thermal conductivity were limited by the large sample size requirements (24.5 mm×24.5 mm) of the tester, large composite samples were prepared by first casting the thermoelectric slurries in a Teflon mold followed by a similar curing process in an argon/vacuum oven. The second method of measuring thermal conductivity was performed using a transient plane source (TPS) method with a C-Therm TCi thermal conductivity analyzer. Transient plane source techniques have been proven to be effective for characterization of other composite systems similar to the materials studied in this work [25, 27, 42, 43].

3.5 Results and Discussion

3.5.1 Phase Change and Microstructure

The effective property of the composite system is a function of the properties of the individual materials properties [65]. It is ultimately desirable to achieve composite properties similar to or exceeding those of the bulk properties of individual materials. However, given that the electrical conductivity and the Seebeck coefficient of the polymer binder are significantly lower than that of the active filler thermoelectric material, the effective properties of the composite system are expected to be less than desirable. To achieve the preferred conductivity of the thermoelectric composite films, curing temperatures need to be optimized. The shrinkage of the polymer matrix upon curing effectively packs the fillers involved [18]. The curing profile for the epoxy polymer matrix measured by the DSC is displayed in figure 3.3(a). An exothermic peak is observed at about 150°C, typical for an imidazole derivative catalyzed curing reaction of an epoxy resin with an anhydride hardener [18]. An endothermic peak was observed at approximately 400°C suggesting the pyrolysis of the epoxy. The curing profiles of electrically conductive composites were fairly similar to that of the polymer matrix. DSC was also used to check the phase change of Sb_2Te_3 and Bi_2Te_3 ball milled powders as shown in figure 3.3(b). A sharp endothermic peak for Sb_2Te_3 is observed at about 425°C, which corresponds to the melting point of Te or a Te rich phase [47]. No endothermic sharp peaks were ob-

served in the DSC curve for Bi_2Te_3 ball milled powder in the studied temperature range.

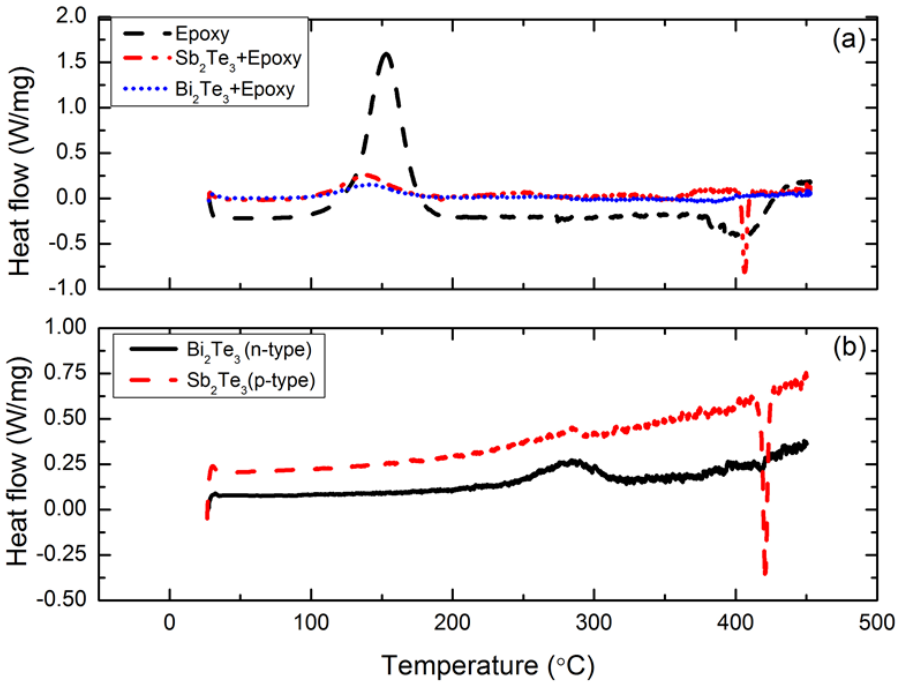

Figure 3.3: Differential Scanning Calorimeter (DSC) curves of epoxy polymer, Bi_2Te_3-epoxy, and Sb_2Te_3-epoxy matrix (a), and Bi_2Te_3 and Sb_2Te_3 ball milled powders (b).

XRD studies were performed on the as received Sb_2Te_3 and Bi_2Te_3 as shown in figure 3.4. Extra peaks of Te were found for the Sb_2Te_3 curve suggesting the presence of excess Te in the as received powder [108]. It substantiates the lower melting point of as received Sb_2Te_3 (compared to bulk Sb_2Te_3) as shown in DSC of Sb_2Te_3 in figure 3.3(b). To understand if the excess Te in the as received powder from the manufacturer was present in the form of pure Te or a Te rich Sb_2Te_3 phase, we performed electron probe microanalysis (EPMA). EPMA studies, as shown in figure 3.5 indicate the presence of a Te rich Sb_2Te_3 phase (bright areas) as well as stoichiometric Sb_2Te_3 (main area) [103]. The elemental ratio of Sb to Te was approximately 1:3.4 in the bright area whereas it was approximately 2:3 in the main area confirming the presence of excess Te.

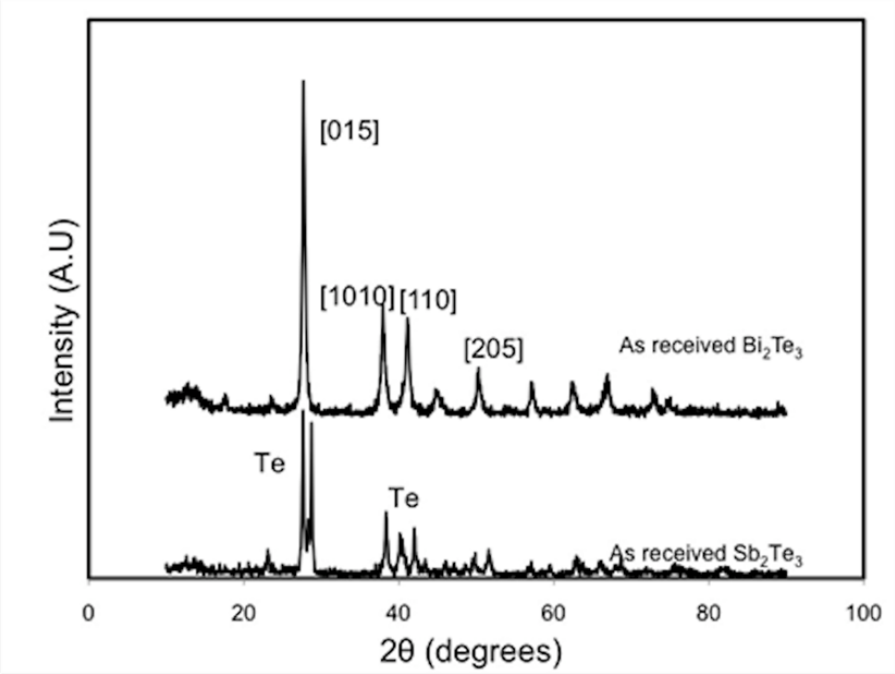

Figure 3.4: X-ray powder diffraction (XRD) patterns of as received thermoelectric powders.

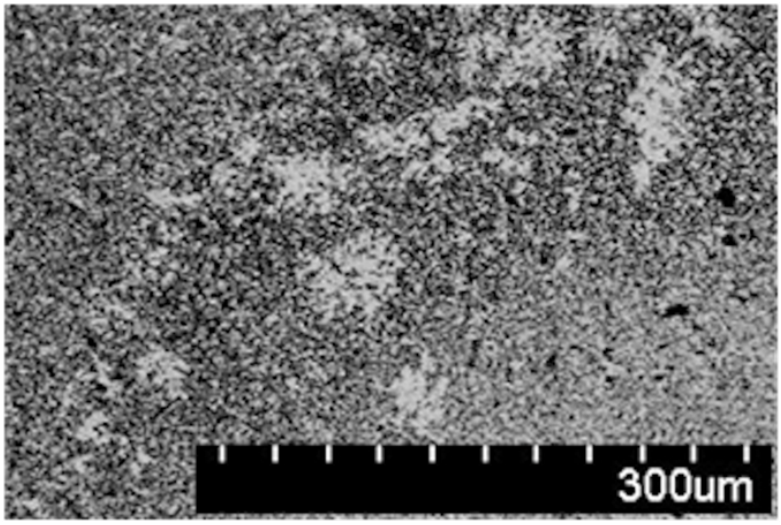

Figure 3.5: EPMA micrograph of p-type Sb_2Te_3.

Figure 3.6 shows the SEM micrographs of Sb_2Te_3 and Bi_2Te_3 DSC samples. Figure 3.6(a) shows the non-uniform distribution of micron and sub-micron particles of Sb_2Te_3 ball milled powder. Figure 3.6(b) and figure 3.6(c) show SEM images of Sb_2Te_3 ball milled powders heated to 350°C and 475°C respectively. There is evidence of grain coalescence at 350°C and formation of large grains at 475°C. Figure 3.6(d) shows the SEM image of Bi_2Te_3 powder heated to 475°C. No evidence of sintering is observed. Figure 3.7 shows the SEM image of p-type Sb_2Te_3 and epoxy resin composite film cured at 350°C. The image of p-type composite film shows a similar clustering of particles as observed in SEM images of Sb_2Te_3 DSC powders.

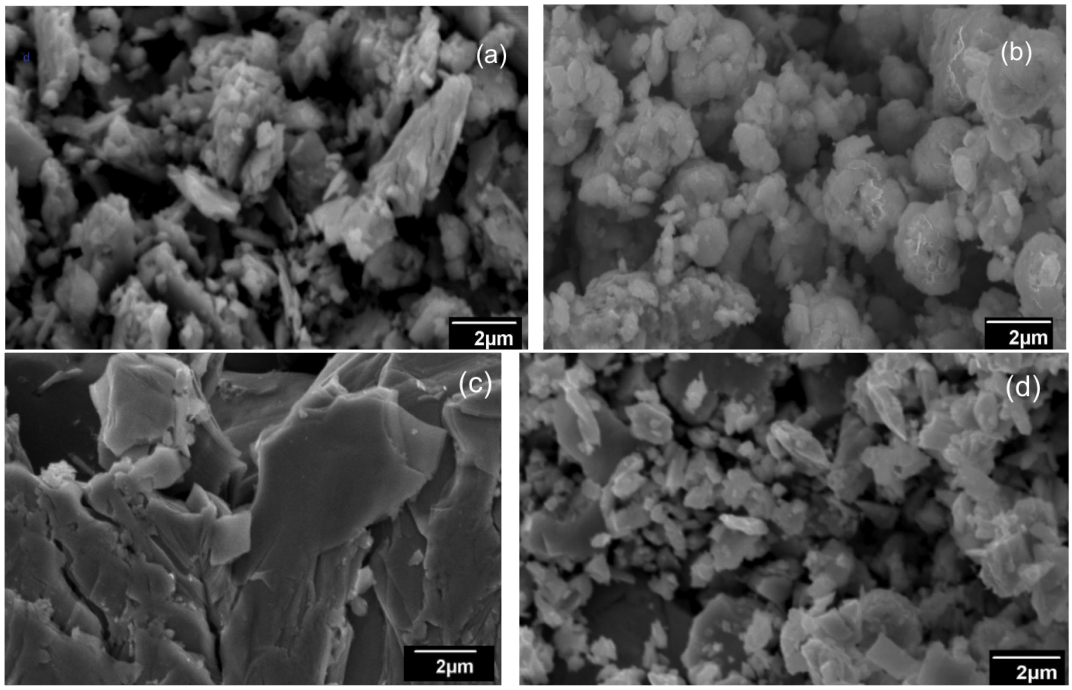

Figure 3.6: SEM micrographs of Sb_2Te_3 powder (a), Sb_2Te_3 powder heated to 350°C (b), Sb_2Te_3 powders heated to 475°C (c), and Bi_2Te_3 powder heated to 475°C (d).

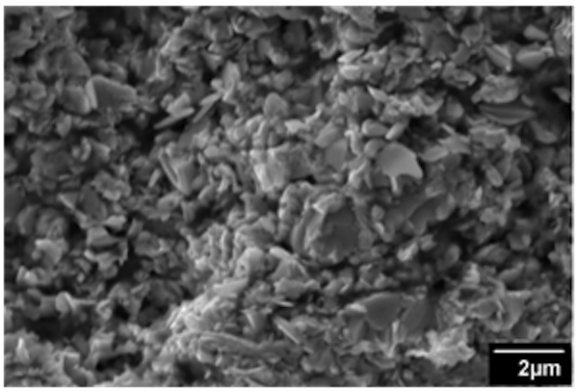

Figure 3.7: SEM micrographs of Sb_2Te_3 and epoxy resin system cured at 350°C.

3.5.2 Thermoelectric Properties

The thermoelectric and thermal transport properties of n-type Bi_2Te_3 and p-type Sb_2Te_3 thermoelectric composites films, cured in the temperature range of 150-350°C, were studied at room temperature. This temperature range was chosen based on the DSC curves of the epoxy and ball milled thermoelectric powders. The effect of curing time was studied on composite films cured at 350°C. Curing time was varied in the range of 6-48 hours. Figure 3.8 shows the thermoelectric properties of p-type Sb_2Te_3 and n-type Bi_2Te_3 composite films as a function of curing temperature. Error bars show the variation of measured thermoelectric properties for various samples prepared using exactly same specifications. While the electrical conductivity (σ) of n-type Bi_2Te_3 samples show little change, the conductivity of p-type Sb_2Te_3 composite films increase by orders of magnitude with increasing curing temperature as shown in figure 3.8(a). At a curing temperature of 150°C, the electrical conductivity was low (1.80 S/cm) as charge carriers were limited by grain boundary scattering [98]. However, as the curing temperature increased, sintering took place resulting in larger grains and reduction of grain boundary scattering. This resulted in higher conductivity of the samples cured at higher temperature (450 S/cm for sample cured at 350°C) [13]. The DSC curve of Sb_2Te_3 sub-micron particles showed in figure 3.3(b) and SEM micrograph shown in figure 3.6(b) support the described mechanism. The insensitivity of the conductivity of Bi_2Te_3 composite film curing temperature can be explained by the absence of sintering. The DSC curve for Bi_2Te_3 powder in figure 3.3(b) and the SEM micrograph in figure 3.6(d) imply that sintering is unlikely in the case of Bi_2Te_3 films.

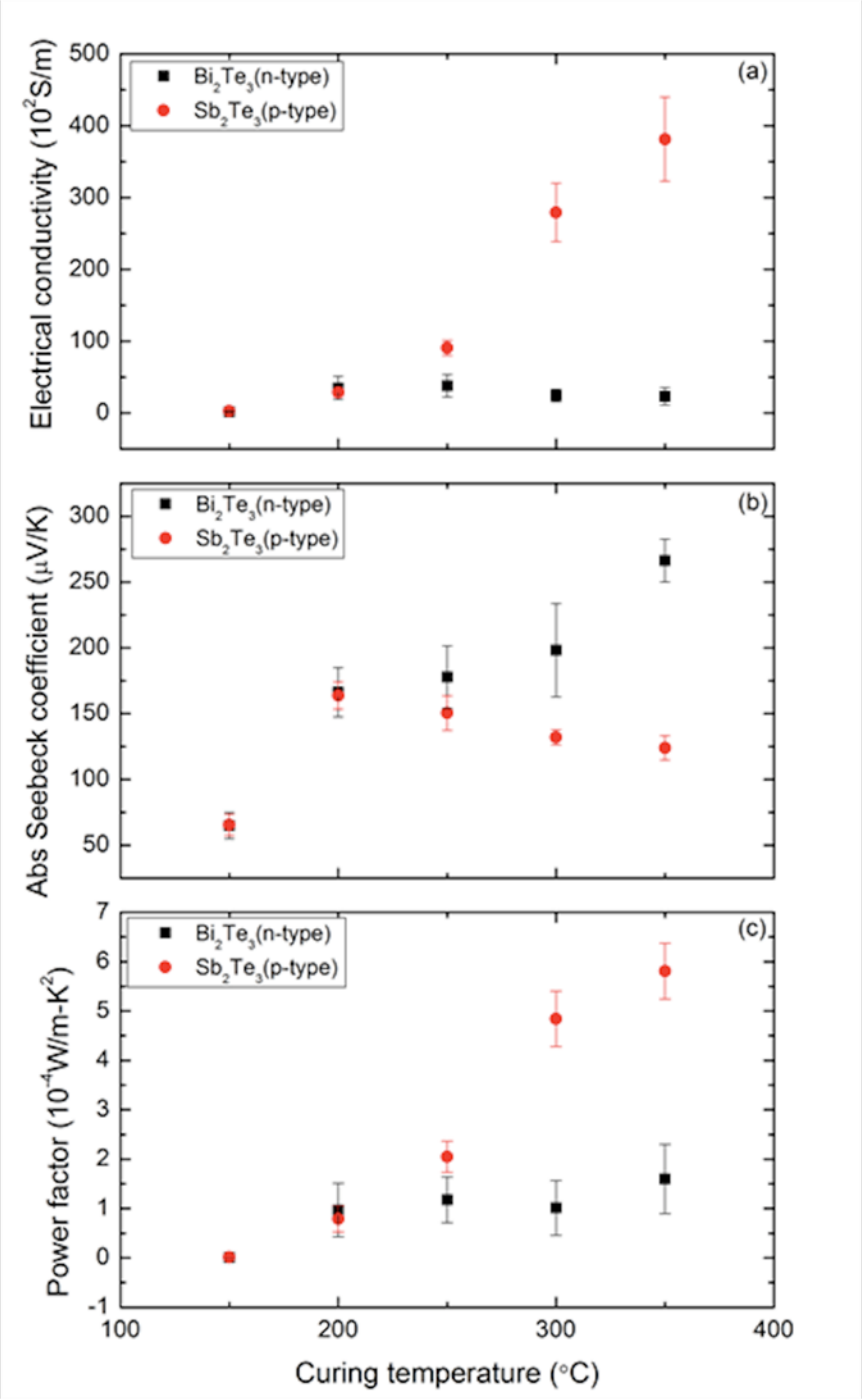

Figure 3.8: Electrical conductivity (a), Seebeck coefficient (b), and power factor (c), all measured at room temperature, of printed composite films as a function of curing temperature.

Figure 3.8(b) shows the trend of Seebeck coefficients (α) for n-type and p-type printed composite films with curing temperature. On increasing the curing temperature above 200°C, α decreases for p-type Sb_2Te_3 thermoelectric composite films as shown in figure 3.8(b) and in table 3.1. Probably, as the curing temperature approached the sintering temperature (350°C), more anti-site defects were generated and therefore the carrier (holes) concentration increased [41].

According to Ioffe, the Seebeck coefficient is a function of the carrier concentration [36]. Hall Effect measurements have confirmed that the carrier concentration was much higher for samples cured at 350°C as compared to samples cured at 200°C as shown in table 3.1. For n-type Bi_2Te_3 composite films, the Seebeck coefficients were negative, confirming it as an n-type material. The absolute Seebeck coefficient increased significantly as the curing temperature increased while the carrier concentration decreased (figure 3.8(b), table 3.1). N-type defects are likely generated during the process of mechanical deformation during powder formation providing n-type excess carriers [111]. These defects decrease with increase in curing temperature and curing time resulting in a decrease of carrier concentration [46].

Figure 3.8(c) shows the power factor ($\alpha^2\sigma$) as a function of the curing temperature. The power factor for Bi_2Te_3 samples increased as the curing temperature increased from 150°C to 200°C and remained unchanged as curing temperature increased beyond 200°C. This is due to the inverse behavior of the Seebeck coefficient and electrical conductivity with increasing curing temperature. As a result the power factor showed no improvement for Bi_2Te_3 composite films. However, the power factor for p-type Sb_2Te_3 composite films increased with increasing curing temperatures due to the large improvement in electrical conductivity.

The effects of curing time (t) on thermoelectric properties of printed composite thick films were also examined. Figure 3.9(a) shows that the electrical conductivity of p-type Sb_2Te_3 composite films increased with increase in annealing time at 350°C. Error bars show the variation of measured thermoelectric properties for various samples prepared using exactly same specifications. This is likely due to an increase of grain sizes with increasing curing time, which reduces the scattering by grain boundaries and increases the necks between particles [95]. No improvement in n-type Bi_2Te_3 was observed with increase in curing time.

Table 3.1: Materials properties of printed thermoelectric/epoxy composites measured at room temperature (bulk properties of cold-pressed samples reported for comparison).

Sample	T_c (°C)	t (h)	α (μV/K)	σ (S/cm)	$\alpha^2\sigma$ (W/m K^2)	μ (cm^2/V s)	n (/cm^3)	k (W/m K)	ZT
Bi_2Te_3(bulk)			-150	450	1.01×10^{-3}	128.5	-2.3×10^{19}	1[112]	0.3
Bi_2Te_3	200	12	-168	24	6.85×10^{-5}	4.6	-3.9×10^{19}	0.24	0.11
Bi_2Te_3	350	12	-275	17	1.28×10^{-4}	16.7	-6.3×10^{18}	0.24	0.16
Bi_2Te_3	350	36	-287	14	1.15×10^{-4}	16.7	-5.1×10^{18}	0.24	0.14
Sb_2Te_3(bulk)			112	612	7.67×10^{-4}	215	1.8×10^{19}	1[24]	0.23
Sb_2Te_3	200	12	174	11	3.25×10^{-5}	1.7	3.6×10^{19}	0.24	0.04
Sb_2Te_3	350	12	152	315	7.37×10^{-4}	39.3	5×10^{19}	0.54	0.41
Sb_2Te_3	350	36	115	520	6.88×10^{-4}	38.5	8.5×10^{19}	0.54	0.38

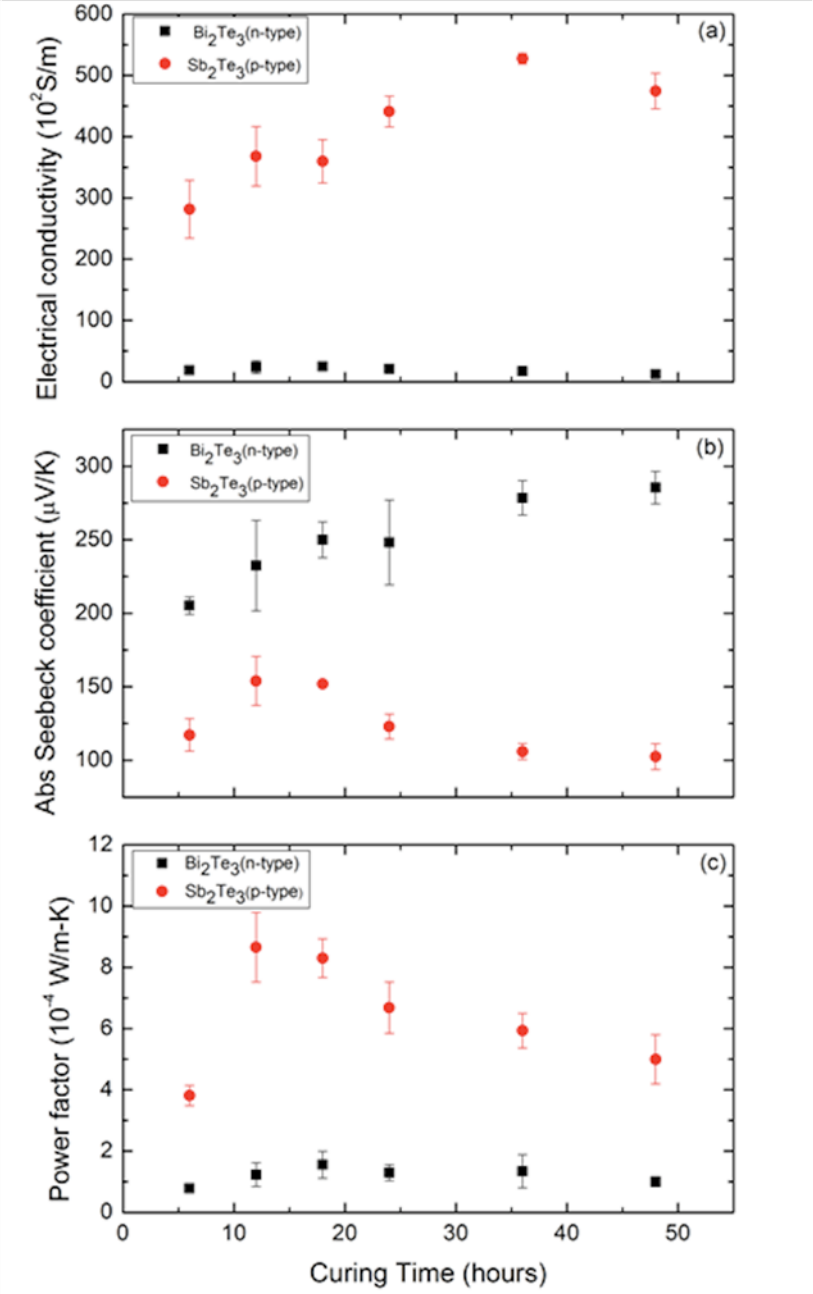

Figure 3.9: Measured electrical conductivity (a), Seebeck coefficient (b), and power factor (c) of printed composite films as a function of curing time.

Figure 3.9(b) shows the effect of curing time on the Seebeck coefficient for both

p-type Sb_2Te_3 composites and n-type Bi_2Te_3 composites. For p-type composites, the Seebeck coefficient decreased due to increase in carrier concentration as previously explained. For n-type Bi_2Te_3 composite thick films, the Seebeck coefficient increased with increase in curing time. The carrier concentration for various samples cured at 350°C for different hours were measured and were found to continuously decrease with increase in curing time as previously explained [111].

Figure 3.9(c) shows the power factor as a function of curing time at 350°C. The power factor for Bi_2Te_3 sample increased when the curing time increased from 6 to 12 hours but remained unchanged afterwards. While the Seebeck coefficient increased, the electrical conductivity decreased with increasing curing temperatures, thus reducing the power factor. The power factor for p-type Sb_2Te_3 composite films increased with increase in curing time from 6 to 12 hours but also showed no improvement with additional annealing time. These graphs indicate that a 12 hours curing and annealing time at 350°C provide optimized thermoelectric properties for p-type Sb_2Te_3 composite films.

The thermal conductivity (k) of the composite material is significantly below that of bulk thermoelectric materials due to the insulating epoxy (thermal conductivity 0.2W/m-K) and the presence of fine grains of the active filler particles [112]. The thermal conductivity of the n-type Bi_2Te_3 and p-type Sb_2Te_3 composites are 0.24 W/m-K when cured at 200°C, and results are comparable to that of silver based electrically conductive adhesives [18]. At 350°C curing temperatures, the thermal conductivity of Bi_2Te_3 composite sample remains unchanged while the thermal conductivity of Sb_2Te_3 composite sample increased to 0.54 W/m-K (Table 3.2). This is likely due to larger grain formation from sintering, resulting in increase of the thermal conductivity [112]. While precautions were taken during sample preparation to form dense samples, the larger samples exhibited some porosity. Maximum ZT of 0.41 for the Sb_2Te_3 and 0.16 for Bi_2Te_3 composite films were achieved when films were cured at 350°C for 12 hrs. Although ZTs of composite thermoelectric materials are less than for bulk materials they are higher than previously reported ZTs for printable thermoelectric materials [39, 98, 102].

Table 3.2: Thermal conductivity and ZT values for composite thermoelectric materials.

Composite Materials	Curing Temp.	Thermal Conductivity(W/m-K)	ZT
Bi_2Te_3-epoxy	350°C	0.24	0.16
Sb_2Te_3-epoxy	350°C	0.54	0.41

3.6 Conclusion

1. In order to dispenser print thermoelectric energy generators, printable thermoelectric materials must be synthesized. Printed thermoelectric inks consist of active particles dispersed in a polymer binder.

2. N-type Bi_2Te_3 and p-type Sb_2Te_3 thermoelectric composite materials were successfully developed for fabricating thermoelectric devices using a dispenser printer. Processing parameters were optimized to enhance the thermoelectric performance of the composite materials.

3. The electrical conductivity of p-type thermoelectric films was improved by an order of magnitude as a result of sintering at high curing temperature of 350°C. The electrical conductivity of n-type film did not improve when the sample was cured at 350°C.

4. The Seebeck coefficients of the composite materials were similar to the bulk materials properties of the active particles. Epoxy, as an insulating binder in the printable system, reduces the thermal conductivity of the printed material which is favorable for improving the figure of merit of the composite.

5. Maximum ZT of 0.41 for the Sb_2Te_3 and 0.16 for Bi_2Te_3 composite films were achieved when films were cured at 350°C for 12 hrs.

Chapter 4

Enhanced Performance of n-type Bi_2Te_3 Composite TEGs

4.1 Overview

As reported in chapter 3, p-type composite films have ZT of 0.41 whereas n-type thermoelectric composite thick films have ZT of 0.18, when cured at 350°C. Electrical conductivity and overall ZT are higher for p-type Sb_2Te_3/epoxy composite films as compared to stock n-type Bi_2Te_3/epoxy composite films. This chapter focuses on optimizing the synthesis and processing parameters to maximize the ZT of n-type composite thermoelectric thick films for dispenser printing by using mechanical alloying and Se as an additive. Additionally, we demonstrate device fabrication and testing techniques for high-density arrays of high-aspect-ratio planar TEGs via a cost effective, scalable, energy efficient dispenser printing method.

4.2 Mechanical Alloying

Mechanical alloying, with controlled amount of Se additives, was used to improve the electrical conductivity of n-type Bi_2Te_3. Doped powders were synthesized by mechanically alloying the raw constituents in the proper stoichiometric ratios. Figure 4.1 shows the mechanical alloying processing steps for creating doped powders for use in thermoelectric inks. Elemental Bi (99.999%, 1-5mm balls) and Te (99.999%, 1-12 mm chunks) (Sigma Aldrich Corporation) were selected as starting materials for mechanical alloying. A molar ratio of 36:64 of Bi and Te was used to form mechanically alloyed (MA) n-type Bi_2Te_3[23]. Varying amounts of Se, 1-6 wt% of

the total weight of Bi_2Te_3, were added. Se was chosen as a dopant to improve the overall thermoelectric properties of the MA Bi_2Te_3[33, 64, 78]. The details of how Se helps to improve the thermoelectric properties is presented in section 4.4. As discussed in chapter 3, an average particle size of approximately 10µm is needed to dispenser print inks [7, 9, 57]. Stainless steel jars containing 10 mm diameter balls were used for the mechanical alloying. The ball to powder weight ratio was kept at 15:1. All powder handling was performed in an argon-filled glove box, in which the oxygen level was kept below 5 ppm to prevent oxidation of the powders. Mechanical alloying was carried out in a planetary ball mill apparatus (Torrey Hills ND 0.4) at 315 rpm for 14 hours in a purified argon atmosphere. The particle size of the mechanically alloyed powders was measured using a Coulter LS-100 laser diffraction particle size analyzer. The particle size ranged between 1-200µm. To further reduce the particle size, the mechanically alloyed powders were wet grinded with 3 mm stainless steel balls at a ball-to-powder mass ratio of 10:1 with isopropyl alcohol (1:1 fluid to powder ratio) at 245 rpm for 2 hours. The resulting average particle size was less than 2µm.

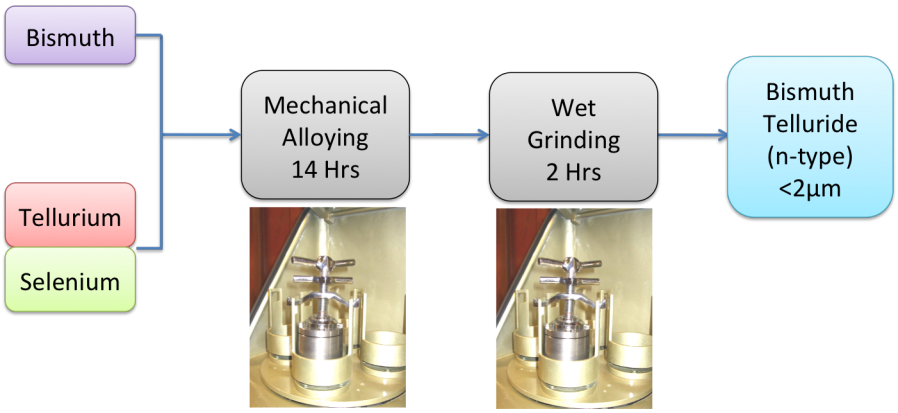

Figure 4.1: Mechanical alloying and wet grinding of n-type Bi_2Te_3 with Se additive.

To make dispenser printable slurries, active particles were mixed with the epoxy resin, as described in chapter 3. The slurry was mixed using a vortex mixer and an ultrasonic bath to disperse the particles. The thermoelectric inks were then printed on glass substrates to form 100-120µm thick films using dispenser printing, and cured at 250°C or 350°C for 12 hours to form solid thick films.

4.3 Materials Characterization

X-ray powder diffraction (XRD) was performed on both MA Bi_2Te_3 powder and MA Bi_2Te_3 with 1wt% Se powder. The XRD pattern is as shown in Figure 4.2 and can be indexed to Bi_2Te_3 (JCPDF, no. 15-0863). The XRD pattern of MA Bi_2Te_3 with 1wt% Se indicates that, the majority of the Bi_2Te_3 and Se reacted with each other to form $Bi_2Te_{3-x}Se_x$ solid solution during mechanical alloying [17, 104, 105]. Absence of Se peak at 30° indicated that all the Se was consumed to form solid solution. This is why the XRD peaks in Figure 4.2 shift slightly to larger angles. However, the crystal structure (rhombohedral) of Bi_2Te_3 with space group (R3 m) remains unchanged; Se substitutes at Te sites only [17, 104, 105].

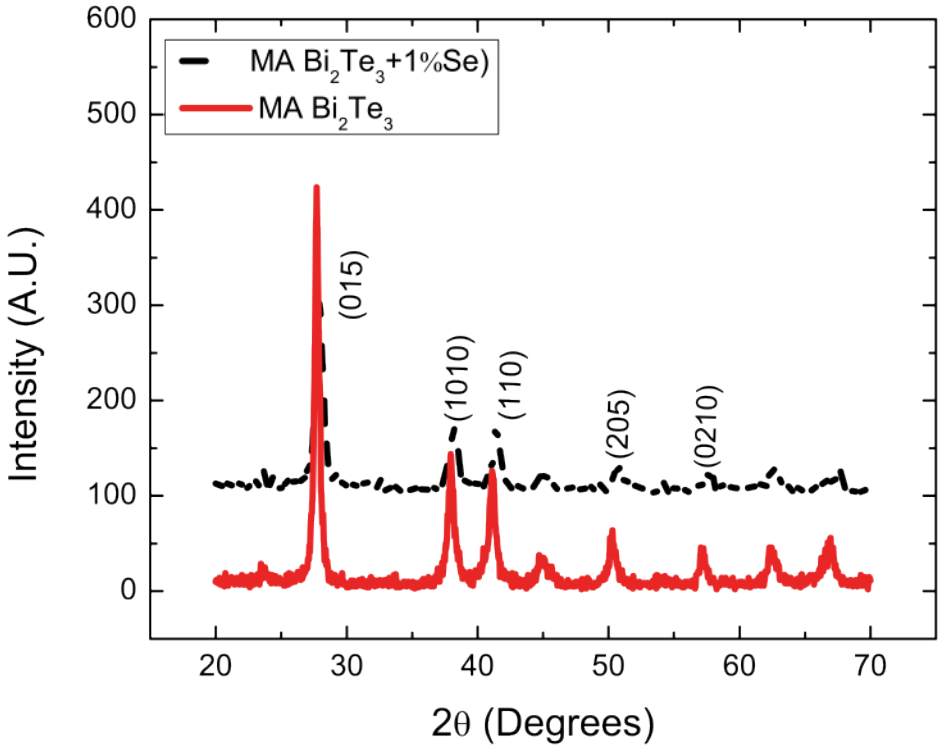

Figure 4.2: X-ray powder diffraction (XRD) patterns of MA Bi_2Te_3 with 1wt% extra Se thermoelectric powders.

Figure 4.3 shows the scanning electron microscope (SEM) of Bi_2Te_3 powder. The average particle size is below 2μm. Differential scanning calorimeter (DSC, Model 2920, TA Instruments) was used to study the melting point of MA Bi_2Te_3 with 1wt% Se sample. An endothermic reaction was observed at 425°C, as shown in Figure 4.4. The DSC analysis was carried out in the air. The constant increase in the entire temperature range in Figure 4.4 is possibly due to oxidation of the sample.

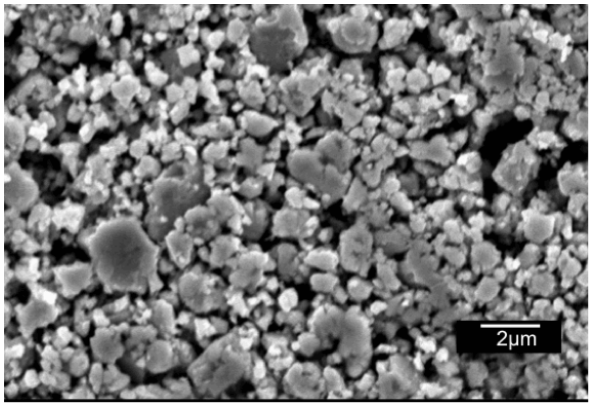

Figure 4.3: SEM micrographs of MA Bi_2Te_3 confirming average particle size less than 2μm.

The morphology of grains and grain boundaries of this DSC sample was analyzed using the scanning electron microscope (JSM-6490 LV), as shown in Figure 4.5(a). This SEM image suggests that MA Bi_2Te_3 with 1wt% Se melts (or undergoes grain growth) at much lower temperature (below 475°C) than stoichiometric Bi_2Te_3 (580°C) [78]. The SEM image of stoichiometric Bi_2Te_3heated to 475°C is shown in figure 4.5(b) for comparison. However, since epoxy disintegrates at 400°C[56], we did one more DSC of the MA Bi_2Te_3 with 1wt% Se heated to 350°C to check the possibility of grain coalescence. The SEM image of this DSC sample (heated to 350°C) as shown in Figure 4.5(c) confirms the grain coalescence at lower temperature. Therefore, dispenser printed composite films were cured at temperatures 250°C, 300°C, 350°C to verify the grain coalescence effect in epoxy polymer matrix. Figure 4.6 shows scanning electron microscope (SEM) images of an MA Bi_2Te_3 with 1wt% Se/epoxy composite film cured at 350°C. Bi_2Te_3 grains are uniformly dispersed in the epoxy matrix. Epoxy serves to hold the Bi_2Te_3 grains together in the cured film. EDS analysis also indicated that amorphous areas are rich in insulating carbon confirming the presence of epoxy. Burning off the epoxy by curing the composite films at higher temperature of 400°C (disintegration temperature of epoxy) resulted

in cracking of the film. Figure 4.6 also suggests that even though epoxy is present in composite films, grain coalescence is still taking place.

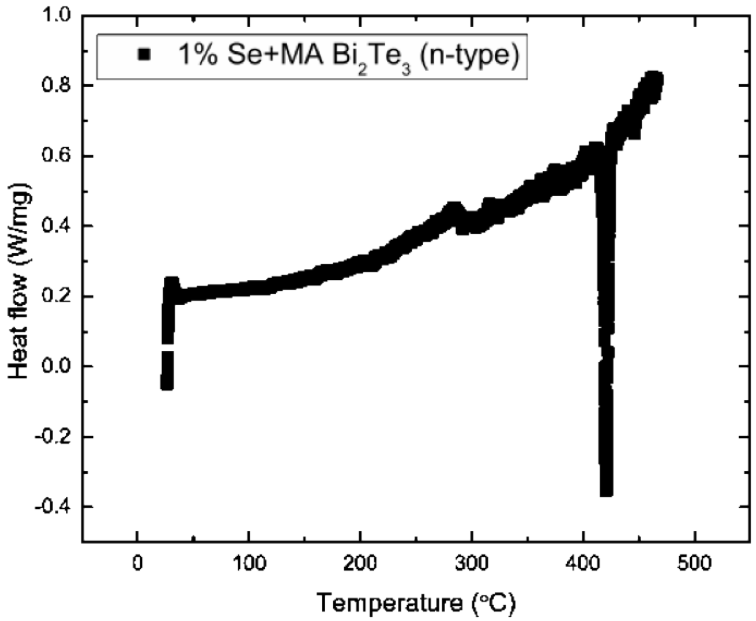

Figure 4.4: Differential scanning calorimeter (DSC) curves of MA Bi_2Te_3 sample with 1wt% extra Se.

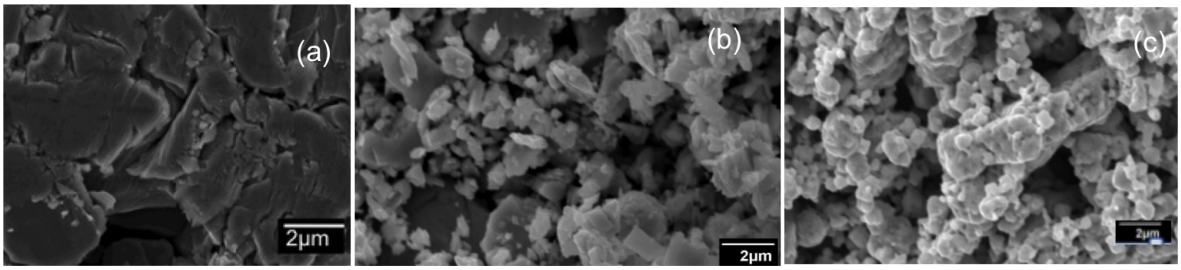

Figure 4.5: SEM micrograph of MA Bi_2Te_3 with 1wt% Se powder (DSC sample) heated to 475°C (a), stoichiometric Bi_2Te_3heated to 475°C (b), and MA Bi_2Te_3 with 1wt% Se powder (DSC sample) heated to 350°C (b).

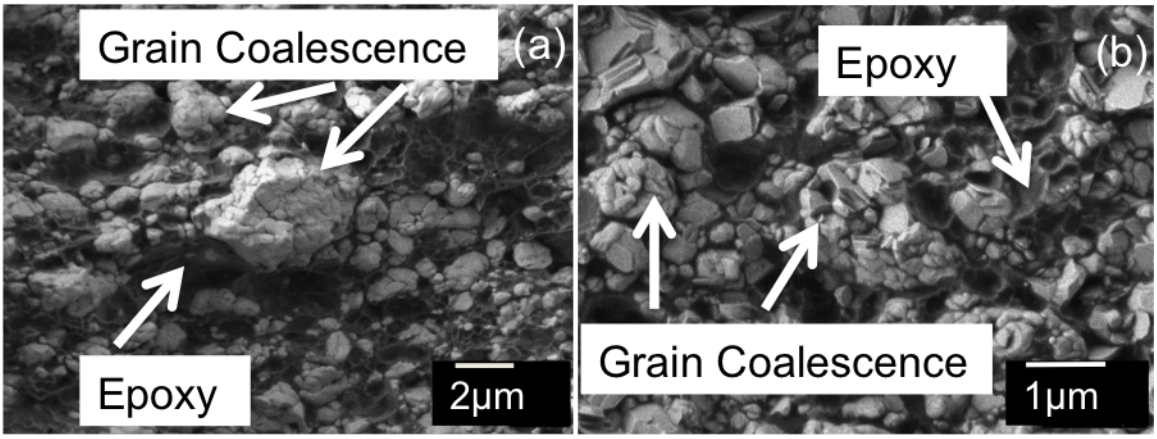

Figure 4.6: SEM micrographs of MA Bi_2Te_3 with 1wt% Se epoxy composites cured at 350°C.

4.4 ZT Improvement Results and Discussion

Figure 4.7 shows the thermoelectric properties of MA n-type Bi_2Te_3 composite films cured at 250°C and 350°C for 12 hours measured at room temperature, as a function of %Se added. The curing temperatures and curing time of 12 hours were chosen based on previous results for p-type Sb_2Te_3/epoxy composite films [56]. Error bars show the variation of measured thermoelectric properties for various samples prepared using exactly same specifications. It is clear from Figure 4.7 (a) that electrical conductivities of composite films are much lower than that of bulk Bi_2Te_3[56]. This decrease in the electrical conductivity can be attributed to the presence of the insulating polymer phase. Effective-medium-theory (EMT) explains the decrease in electrical conductivity due to presence of insulating polymer phase [62, 69, 99]. Another possible reason may be a decrease in the charge carrier mobility due to grain boundary scattering [13].

As shown in Figure 4.7 (a), the addition of 1wt% Se resulted in significant improvement in the electrical conductivity of composite films compared to without Se additive MA Bi_2Te_3 composite films. This improvement in the electrical conductivity is likely due to the following mechanism. Se substitutes Te sites due to weaker $Te^{(1)}$-Bi-$Te^{(2)}$-Bi-Te- bonds and becomes $Te^{(1)}$-Bi-Se-Bi-Te or Se-Bi-$Te^{(2)}$-Bi-Te, leaving extra Te available to melt at lower temperatures [78]. The DSC curve of 1%Se Bi_2Te_3 in Figure 4.4 shows that melting of this sample occurred at 425°C rather than at 580°C, the standard melting temperature of Bi_2Te_3. This melting is also

verified by SEM micrograph of the DSC sample, as shown in Figure 4.5(a). The lower melting point helps in grain coalescence and formation of larger grains at lower sintering temperatures of 350°C, as shown in Figure 4.5(b). This increase in grain size as a result of adding 1% Se is also observed for dispenser printed composite films as shown in Figure 4.6. These larger grains result in reduction in grain boundary scattering and improve mobility of carriers. The mobility of the 1%Se sample cured at 350°C was found to be 24 cm^2/V-sec, which is four times higher than (6 cm^2/V-sec) mobility of un-doped sample cured at 350°C. As a result, electrical conductivity increases due to addition of 1% Se.

The electrical conductivity did not improve with increase in Se wt% beyond 1%. This is likely due to an increase in the band-gap of MA Bi_2Te_3 with increase in the amount of Se [64]. The melting point of Se doped Bi_2Te_3 does not decrease with adding more Se [78]. Therefore, there are no further gains in mobility due to addition of Se. Instead there are increase in band-gap lowers carrier concentration causing lower conductivity.

The electrical conductivity of samples cured at 250°C is lower compared to samples cured at 350°C due to the curing temperatures being much smaller than melting point of the MA Bi_2Te_3. The highest electrical conductivity (140 S/cm) was achieved for 1wt% Se doped MA Bi_2Te_3 composite films cured at 350°C. This electrical conductivity is still an order of magnitude lower than the bulk Bi_2Te_3 mainly due leftover epoxy in the composite films cured at 350°C. The presence of epoxy in the composite films cured at 350°C is verified using SEM as shown in Figure 4.6.

Figure 4.7(b) shows variation of the Seebeck coefficient with respect to Se wt%. The negative values confirm the synthesized powder as an n-type material. The Seebeck coefficient decreases with increase in carrier concentration for a single phase system [23]. However, the Seebeck coefficient of a two-phase (active and polymer) composite system, estimated by effective-medium-theory (EMT), also depends on effective electrical and thermal conductivity of composite system [69, 99, 112].

$$\alpha = 6k \frac{< \alpha_j D_j >}{1 - 3 < k_j D_j >} \tag{4.1}$$

and

$$D_j = \frac{\sigma_j}{(k_j + 2k)(\sigma_j + 2\sigma)} \tag{4.2}$$

where the subscript j denotes the jth phase, $<>$ denotes the volume average, and k and σ are effective thermal and electrical conductivities of the composite system and can be obtained by the EMT as follows

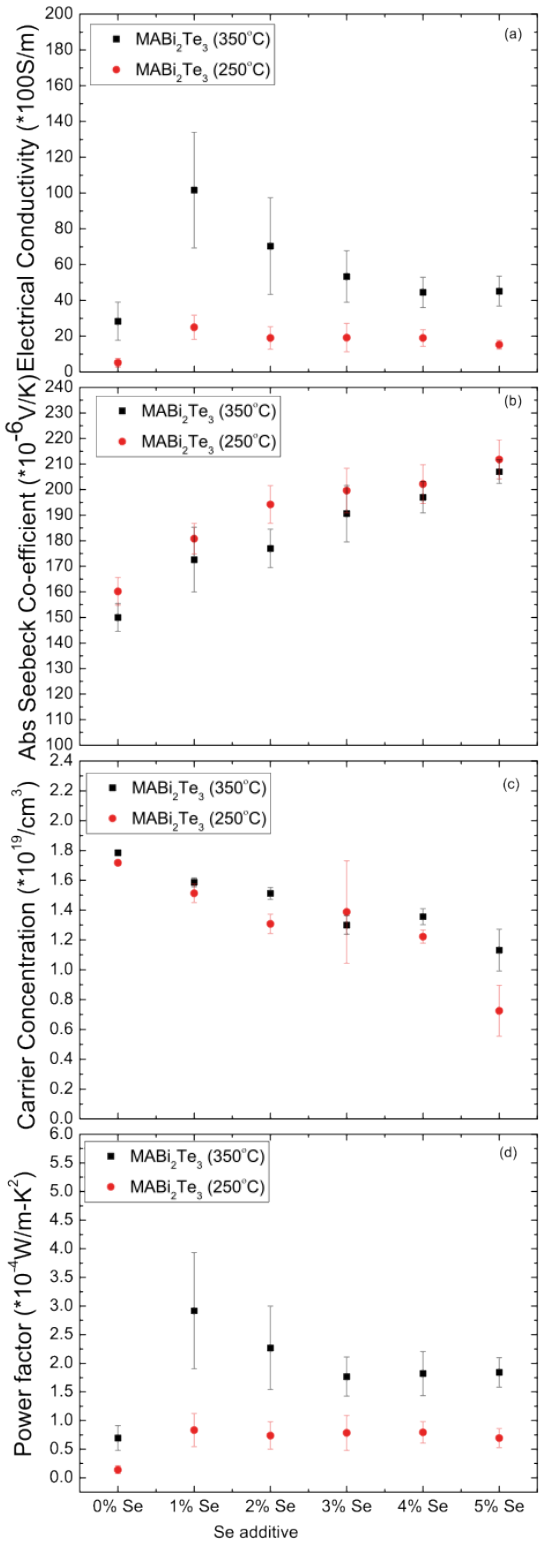

Figure 4.7: Thermoelectric properties of MA Bi_2Te_3 dispenser printed composite films as a function of Se as an additive and curing temperature, including electrical conductivity (a), Seebeck coefficient (b), carrier concentration (c), and power factor (d).

$$< \frac{\sigma_j - \sigma}{\sigma_j + 2\sigma} >= 0 \tag{4.3}$$

$$< \frac{k_j - k}{k_j + 2k} >= 0 \tag{4.4}$$

where $< >$ denotes volume average of the property parameters. The electrical and the thermal conductivity of the insulating polymer epoxy is zero. Equation (4.3) and equation (4.4) can be simplified to get the thermal and the electrical conductivity for the active phase:

$$k_j = k;\ \sigma_j = \sigma.$$

Substituting k_j and σ_j in equation (4.2), we get (for active phase)

$$D_j = \frac{1}{9k}.$$

Equation (4.1) can, therefore, be simplified as

$$\alpha = \alpha_j \tag{4.5}$$

Therefore, the effective Seebeck coefficient of a composite system is the same as a single phase system (MA Bi_2Te_3) and is related to the carrier concentration [69, 99, 112]. The Seebeck coefficients of MA Bi_2Te_3 composite films are lower (170 μV/K) than that of Se doped MA composite printed films (200 μV/K) cured at both 250°C and 350°C. The reason for lower Seebeck coefficients without Se is the high carrier concentration of MA Bi_2Te_3 composite films as shown in Figure 4.7(c). The addition of Se as a dopant reduces the carrier concentration; therefore the Seebeck coefficient increases [33]. The absolute value of the Seebeck coefficient for printed composite films cured at 250°C was found to be slightly higher than that for films cured at 350°C. However, the mechanisms involved for Seebeck coefficient improvement while curing at 250°C and 350°C are different. During the mechanical alloying process, donor-type defects are likely to be generated which provide excess n-type carriers. These defects decrease with increasing curing time, resulting in an overall decrease in carrier concentration [111]. Therefore, films cured at 250°C for 12 hours have Seebeck coefficients that are similar to bulk values. However, Te is volatilized at 350°C and bismuth oxides formed, producing anti-site defects as well as Te vacancies. This increases hole carrier concentration. As a result, donor-like defect carrier concentration gets compensated for by hole concentration, leading to an increase in the Seebeck coefficient [63, 85, 111].

Figure 4.7(c) shows the carrier concentration measurements at 250°C and 350°C. It confirms that films cured at 350°C have higher carrier concentration as compared to films cured at 250°C. Also it is clear that Se addition reduces the carrier concentration. Therefore, the Seebeck coefficient increases.

The power factor ($\alpha^2\sigma$) is found to be highest for MA Bi_2Te_3 with 1wt% Se cured at 350°C (4.7e-4 W/m-K^2) as shown in Figure 4.7(d). The average thermal conductivities of MA Bi_2Te_3 with 1 wt% Se cured at 250°C and 350°C were 0.26 W/m-K and 0.38 W/m-K, respectively, which is almost one third of the bulk value [56]. The low thermal conductivity values relative to bulk materials (typically ~1.2 W/m-K) are due to the insulating nature of epoxy and fine grains of active filler particles [56]. A maximum ZT value of 0.31 is obtained for 1wt% Se MA Bi_2Te_3 dispenser printed composite films. This ZT value is higher than the reported ZT of n-type composite thermoelectric materials [56, 57, 70, 81, 98, 102, 110].

Composite Materials	Curing Temp.	Thermal Conductivity(W/m-K)	ZT
MA Bi_2Te_3(1% Se)	250°C	0.26	0.15
MA Bi_2Te_3(1% Se)	350°C	0.38	0.31

Table 4.1: Thermal conductivity and ZT values for composite thermoelectric materials.

To investigate the temperature dependent thermoelectric properties of composites, the electrical conductivity and Seebeck coefficient of MA n-type Bi_2Te_3 with 1wt% Se were measured. Figure 4.8 shows the thermoelectric properties of 1wt% Se MA n-type Bi_2Te_3 composite films cured at 250°C, 300°C, and 350°C as a function of temperature. Figure 4.8(a) and Figure 4.8(b) show that the electrical conductivity and the Seebeck coefficient do not change with the change in temperature in the range of 20°C to 90°C. Figure 4.8(c) shows that power factor does not change with temperature in the same temperature range. Therefore, the thermoelectric properties of composite films are not adversely affected in the temperature range of 20°C to 90°C. Therefore, the TEG device made using dispenser printed composite films can be used in above mentioned temperature range.

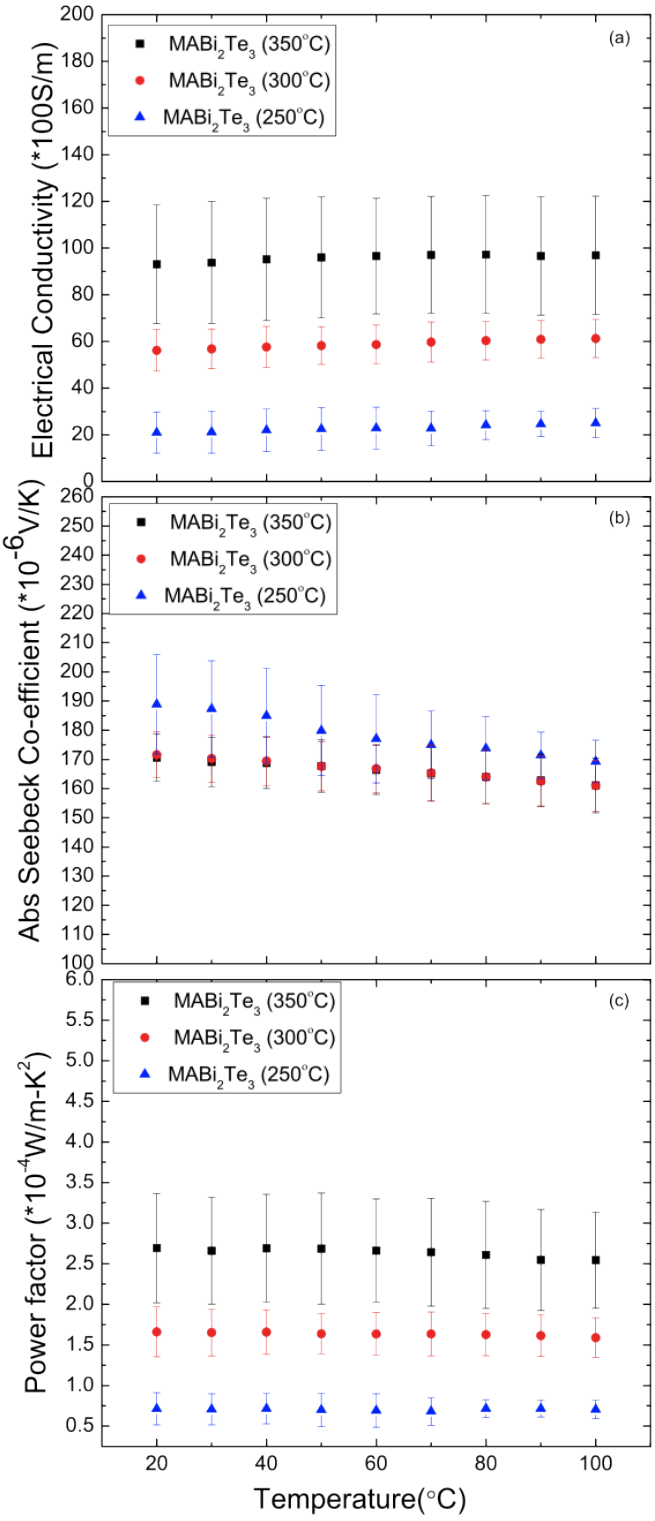

Figure 4.8: Thermoelectric properties of MA Bi_2Te_3 with 1wt% extra Se dispenser printed composite films as a function of temperature including the electrical conductivity (a), Seebeck coefficient (b) and power factor (c).

4.5 Device Fabrication and Testing

4.5.1 Single Leg Device

While TEG device geometry is highly application dependent, high-density and high-aspect-ratio arrays are frequently required for low-temperature TEG applications [21, 88]. Figure 4.9 shows an envisioned manufacturing process for dispenser-printed thermoelectric devices. We use a planar structure in combination with flexible substrate to achieve high packing density required to produce small devices that can be used for low temperature applications [7]. We use high aspect ratio device design to maintain the temperature difference across the device and to achieve reasonable power output.

A flexible printed circuit board (Flex-PCB) fabricated by Rigiflex Technology Inc. was used as a substrate. The Flex-PCB consisted of nickel and gold plated copper traces on a flexible polyimide substrate. A polyimide substrate with metal electrodes was chosen due to its flexibility, electrical insulation, high temperature tolerance and low thermal conductivity (0.12 W/m-K). Next, the MA n-type Bi_2Te_3 composite inks were dispenser printed onto the substrate to form lines spanning across the top and the bottom contacts. Thick metal contacts resulted in reduced electrical contact resistance between metal contacts and printed TE elements. Printed lines on the flex PCB were cured in an argon/vacuum oven at 300°C. 24AWG copper wires were attached to the device using conductive silver epoxy (1901-S, ESL Electroscience) to form electrical connections. A schematic and an image of dispenser printed 62-element TEG prototype consisting of elements that were 5mm × 700μm × 120μm in dimensions is shown in Figure 4.9.

4.5.2 Experimental Setup

The printed prototype device was tested using a custom testing apparatus as shown in Figure 4.10 Thermoelectric heater/coolers (9500/127/040 B, Ferrotech Corp.) were mounted onto two aluminum plates to provide surfaces for cooling and heating. The printed TEG was positioned between the plates and a temperature difference was applied across the device. Once the device reached steady state, the open circuit voltage of the device was measured using a digital multimeter. A variable load resistance was then connected in series with the device and voltage measurements were taken at multiple load resistances. The power was calculated based on the measured voltage and load resistance at various temperature differences.

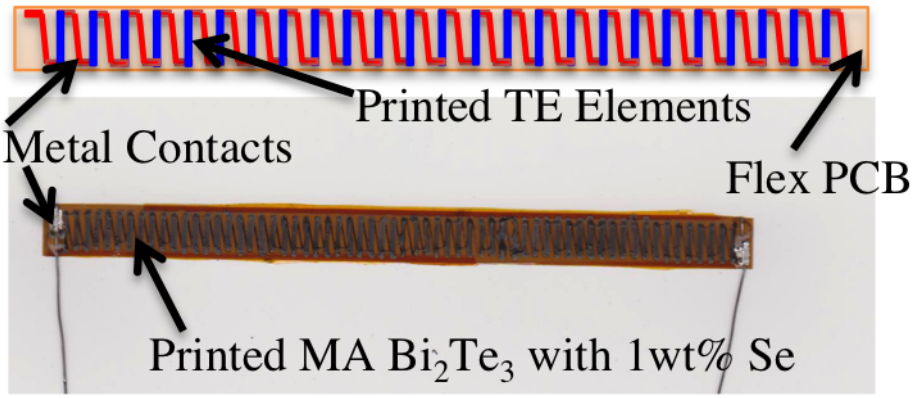

Figure 4.9: Schematic and image of dispenser printed 62-element MA Bi_2Te_3 with 1 wt% extra Se planar thermoelectric device on a flexible substrate.

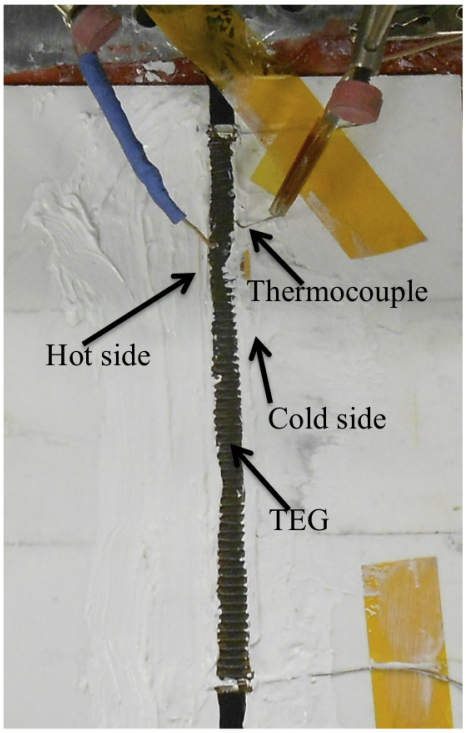

Figure 4.10: Image of thermoelectric device characterization custom built setup.

4.5.3 Device Prototype Results and Discussion

Although highest ZT was achieved when composite films were cured at 350°C we chose to cure the device at 300°C. At 350°C cracking of films and epoxy disintegration was observed to some extent. The device resistance of the prototype was 480Ω when cured at 300°C.

Figure 4.11 shows the device characteristic curve for the 62-element prototype device measured for ΔT = 20 K at various load resistances. The optimal power output of the device occurs when the load resistance matches the device resistance.

$$P_{max} = \frac{V_{op}^2}{4R_{in}} \tag{4.6}$$

where V_{op} is the open circuit voltage and depends on the number of couples m, Seebeck coefficient α and temperature difference ΔT. The internal resistance of the device R_{in} can be estimated as

$$R_{in} = \rho\frac{ml}{A} \tag{4.7}$$

where ρ is the electrical resistivity of the material, l (5mm) is the element length in the direction of heat flow, and A (700μm × 120μm) is the cross-sectional area of the element. The internal device resistance (480Ω) is very close to the expected resistance (465Ω) calculated from the materials properties. At matched load resistance, the device produces approximately 25μW at 0.23mA and 109mV closed circuit voltage.

Figure 4.12 shows the measured power density (power output per unit device area) of the device as a function of the temperature difference. Maximum power output at matched load resistance was measured at ΔT of 5K, 10K and 20K. The solid line in figure indicates the ideal model whereas the dashed line indicates the fitted model [9, 22, 87]. In the case of the fitted model, R_{in} was the measured resistance of the generator. For the ideal model, power was calculated using the intrinsic properties (α and σ) of dispenser printed MA Bi_2Te_3 with 1wt% Se films cured at 300°C. The fitted model and actual measured power density value closely matched the ideal model at ΔT of 5K, 10K. The modeling suggests that a device with current material properties is capable of achieving a power density of 135μW/cm^2 given negligible contact resistance at ΔT of 20K. However, at ΔT of 20K actual measured power density (130μW/cm^2) is slightly lower than ideal model (135μW/cm^2). The deviation may be due to fluctuations in temperature across the device during measurement and minor electrical contact resistance. It is worth noting that P_{max} is proportional to $(\Delta T)^2$ because P_{max} depends on the square of the open circuit voltage, as in equation (4.6), and the open circuit voltage depends on ΔT.

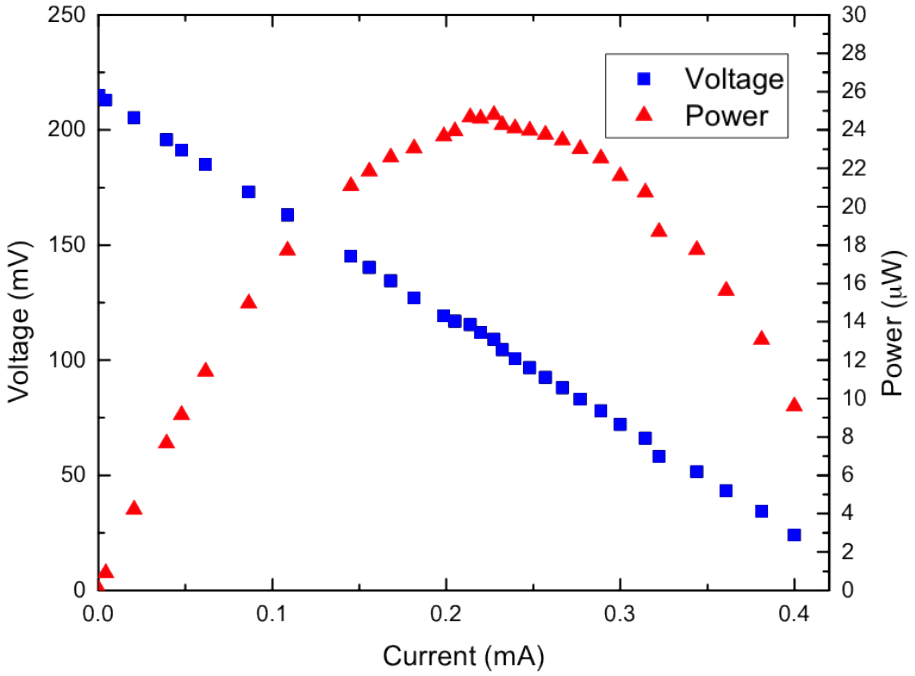

Figure 4.11: Characteristics curve of the 62 element TEG device at ΔT=20K.

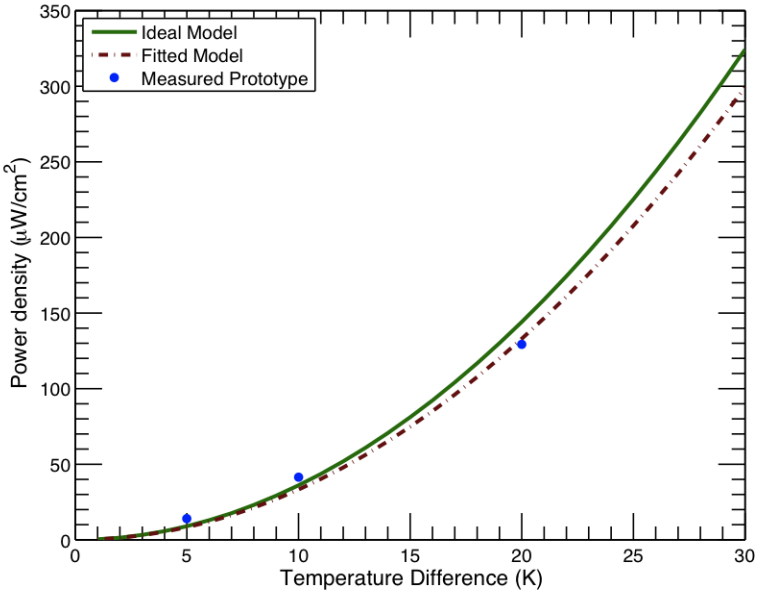

Figure 4.12: Power density at matched load resistance as a function of temperature difference across the TEG for ideal TEG model, fitted model, and measured device.

Power output for the 50-couple device is 10.5μW at ΔT=20K and the power density is 75μW/cm^2[7]. As a result of improving the materials properties and contact resistance, a power output of 25μW was achieved at ΔT=20K and power density 130μW/cm^2 for a 62 single leg n-type device. This power density is considerably higher than 0.27μW/cm^2 for ΔT=30K reported in the literature using similar printing techniques [6]. A non-optimized planar geometry was chosen for demonstration purposes. For specific applications, it is possible to design the TEG device to optimize the power output for various temperature differences.

This power is sufficient to power thermoelectric generator to provide adequate power for a wireless sensor/transmitter used in the monitoring of the equipment on aircraft, aerospace, power plant, and process plant industries. Higher output voltage and higher power is desired for the operation of many electronic devices. By integration with p-type elements and by increasing the number of couples, higher performance of devices can be achieved.

4.6 Conclusion

1. Enhanced thermoelectric properties have been achieved in MA n-type Bi_2Te_3 with 1wt% Se printable composite materials.

2. Improvements in ZT were obtained by sintering effects occurring at 350°C, which improved the electrical conductivity. The ZT was also enhanced by the low thermal conductivity of the composite material.

3. Seebeck coefficients similar to bulk values were achieved, which helped in achieving high power factor.

4. A maximum ZT value of 0.31 is obtained for 1wt% Se MA Bi_2Te_3 dispenser printed composite films when cured at 350°C.

5. A 62-element planar prototype device was printed on a custom designed flexible polyimide substrate to form a TEG.

6. The device produced 25μW at 0.23mA and 109mV for a 20K temperature difference. These results indicate an areal power density of 130μW/cm^2, which is quite close to the theoretical power density of 135μW/cm^2.

7. The results shown are promising for the use of low-cost and scalable TEGs for various low-power energy harvesting applications.

Chapter 5

Dispenser Printed MA p-type $Bi_{0.5}Sb_{1.5}Te_3$ Flexible Thermoelectric Generators

5.1 Overview

Chapter 4 described the improvements in the figure of merit of Bi_2Te_3 as a result of Se additive. Similar mechanical alloying techniques are used to synthesize p-type $Bi_{0.5}Sb_{1.5}Te_3$ with small amount of Te additives. Te as an additive helps to reduce the carrier concentration and improve the Seebeck coefficient by inhibiting the formation of anti-structure defects during mechanical alloying. This chapter focuses on optimizing the synthesis and processing parameters to maximize the ZT of $Bi_{0.5}Sb_{1.5}Te_3$-epoxy thermoelectric composites thick films by using Te as an additive. Additionally, printing and testing for high-density arrays of high-aspect-ratio planar TEGs is demonstrated using MA p-type $Bi_{0.5}Sb_{1.5}Te_3$ composite slurries.

5.2 Experimental

$Bi_{0.5}Sb_{1.5}Te_3$ was chosen as the starting p-type thermoelectric material because of its high ZT value at room temperature [72, 93]. For p-type $Bi_{0.5}Sb_{1.5}Te_3$ alloys, it is well known that holes are created by the anti-structure defects generated by the occupation of Te sites with Bi and Sb atoms [63]. Te as an additive helps to reduce the carrier concentration and improve the Seebeck coefficient by inhibiting the formation of anti-structure defects during mechanical alloying (MA) [26, 107].

Elemental Bi (99.999%, 1-5mm balls), Sb(99.999%, 1-5mm balls) and Te (99.999%, 1-12 mm chunks) (Sigma Aldrich Corporation) were selected as starting materials for mechanical alloying. A molar ratio of Bi, Sb and Te was used to form mechanically alloyed (MA) p-type $Bi_{0.5}Sb_{1.5}Te_3$[106]. A varying amount of Te, 2-10 wt% of the total weight of $Bi_{0.5}Sb_{1.5}Te_3$, was added. Te was chosen as a dopant to improve the thermoelectric properties of the MA $Bi_{0.5}Sb_{1.5}Te_3$[34, 78]. An average particle size of 10μm is needed to dispenser print inks [56]. To produce MA $Bi_{0.5}Sb_{1.5}Te_3$ particles, chunks (1-12mm size) of elemental bismuth, antimony, and tellurium were mechanically alloyed in the molar ratio [106]. A high-energy planetary ball-mill (Torrey Hills ND 0.4L) was used for MA. In addition to mechanical alloying, wet grinding was used to reduce the average particle size to 10μm [56, 58]. Thermoelectric composite inks were made using $Bi_{0.5}Sb_{1.5}Te_3$ as active particles and commercial epoxy resin as polymer matrix [56]. Vortex mixer and an ultrasonic bath were used to disperse the particles and mix the active particles in polymer to form well dispersed slurries. 100-120μm thick composite films were then printed on glass substrates using dispenser printer, and cured at 250°C for 12 hours to form thick films for measuring thermoelectric properties [56, 78, 106].

5.3 Thermoelectric Property Characterization

The XRD was performed on MA $Bi_{0.5}Sb_{1.5}Te_3$ and MA $Bi_{0.5}Sb_{1.5}Te_3$ with 8wt% extra Te powder. The XRD peaks for both samples are consistent with standard pattern of $Bi_{0.5}Sb_{1.5}Te_3$ (JCPDS49-1713), confirming the formation of MA $Bi_{0.5}Sb_{1.5}Te_3$ as shown in Figure 5.1. The rhombohedral crystal structure of MA $Bi_{0.5}Sb_{1.5}Te_3$ with space group (R3m) remains unchanged with the addition of 8wt% extra Te [72].

Dispenser printable slurries were made by mixing MA $Bi_{0.5}Sb_{1.5}Te_3$ in epoxy resin polymer binder, which is well known and off the shelf available adhesives [51]. To form a conductive path in composite systems, the volume fraction of conductive active particles in polymer matrix should be higher than percolation threshold [52, 53]. Empirical studies, in this case, show that filler particles to epoxy volume ratio should be 45% to 55% in order to form the conductive paths. The highest volume ratio of active particles to polymer achieved was 48% to 52%, beyond which crack formation was observed in the cured film. This higher volume ratio resulted in compact films with minimal cure shrinkage and overall good thermoelectric properties.

The curing of dispenser printed films was done in the temperature range of 150°C to 350°C [56]. At curing temperatures of 150°C and 200°C films did not give adequate thermoelectric properties. One possible reason is the inadequate shrinkage of the polymer matrix upon curing to pack filler particles. Cracking was observed

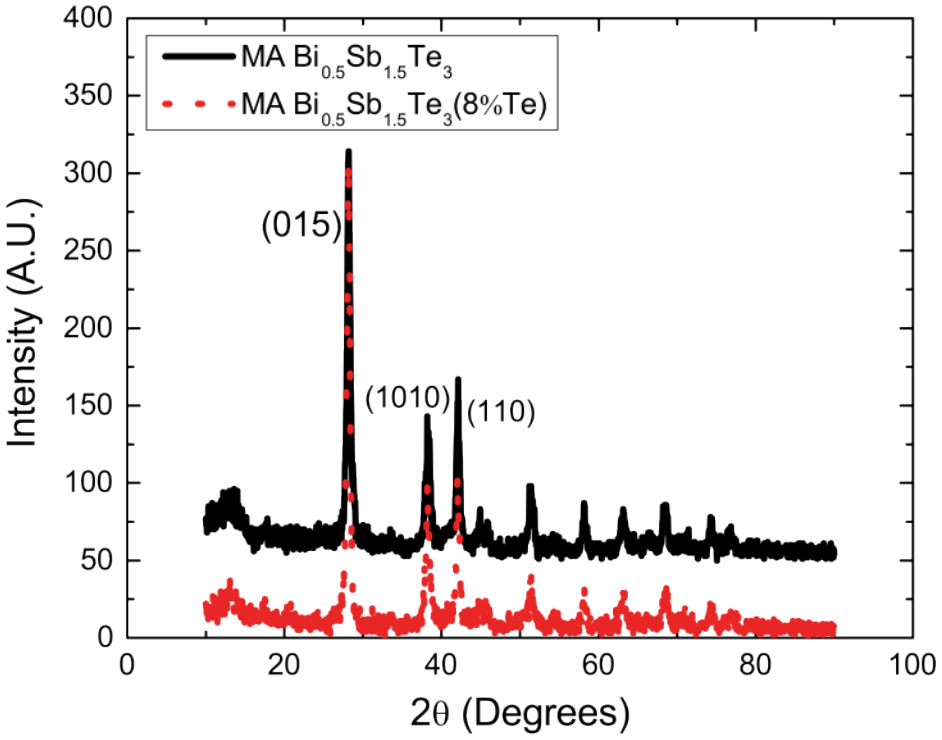

Figure 5.1: X-ray powder diffraction (XRD) patterns of MA $Bi_{0.5}Sb_{1.5}Te_3$ and MA $Bi_{0.5}Sb_{1.5}Te_3$ with 8wt% extra Te thermoelectric powders.

in films cured at or above 300°C. Therefore, p-type dispenser printed films were cured at 250°C. The curing was done for 12 hours to facilitate annealing with the objective of reducing the defects, and hence the carrier concentration, and improving the Seebeck coefficient [56]. Figure 5.2 shows SEM image of filler particles after mechanical alloying and wet grinding. From this image, it is clear that the average particle size is less than 5µm. Figure 5.3 shows a cross-section SEM image of a cured $Bi_{0.5}Sb_{1.5}Te_3$ /epoxy dispenser printed composite film. The image suggests that the epoxy polymer binder forms a solid, dense matrix when mixed and cured with active $Bi_{0.5}Sb_{1.5}Te_3$ particles. It also suggests that active particles are uniformly distributed in the polymer matrix.

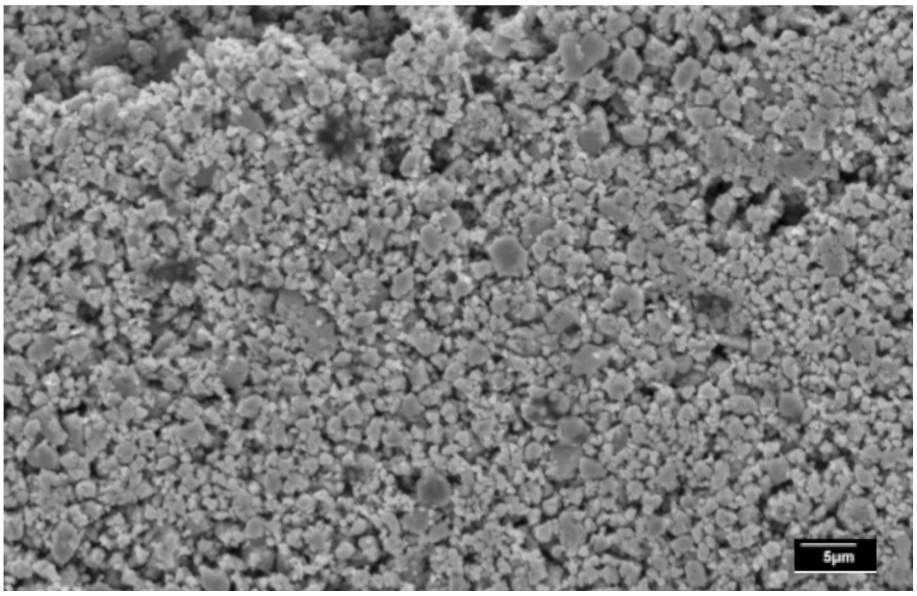

Figure 5.2: SEM micrograph of MA $Bi_{0.5}Sb_{1.5}Te_3$ p-type filler after wet grinding.

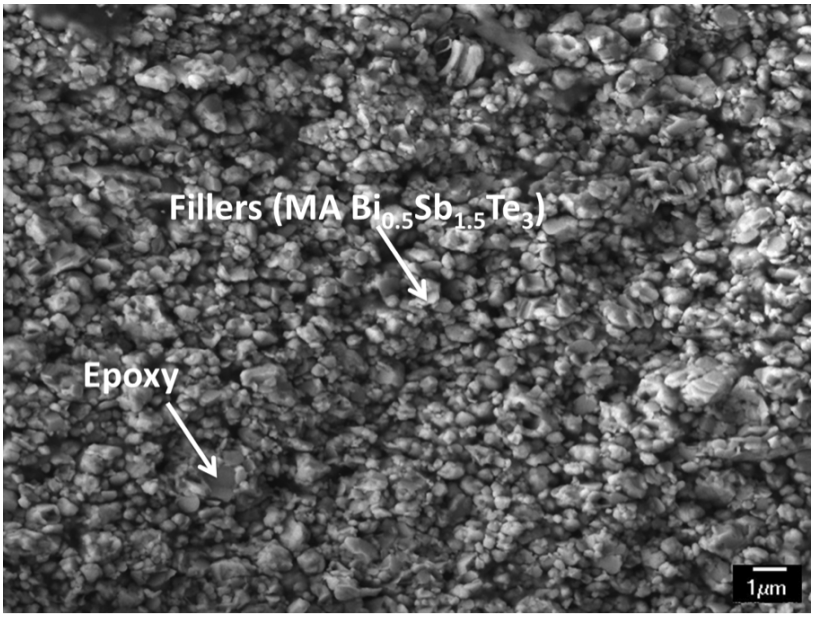

Figure 5.3: SEM micrograph of dispenser printed MA $Bi_{0.5}Sb_{1.5}Te_3$ p-type composite films cured at 250°C for 12 hours.

Electrical conductivity and Seebeck coefficient measurement of p-type composite films were done using custom built testing setup. The thermoelectric properties of p-type $Bi_{0.5}Sb_{1.5}Te_3$ thermoelectric composite films cured at 250°C for 12 hours were studied at room temperature and are shown in Figure 5.4. Error bars show the variation of measured thermoelectric properties for various samples prepared using exactly same specifications. It is clear from figure 5.4(a) that dispenser printed MA $Bi_{0.5}Sb_{1.5}Te_3$ composite films have electrical conductivities (12 S/cm) that are two orders of magnitude lower as compared to bulk $Bi_{0.5}Sb_{1.5}Te_3$ (1300 S/cm) [72]. The lower electrical conductivity is due to the non-conducting epoxy polymer matrix [62, 69, 112]. The decrease in electrical conductivity may also be due to the grain boundary scattering, which causes carrier mobility to be lower [58]. Addition of Te also did not help to improve electrical conductivity significantly. The slight increase in the electrical conductivity with addition of Te is possibly due to increased grain coalescence facilitated by the presence of extra Te which has lower melting point compared to $Bi_{0.5}Sb_{1.5}Te_3$ [56].

Figure 5.4(b) shows Seebeck coefficient variation with respect to Te as an additive. The positive value of the Seebeck coefficient confirms the material as p-type. For stoichometric MA $Bi_{0.5}Sb_{1.5}Te_3$ composite films, the Seebeck coefficient is the same (200 µV/K) as reported for bulk material [72]. According to EMT the Seebeck coefficient of a composite system depend on the effective electrical and thermal conductivity of the composite system. Since electrical conductivity of the insulating polymer is zero, effective Seebeck coefficient of composite system is the same as MA $Bi_{0.5}Sb_{1.5}Te_3$ and is related to carrier concentration only [50, 58, 112]. Approximately 50% improvement in the Seebeck coefficient was observed as a result of adding extra Te. Antisite defects are created in the $Bi_{0.5}Sb_{1.5}Te_3$ alloy as Te sites are occupied by Bi and Sb atoms. The hole concentration of p-type $Bi_{0.5}Sb_{1.5}Te_3$ alloy depends on the antisite defects and on the degree of Te-deficiency in the stoichiometric composition [78, 58]. Antisite defect concentration decreases with the addition of extra Te as Te-deficiency sites are replaced by extra Te. As a result, the Seebeck coefficient increases [78]. The Hall coefficient and carrier concentration measurements were done using an Ecopia-300. Hall effect measurements confirmed slightly lower bulk carrier concentration for films with extra Te, as shown in figure 5.4(c). Therefore, the Seebeck coefficient is higher for films with 8wt% extra Te.

Figure 5.4(d) shows that the power factor is highest for MA $Bi_{0.5}Sb_{1.5}Te_3$ with 8wt% extra Te composite films (1.8×10^{-4} W/m-K^2). Addition of 10% extra Te did not help to improve the thermoelectric materials properties any further. Therefore, we chose MA $Bi_{0.5}Sb_{1.5}Te_3$ with 8wt% extra Te for making the TEGs. A transient plane source with C-therm TCi thermal conductivity analyzer was used to measure the

thermal conductivity. The thermal conductivity of MA $Bi_{0.5}Sb_{1.5}Te_3$ with 8wt% extra Te dispenser printed film was 0.24 W/m-K. Lower thermal conductivity as compared to the bulk (1.1 W/m-K) is due to the insulating nature of epoxy. Additionally, fine grain (5µm) active filler particles increase the potential barrier scattering that also contributes to lower thermal conductivity [112]. A maximum ZT of 0.2 was achieved for dispenser printed MA $Bi_{0.5}Sb_{1.5}Te_3$ with 8wt %Te composite films.

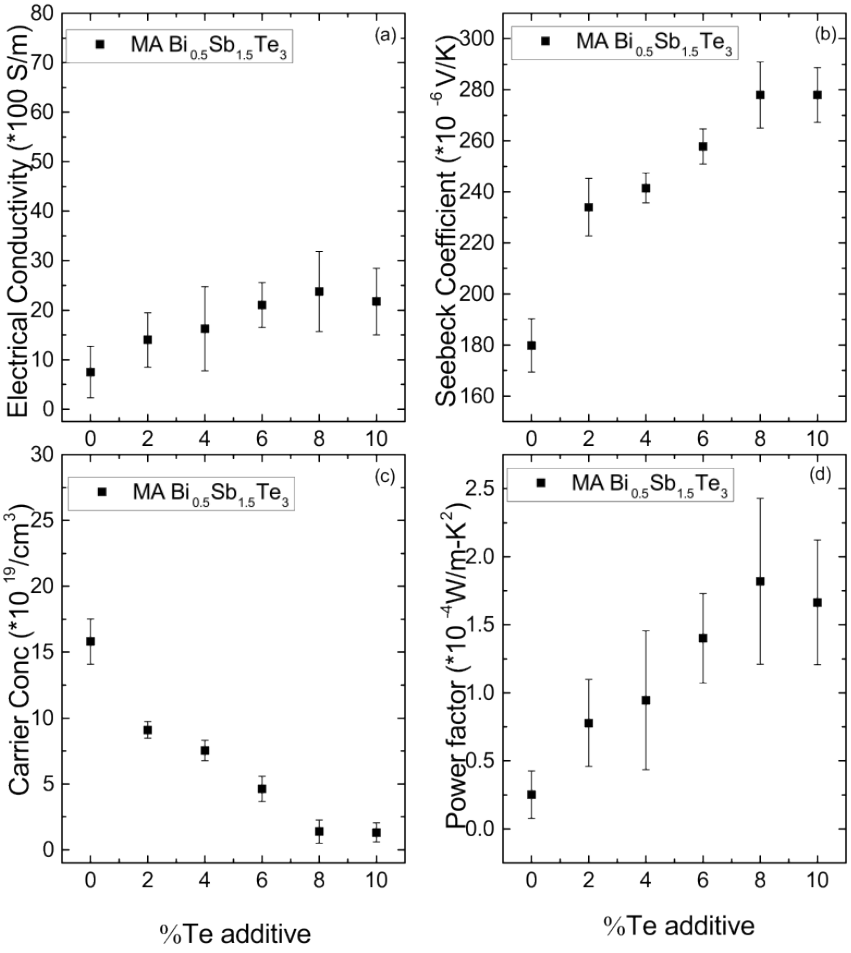

Figure 5.4: Thermoelectric properties of dispenser printed MA $Bi_{0.5}Sb_{1.5}Te_3$ composite films as a function of extra Te wt% including electrical conductivity (a), Seebeck coefficient (b) carrier concentration (c) and power factor (d).

5.4 Device Fabrication

Although the device geometry of a TEG depends on the specific application, high density and high aspect ratio are desirable for various low waste heat applications [87, 96]. A sixty leg planar TEG was dispenser printed on flexible substrate fabricated by Rigiflex Technology Inc [58]. The planar thermoelectric device was fabricated using dispenser printed MA p-type $Bi_{0.5}Sb_{1.5}Te_3$ with 8wt% extra Te polymer composites slurries. The printed TEG device was cured in argon/vacuum oven at 250°C. Electrical connections were made using silver epoxy and electrical wires. The illustration and an image of the actual device are shown in Figure 5.5. Prototype device testing was done using custom test set up within 24 hours of curing [58].

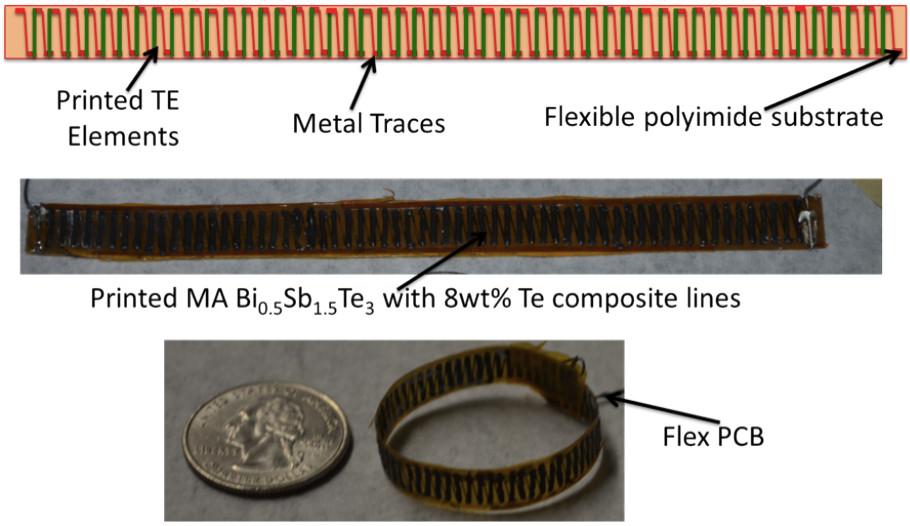

Figure 5.5: Illustration and image of dispenser printed MA $Bi_{0.5}Sb_{1.5}Te_3$ (with 8wt% extra Te) p-type planar thermoelectric device on flex PCB substrate.

5.5 Printed Device Performance

The device resistance of the prototype was 800Ω when cured at 250°C. To measure the power output of the device a variable resistance was attached in series to the device. The maximum power output of the device occurs when the load resistance matches the device resistance as shown in Figure 5.6.

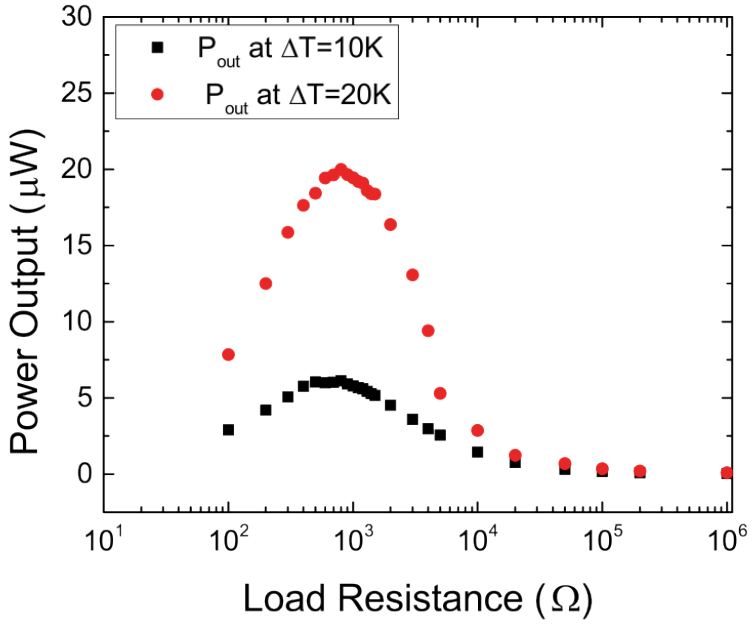

Figure 5.6: Power output of TEG device as a function of load resistance at ΔT=10K and 20K.

Figure 5.7 shows the device characteristic curve for a sixty-element prototype device measured at ΔT of 10 and 20K at various load resistances. At matched load resistance, the device produces approximately 20.5μW at 0.15 mA and 130 mV closed circuit voltages at 20K temperature difference. Open circuit voltage at 20K temperature difference is 260mV. At 10K temperature difference maximum power output is 5.5μW and open circuit voltage obtained is 130mV. Power output of the thermoelectric device is given by the following equation

$$P_{max} = \frac{V_{op}^2}{4R_{in}}$$

where

$$V_{op} = m\alpha\triangle T$$

and

$$R_{in} = \rho\frac{ml}{A}$$

where V_{op} is the open circuit voltage, m the number of couples, α the Seebeck co-efficient and ΔT the temperature difference across the device. R_{in} is the internal resistance of the device; ρ is the electrical resistivity of the composite p-type films; l (5mm) and A (600μm$\times$120μm) are the length and cross sectional area of the thermo-element.

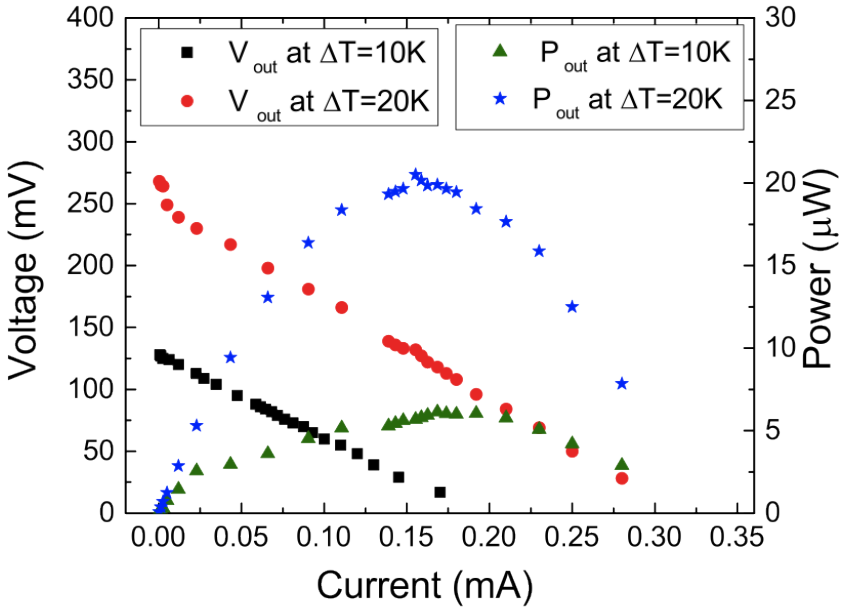

Figure 5.7: Power output graph of the single thermo-element TEG device at ΔT=10K and 20K.

The variation of power density (power per unit area) with temperature difference for ideal model, fitted model, and actual measurements of the prototype is plotted in figure 5.8. The power density for the ideal model was calculated using thermoelectric materials properties of MA $Bi_{0.5}Sb_{1.5}Te_3$ with 8 wt% extra Te composites films cured at 250°C and is shown by solid line in figure 8 [21, 87]. Figure 5.8 shows that a maximum power density of 172μW/cm^2 can be obtained for TEG devices at ΔT of 20K for the ideal model.

For fitted model, power density is calculated based on internal resistance of the device (800 Ω) and Seebeck coefficient of composite films. The power density value for the fitted model and the ideal model matched at ΔT of 10K and 20K suggesting negligible contact resistance of the TEG device. The actual measured power density

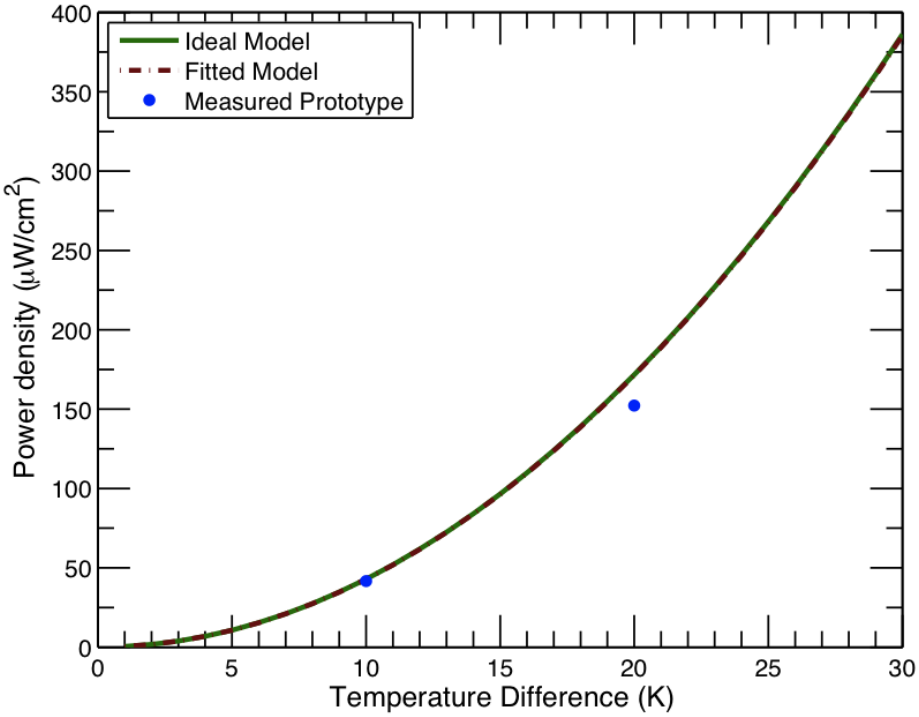

Figure 5.8: Power density vs. temperature difference across the device for ideal model, fitted model and actual prototype TEG.

values are calculated by dividing the maximum power output of the TEG device, produced at ΔT of 10K and ΔT of 20K, by the area of the device. It is clear from figure 5.8, that a p-type single-element TEG is capable of attaining a power density of 40μW/cm^2 at ΔT of 10K. However, at ΔT of 20K actual measured power density (152μW/cm^2) is slightly lower than ideal model (172μW/cm^2). The graph also indicates that in the higher temperature difference region power density deviation between the ideal model and actual prototype increases. The difficulty in maintaining a high temperature difference across the TEG possibly results in different power densities for the ideal and the actual prototype. Another important thing to notice in figure 5.8 is, P_{max} is proportional to $(\Delta T)^2$ as Pmax depends on the square of the open circuit voltage and the open circuit voltage is proportional to ΔT. The printability of the composite materials allow for a cost-effective, scalable and high-density fabrication method for TEGs. While this work demonstrates the feasibility

of printed planar TEGs, further application design can be investigated.

5.6 Conclusions

1. MA p-type $Bi_{0.5}Sb_{1.5}Te_3$ composite was developed for fabricating thermoelectric devices using a dispenser printer.

2. The Seebeck coefficient of MA p-type $Bi_{0.5}Sb_{1.5}Te_3$ was enhanced by adding 8wt% extra Te.

3. Increase in the Seebeck coefficient and reduction in the thermal conductivity helped to achieve ZT of 0.2.

4. A sixty-element planar prototype device was printed on a custom designed flexible polyimide substrate to form a TEG.

5. The device produced 20.5μW power at 0.15mA and 130mV for 20K temperature difference. These results indicate an areal power density of 150μW/cm^2.

6. The results shown are promising for the use of low-cost and scalable TEGs for various low-power energy harvesting applications.

Chapter 6

Practical Printed Flexible Thermoelectric Generators for Use on Low Levels of Waste Heat

6.1 Overview

In chapters 4 and 5, improvements in the figure of merit of n-type Bi_2Te_3 and p-type $Bi_{0.5}Sb_{1.5}Te_3$ with help of additives was presented. In this chapter, we explore Bi as n-type thermoelectric composite material as it is relativily inexpensive and easily available. Also, it is less toxic compared to commonly used thermoelectric materials like Bi_2Te_3. We present a unique way of fabricating circular TEGs using dispenser-printing methods, which can be easily mounted on a hot surface or wrapped around pipes carrying hot fluid to generate electricity to power condition monitoring sensors. In order to realize practical thermoelectric devices, both p-type and n-type elements connected in series are essential to achieve reasonable efficiency. Therefore, Bi-epoxy has been used as n-type composite thermoelectric material and MA $Bi_{0.5}Sb_{1.5}Te_3$ with 8wt% extra Te epoxy composites as p-type thermoelectric material to print circular TEGs.

Additionally, a 50-couple TEG, with 3.5mm×600µm×100µm printed element dimensions, is fabricated on a custom designed polyimide substrate with thick metal contacts. The prototype TEG device was tested on experimental setup where hot and cold temperature difference was maintained to achieve high temperature difference across the device. To achieve similar power output in a practical situation, such as from pipes carrying hot fluid an experimental study in forced and natural convection is performed.

6.2 Experimental

6.2.1 Device Fabrication

The main drawback of using Bi as n-type thermoelectric material is its low Seebeck coefficient and high thermal conductivity as compare to standard Bi_2Te_3. However, we still explore Bi epoxy based composite thermoelectric materials because Bi has higher electrical conductivity as compare to Bi_2Te_3 that may help to improve the electrical conductivity of Bi-epoxy composite films. Insulating epoxy may help to reduce the thermal conductivity of Bi-epoxy composite films. Therefore, Bi-epoxy was used as n-type composite thermoelectric material and MA $Bi_{0.5}Sb_{1.5}Te_3$ with 8wt% extra Te epoxy composites as p-type thermoelectric material to print circular TEGs. The preparation of Bi and epoxy based thermoelectric slurries were same as described in chapter 3.

A high aspect ratio circular device design was used to maintain the temperature difference across the device and to achieve reasonable power output. Circular TEG device can be wrapped around heated pipe. One side of the TEG in contact with hot pipe and other in the ambient, exploits the temperature difference around heated pipe. A custom made Flex-PCB consisting of nickel and gold plated copper traces was fabricated on a flexible polyimide substrate by Rigiflex Technology Inc [96]. N-type Bi and p-type MA $Bi_{0.5}Sb_{1.5}Te_3$ composite inks were dispenser printed onto the substrate to form lines spanning across the inner and the outer contacts. Thick metal contacts resulted in reduced electrical contact resistance between metal contacts and printed TE elements. Printed lines on the flex PCB was cured in an argon/vacuum oven at 250°C.

6.2.2 Circular Device Testing Setup

Custom built test setup for circular device testing was prepared. Circular themopeltier was used as hot side. Ten small rectangular peltiers were connected in series to form a circular shape and were maintained as cold side. Circular TEG device was placed in such a manner that one side of thermo elements rested on hot side peltiers and other side on cold side as shown in figure 6.1. A schematic of the custom made setup for the power output measurements and the dispenser-printed 10-couple circular TEG prototype is shown in figure 6.1(a) and figure 6.1(b). Series of temperature differences was applied across the dispenser printed prototype device. Temperatures at the both ends of the elements were monitored to ensure that a steady state was reached and open circuit voltage was measured. Closed circuit voltage measurements were taken at multiple load resistance values. The power

output was calculated using the measured voltage and load resistance at various temperature differences.

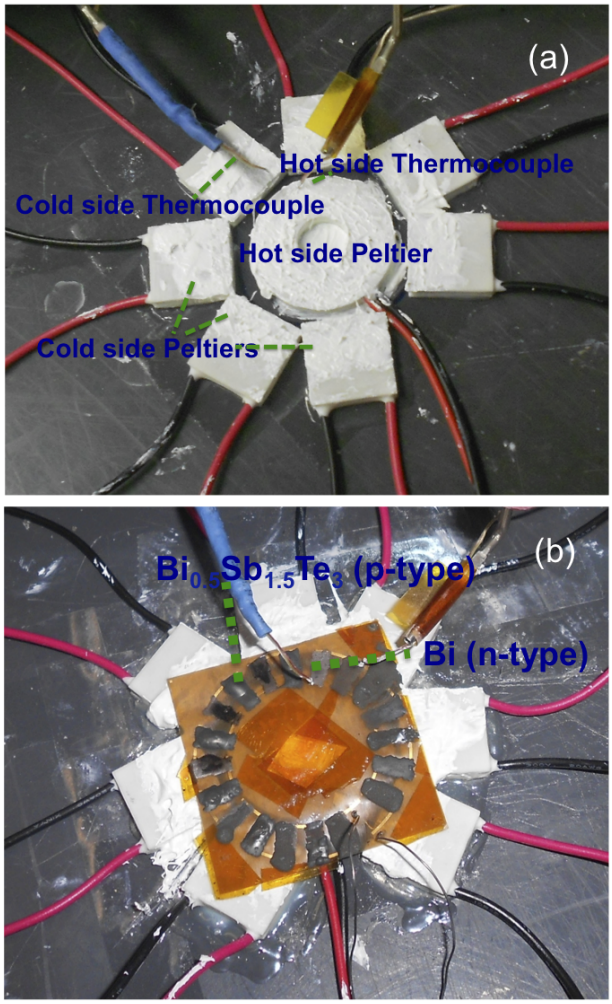

Figure 6.1: Image of custom built measurement set up and printed circular thermoelectric device on the setup.

6.2.3 Thermoelectric Property Characterization

N-type Bi-epoxy and p-type MA $Bi_{0.5}Sb_{1.5}Te_3$-epoxy slurries were dispenser printed as thick films on glass substrate for thermoelectric characterization purposes and cured at 250°C. Figure 6.2 shows the thermoelectric properties of n-type Bi-epoxy and

p-type $Bi_{0.5}Sb_{1.5}Te_3$ with 8wt% extra Te-epoxy films cured at 250°C, as a function of temperature. Error bars show the variation of measured thermoelectric properties for various samples prepared using exactly same specifications. Bi has approximately one order of magnitude higher electrical conductivity (9000 s/cm) as compared to bulk $Bi_{0.5}Sb_{1.5}Te_3$ (1300 S/cm) [72]. Electrical conductivity of n-type Bi epoxy as well as MA p-type $Bi_{0.5}Sb_{1.5}Te_3$ epoxy composites are almost two orders of magnitude lower than the bulk due to the insulating nature of epoxy polymer present in composite films. Additionally, figure 6.2(a) indicates Bi epoxy composites have one order magnitude higher electrical conductivity (110 S/cm) as compare to MA p-type $Bi_{0.5}Sb_{1.5}Te_3$ with 8wt% extra Te-epoxy films (11 S/cm). Bi epoxy composite films have one order magnitude higher electrical conductivity as compare to MA n-type Bi_2Te_3 dispenser printed films cured at 250°C [58]. Almost no variation in electrical conductivity with temperature was observed for n-type and p-type composite films as shown in figure 6.2(a).

Figure 6.2(b) shows Seebeck coefficient variation of n and p-type thick films with temperature. For Bi composite films Seebeck co-efficient is same as bulk (84 μV/K) when cured at 250°C. Similarly, for MA p-type films, Seebeck coefficient is positive and same as bulk value (250 μV/K) [72]. This behavior of the composite film can be explained on the basis of effective medium theory. Seebeck coefficient of composite system depends on electrical and thermal conductivity. Electrical and thermal conductivity of insulating epoxy polymer is almost zero; so effective Seebeck coefficient of composite system is same as active filler particles [58]. Therefore, MA composite printed films cured at 250°C for 12 hrs have Seebeck coefficient same as bulk value. With increase in temperature up to 90°C there is almost no change in Seebeck coefficient was observed in n and p-type composite films as shown in figure 2(b).

Figure 6.2(c) shows that power factor is same for $Bi_{0.5}Sb_{1.5}Te_3$-epoxy based p-type films and Bi-epoxy based n-type films (8.6e-5 W/m-K^2). As the electrical conductivity and Seebeck coefficient did not change with temperature the power factor did not change much with temperature. Therefore, in the temperature range of 20 to 90°C, composite films are not adversely affected by the temperature increment.

6.2.4 Circular Device Results and Discussion

To demonstrate the circular prototype, Bi-epoxy as n-type and MA $Bi_{0.5}Sb_{1.5}Te_3$ with 8wt% extra Te-epoxy as p-type thermo-elements were printed on flex-PCB. For specific applications, it is possible to design the TEG device to optimize the power output for given temperature differences. However, for demonstration purposes a

non-optimized geometry was chosen. The device resistance of the prototype was 100Ω when cured at 250°C. Open circuit voltage for 10-couple n and p-type thermo-element connected in series was 230mV at 70K temperature difference. It corresponds approximately to sum of thermovoltage of each unit cell (0.270+0.084)×10×70=245mV.

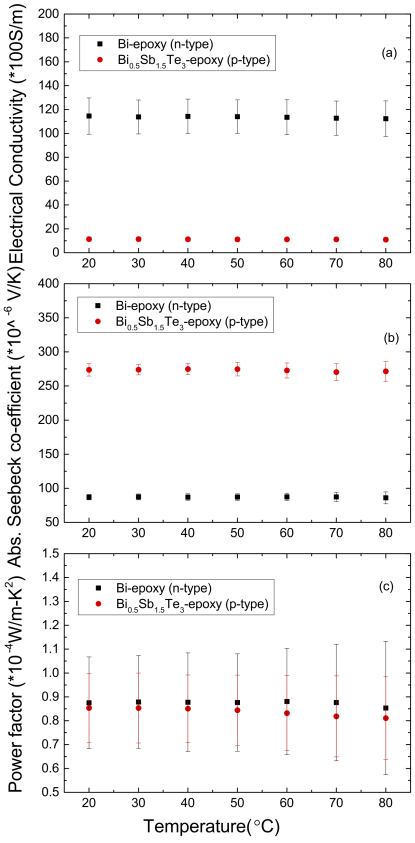

Figure 6.2: Thermoelectric properties of n-type Bi epoxy and p-type MA $Bi_{0.5}Sb_{1.5}Te_3$ epoxy composite films cured at 250°C as a function of temperature.

To measure the power output of the device a variable resistance was attached in

series to the device. The maximum power output of the device occurs when the load resistance matches the device resistance. Figure 6.3 shows the device characteristic curve for a 10-couple circular prototype device measured at ΔT of 20K, 40K and 70K at various load resistances. At matched load resistance, the device produces approximately 130µW at 1.145mA current and 114.5mV closed circuit voltages at 70K temperature difference. At 20K and 40K temperature differences maximum power outputs are 8.5µW and 30.5µW and closed circuit voltages obtained are 30mV and 55mV respectively.

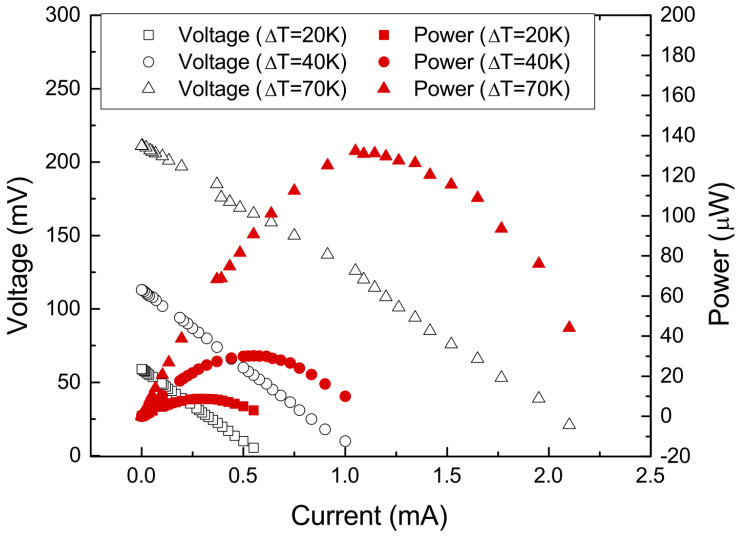

Figure 6.3: Characteristics curve of the ten-couple circular TEG device at ΔT= 20K, 40K and 70K.

Figure 6.4 shows the measured power density and fitted model power density of the device as a function of the temperature difference. The power density in the fitted model was calculated using thermoelectric voltage produced by n and p-type dispenser printed composites films and using internal resistance of TEG device and plugging these numbers into power equation written above. The maximum power density of 1370µW/cm^2 can be obtained for TEG devices at ΔT (70K) using fitted model. However, at ΔT of 70K actual measured power density (1230µW/cm^2) is slightly lower than ideal model (1370µW/cm^2). Similarly at 40K temperature difference fitted model power output (440µW/cm^2) is slightly higher than actual (365µW/cm^2). At 20K temperature difference actual power output (77µW/cm^2) is

same as fitted (77μW/cm^2). The deviation at higher temperature difference may be due to fluctuations in the temperature across the device during measurement as it becomes more difficult to maintain high temperature difference across the device.

Power density of 75μW/cm^2 (temperature difference 20K) is previously reported for the planar TEG prototype using Bi_2Te_3 and Sb_2Te_3[7]. While, Bi_2Te_3 was replaced by relatively inferior thermo-electric material Bi, we achieved similar device performance. The advantage of using Bi over Bi_2Te_3 is that it is cheaper, less toxic and easily available. The power generated by 10-couple circular TEG device is sufficient to power, condition monitoring wireless sensors used at hot surface equipment such as motors, pumps and steam pipes. The versatility of printed fabrication processes allows for rapid customization by varying the printed element length, width and thickness through printing parameters. For future work, we would like to explore cheaper and less toxic alternative for p-type MA $Bi_{0.5}Sb_{1.5}Te_3$.

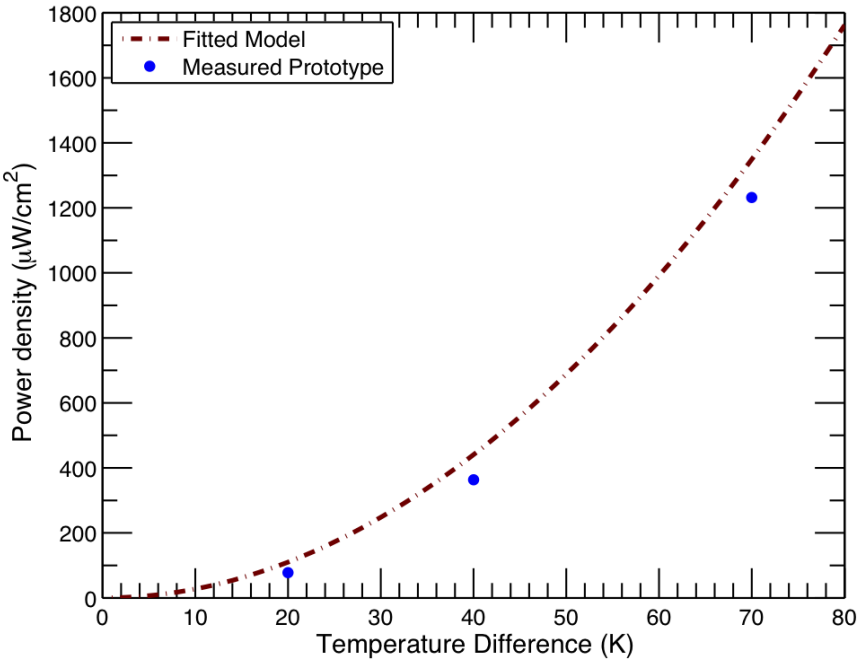

Figure 6.4: Power density at matched load resistance as a function of temperature difference across the TEG for fitted model (dotted line), measured device (circular shape).

6.3 Planar Thermoelectric Device

In chapter 2, we discussed the design of TEG based on bulk materials. However for printing purposes, we are using thermoelectric slurries. The TEG device design was done using MA n-type Bi_2Te_3 with 1wt% Se and p-type $Bi_{0.5}Sb_{1.5}Te_3$ with 8wt% extra Te-polymer composites film properties. Details of the synthesis of composite materials and their thermoelectric properties can be found in chapters 4 and 5. The fundamental voltage and power equations described in chapter 2 will serve as a platform for the design of generators for powering wireless sensor network for low waste heat application. As design-modeling studies in chapter 2 showed that power output depends on thermo-element leg length, so for modeling purpose we choose thermo element leg length to be variable; other parameters are fixed and values are shown in table 6.1 [22, 79, 87]. The Seebeck co-efficient of n and p-type composite films is 180µV/K and 280µV/K [58, 59]. Electrical conductivity of n and p-type composites films is 30S/cm and 1300S/cm [58, 59]. Thermal conductivity of n and p-type composites films is 0.25W/m-K [58, 59]. Based on the composite thermoelectric film properties and fixed design parameters we have plotted power output vs. thermo element length for a temperature difference 20K as shown in figure 6.5. Maximum power output of 38µW occurs at 3.47mm leg-length at ΔT of 20K.

w (width)	s (spacing)	t (thickness)	m (#of couples
0.6e-3m	0.5e-3m	100e-6m	50

Table 6.1: Design parameters for TEG.

Based on this optimized leg-length (3.5mm), a custom-designed, double-layer, flexible printed circuit board (Flex-PCB) was fabricated by Rigiflex, Inc [96]. The planar thermoelectric device was fabricated from the n and p-type composite slurries. The printed TEG was cured in argon/vacuum oven at 250°C. Electrical connections were made using silver epoxy and electrical wires. The illustration and an image of the actual device are shown in figure 6.6.

6.3.1 Planar Device Measurement Setup

The printed prototype device was tested using a custom experimental testing apparatus as shown in figure 6.7 [58].

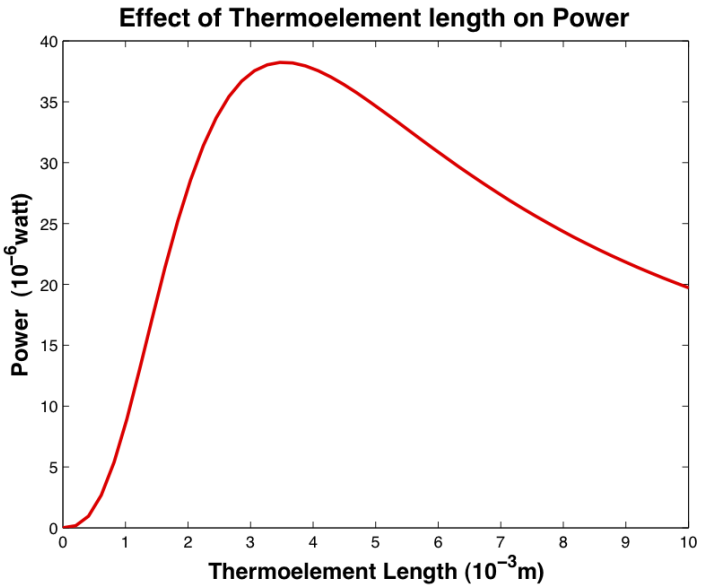

Figure 6.5: Effect of thermo-element leg length on power at ΔT of 20K.

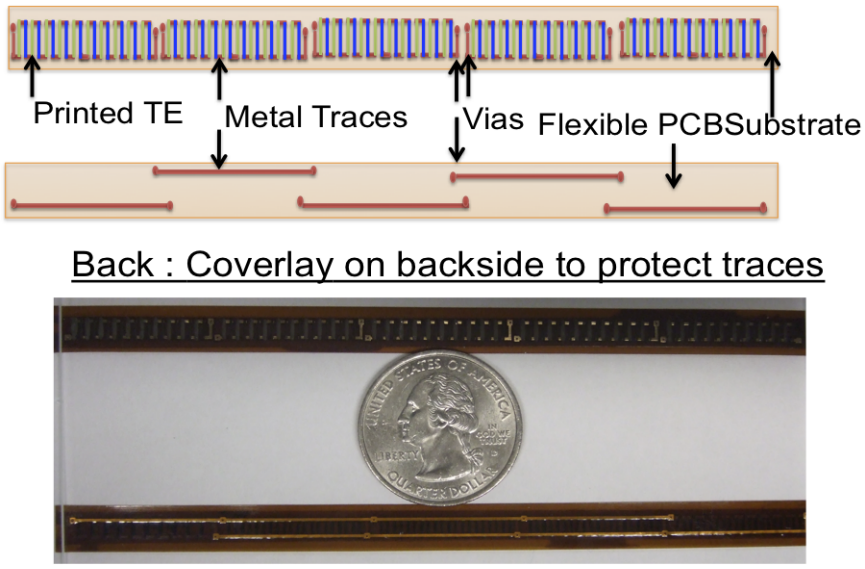

Figure 6.6: Illustration and image of dispenser printed MA Bi_2Te_3 (1 wt% Se) n-type and MA $Bi_{0.5}Sb_{1.5}Te_3$ (8%Te) p-type planar thermoelectric device on flexible polymide substrate.

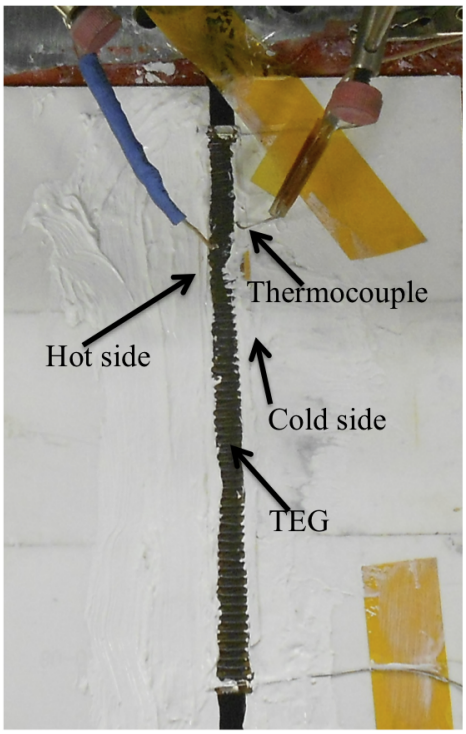

Figure 6.7: Image of custom built experimental setup for TEG device power output measurement.

The practical situation of waste heat around a hot pipe was simulated in the laboratory by using 0.3048m hollow 'schedule 40' pipe as shown in figure 6.8. Heavy duty silicone rubber heat sheets were placed inside the pipe for heating. The outer surface area of the pipe was wrapped in an insulating silica sheet to maintain the hot side temperature of pipe. One thermocouple was placed underneath the insulating sheet in contact with the hot surface of the pipe to measure the hot surface temperature. The heat sheets could increase the temperature of the hot pipe up to 180°C. To precisely control the hot pipe temperature a PID controller was used. A small fan was used to create forced convection. A small slit in the insulating silica sheet was created to fit the TEG so that bottom side of the TEG device was in contact with the hot pipe and the upper side of the TEG was in the ambient environment. Thermal joint compound (TIM-417, Wakefield Solutions) was applied at the contact interfaces to reduce contact thermal resistance. Various temperature differences were then applied across the printed TEG using the PID controller. The open circuit voltage and power output were measured.

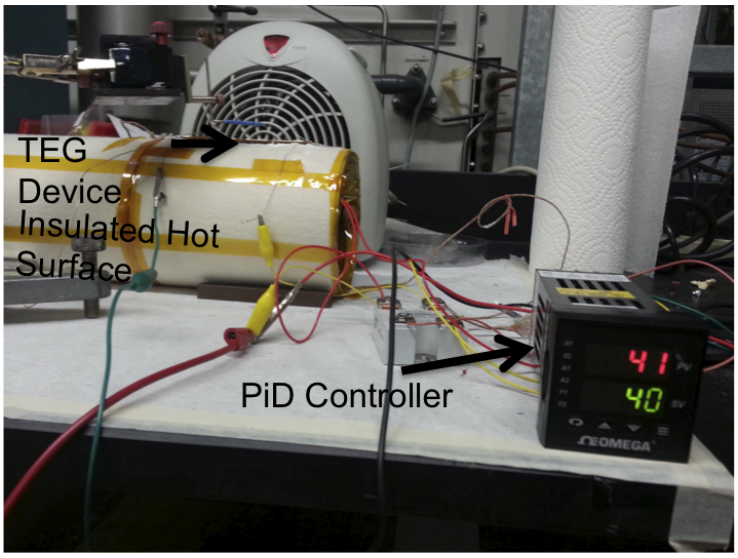

Figure 6.8: Image of insulated hot pipe set up in lab.

6.4 Results and Discussion

6.4.1 Materials Property Characterizations

To demonstrate the planar device prototype we choose previously developed MA Bi_2Te_3 with 1wt% Se as n-type material and MA $Bi_{0.5}Sb_{1.5}Te_3$ with 8 wt% extra Te as p-type [58, 59]. These composite films have poor temperature resistance and are therefore unsuitable for use at high temperatures. Furthermore, these materials have inferior thermoelectric properties to those of some inorganic thermoelectric materials. To realistically apply these thermoelectric materials, applications which operate in the low temperature range (<100°C) need to be targeted. For low waste heat application, thermoelectric device perform from room temperature to a moderate temperature range. Therefore, it is necessary to measure thermoelectric properties of these dispenser printed composite materials from room to moderate temperature range. Figure 6.9 shows the measured thermoelectric properties of MA n-type and p-type film cured at 250°C in temperature range from 20°C to 90°C. Figure 6.9(a), 6.9(b) and 6.9(c) show that electrical conductivity, Seebeck coefficient and power factor do not change with the change in temperature in the range of 20°C to 90°C. Error bars show the variation of measured thermoelectric properties for various samples prepared using exactly same specifications. The thermoelectric properties of composite films are not adversely affected in the temperature range of 20°C to 90°C.

Therefore, the TEG device made using dispenser printed composite films can be used in that temperature range.

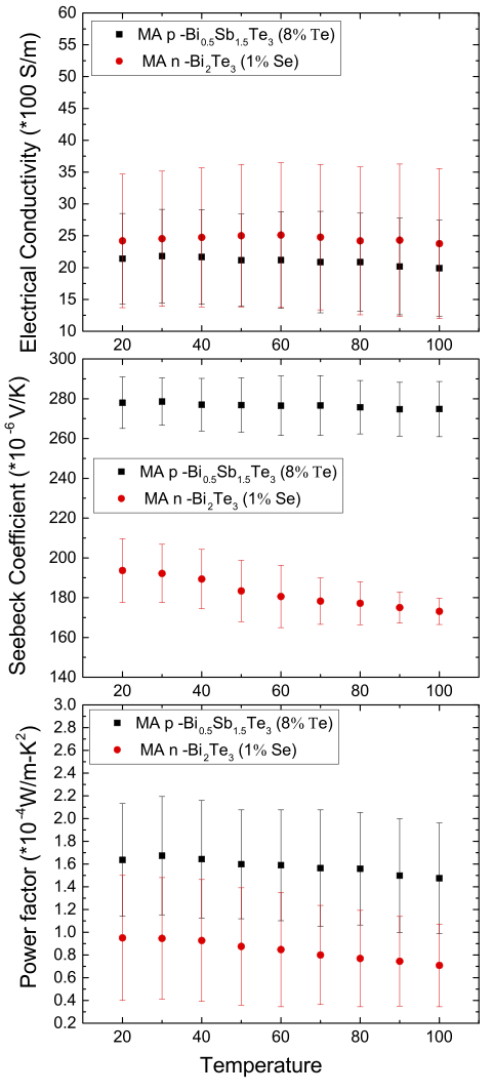

Figure 6.9: Thermoelectric properties of n and p-type dispenser printed composite films as a function of temperature including electrical conductivity (a), Seebeck coefficient and power factor (c).

6.4.2 Printed Device Performance

Using the n and p-type composites slurries, thermo-elements were printed on a flexible PCB substrate. The device resistance of the prototype was 55Ω when cured at 250°C. A variable resistance was attached in series to the TEG device and voltage measurements were taken at multiple load resistances. The power was calculated based on the measured voltage and load resistance at various temperature differences. Figure 6.10 shows the power output graph for the 50-element series parallel combination prototype device measured at ΔT of 10 and 20K. At ΔT of 20K, printed TEG device produced maximum power of 33µW at 0.77mA current and 44mV closed circuit voltage. Open circuit voltage at ΔT of 20K was 88mV. At ΔT of 10K the maximum power output was 8 µW and closed circuit voltage obtained was 21mV.

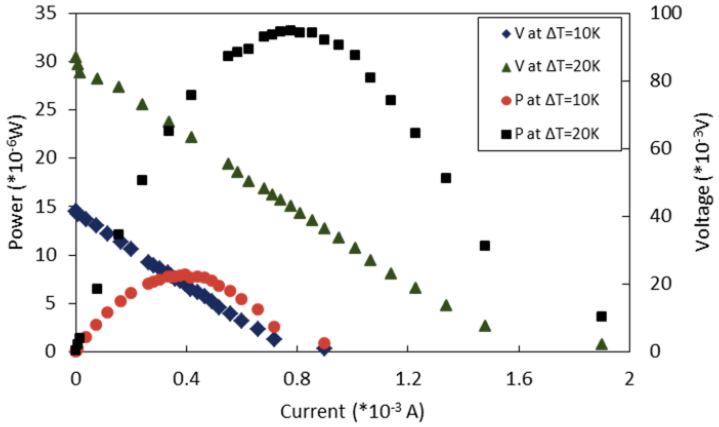

Figure 6.10: Power output curve of the 50 printed couples TEG device at temperature difference of 10K and 20K.

Figure 6.11 shows the variation of power density (power output per unit area) of the TEG with the temperature difference for ideal model, fitted model and actual prototype. Using thermoelectric material properties of MA Bi_2Te_3 (1wt% Se) with epoxy as n-type and MA $Bi_{0.5}Sb_{1.5}Te_3$ (8% Te) with epoxy as p-type composites films cured at 250°C, the theoretical power density(power per unit area) of TEG devices has been predicted for ideal model [22, 87]. A maximum power density for ideal model at temperature difference of 20K was 3.50 W/m^2.

For fitted model, power density is calculated based on internal resistance of the device (800 Ω) and Seebeck coefficient of composite films. It is clear from figure 6.11

that the fitted model and ideal model have same power density value at temperature difference of 10K and 20K, implying contact resistance is almost negligible for TEG device. The actual power density values are calculated by dividing the maximum power output of TEG device, produced at ΔT of 10K and 20K, by the area of the device. The actual device is capable of achieving a power density of 0.87W/m^2 at ΔT of 10K. However, at temperature difference of 20K actual measured power density (2.80W/m^2) varies from the ideal model (3.50 W/m^2). The slight variation may be due to fluctuations in temperature across the TEG during measurement and it is very difficult to maintain high temperature difference across the device in practice. This might be the reason of getting lower power density in actual prototype than ideal model.

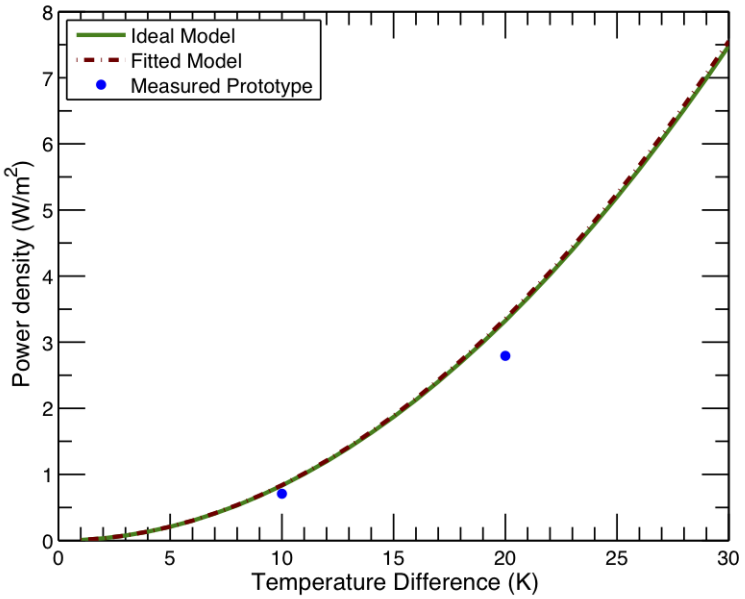

Figure 6.11: Variation of Power density as a function of temperature difference across the printed device for ideal model, fitted model and actual measured prototype.

An important thing to note in power output measurements was, we were maintaining the hot and cold side temperatures. But in a real situation such as exhaust pipes or engine manifolds of automobiles, steam pipes, etc, it is not possible to maintain the ambient side temperature. In these scenarios the use of TEGs to generate useful energy requires examination. As described in section 6.3 we have simulated the test set up of a waste heat situation from a heated pipe in the laboratory. Using

the same device with 55Ω resistance and maintaining the temperature difference of hot pipe at 60°C, 80°C and 100°C, power output measurement was done. A small fan was used for creating the forced convection. In forced convection, at 100°C hot surface pipe temperature, when the external load resistance matches the device internal resistance, a maximum power of 33µW was obtained. It was approximately the same power as in the experimental situation with hot and cold side temperatures controlled to give a 20K temperature difference across the TEG. At 80°C and 60°C pipe surface temperature, maximum power outputs obtained at matched load resistance were 21µW and 9µW respectively which was equivalent to 15K and 10K temperature difference. Figure 6.12 shows the device characteristic curve for the 50-element device measured at hot surface pipe temperature T = 100°C, 80°C and 60°C at various load resistances.

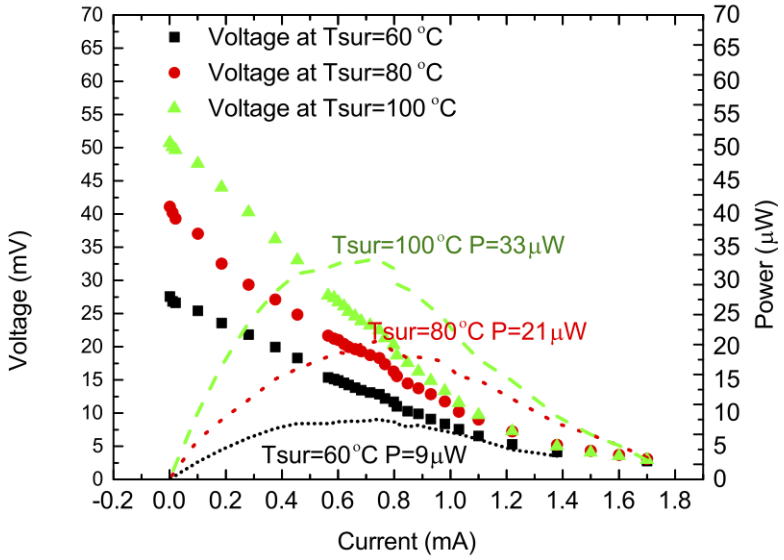

Figure 6.12: Characteristics curve of the 50 element TEG device at hot pipe temperature T=100°C, 80°C, 60°C respectively.

In natural convection, at 100°C pipe surface temperature, maximum power of 8µW was obtained which is equivalent to 10K temperature difference in experimental situation where the hot and cold side temperatures were controlled. Maximum power of 4.6µW and 2µW was obtained at 80°C and 60°C pipe temperature respectively. In natural convection experiment, it was difficult to maintain high temper-

ature difference between hot and cold side and lot of temperature fluctuation was observed. Future work will include device design optimization with inbuilt heat sinks to maintain a large temperature difference in natural convection.

Many of these devices can be stacked together to generate high power output. Power generated by these stacked TEG devices is sufficient to charge batteries used in wireless sensors/transmitters used in the monitoring of equipment with hot surfaces such as motors, pumps and steam pipes that are used in aerospace, power plants, processing industries, residences and geothermal industries [96]. The successful demonstration of planar thermoelectric generators opens opportunities for a wide variety of energy harvesting applications. The developing medical and healthcare needs of the world will place demands on more complex diagnostic and treatment technologies that require autonomous power sources. Given the limitations of primary battery systems, thermoelectric generators provide a solid-state solution to alleviate the power demands of current and future technologies.

6.5 Conclusions

1. In summary, Bi is cheaper, easily available and less toxic compared to Bi_2Te_3. Bi-epoxy based composite films have power factor similar to Bi_2Te_3. Therefore, it is preferable to use Bi-epoxy based composite materials for printing high aspect ratio devices.

2. We demonstrated a novel way of printing circular TEG devices that can be wrapped around pipes carrying heated fluids to power condition monitoring sensors. The maximum power output of 130µW at 70K temperature difference is achieved for a 10-couple device that resulted in measured power density (1230µW/cm^2).

3. A 50-element planar prototype was printed on a custom designed flexible polyimide substrate to form a TEG with thermo element leg-length of 3.5mm.

4. The device produced 33µW at 0.75mA and 43mV for a 20K temperature difference on custom test apparatus. These results indicate an areal power density of 280µW/cm^2.

5. 33µW power output was achieved when the TEG was applied to a pipe surface with temperature of 100°C in forced convection. While, in natural convection, 8µW power was obtained at 100°C pipe surface temperature.

6. The results shown are promising for the use of low-cost and scalable TEGs for various low-power energy harvesting applications or powering autonomus wireless sensor networks.

Chapter 7

Summary and Future Work

7.1 Summary

Thermal energy harvesting power sources have received significant research attention primarily due to the growth of autonomous monitoring applications utilizing WSNs. These power sources utilize the waste heat available in applications such as heat engines, car exhausts, and pipes carrying hot fluid to generate electricity. This work presents design, fabrication and testing of cost effective TEG devices. A novel method to synthesize thermoelectric materials to print scalable TEG devices for low waste heat application is presented. A custom developed dispenser printer is utilized for printing TEG devices. Optimization of processing parameters to enhance the ZT of n and p-type thermoelectric composite slurries is also included. MA with controlled amount of dopant helped improve ZT of the n and p-type slurries. The prototype TEG was printed on a custom designed flexible substrate to reduce the contact resistance. Device power output measurements were done on a custom measurement setup. Apart from a conventional measurement setup using maintained temperature difference across TEG, a practical situation of low waste heat around a pipe was simulated in the laboratory. The power output measurements were done in forced and natural convection. Findings of this work are summarized below.

1. The heat transfer modeling shows that low grade waste heat sources provide sufficient temperature differences across the TEG.

2. Thick film TEGs have the potential to enable large scale deployment of WSNs.

3. Direct write printing, a cost effective and easily automated technique, is suitable for fabricating thick film TEGs.

4. N-type Bi_2Te_3-epoxy and p-type Sb_2Te_3-epoxy thermoelectric composite materials were successfully developed for printing thermoelectric devices.

5. A maximum ZT of 0.41 was achieved for the Sb_2Te_3 composite films whereas the best ZT for Bi_2Te_3 composite films was only 0.18 when films were cured at 350°C for 12hrs.

6. Thermoelectric properties of MA n-type Bi_2Te_3 were enhanced by addition of 1wt% Se. A maximum ZT of 0.31 was obtained for 1wt% Se MA Bi_2Te_3 composite films when cured at 350°C.

7. A sixty two single-element TEG device was printed on a custom designed flex-PCB substrate using MA n-type $Bi_2Te_3$with 1wt% Se. The device produced 25µW at 0.23mA and 109mV for 20K temperature difference. These results indicate an areal power density of 130µW/cm^2.

8. MA p-type $Bi_{0.5}Sb_{1.5}Te_3$ with 8% Te composite was successfully developed. A sixty single-element device fabricated using the composite slurries produced 20.5µW power at 0.15mA and 130mV for 20K temperature difference.

9. A novel circular TEG device was printed using Bi and $Bi_{0.5}Sb_{1.5}Te_3$ inks. The device can be wrapped around pipes carrying heated fluids and utilize the temperature difference to generate power. A maximum power output of 130µW at 70K temperature difference was achieved for a 10-couple device that resulted in measured power density of 1230µW/cm^2.

10. A 50-couple prototype TEG was designed (leg length 3.5mm) and printed on a custom designed flex-PCB substrate using MA n-type $Bi_2Te_3$with 1wt% Se and MA p-type $Bi_{0.5}Sb_{1.5}Te_3$ with 8% Te. The device produced 33µW at 0.75mA and 43mV for a 20K temperature difference on a custom test apparatus. These results indicate an areal power density of 280µW/cm^2.

11. A significant drop in the power output, from 33µW to 8µW, was observed for a TEG device mounted on a 100°C pipe surface when the measurement setup was changed from forced convection to natural convection. This drop in power output suggests that it is difficult to maintain high temperature difference in a natural convection scenario.

7.2 Future Work

Printed TEGs are not as efficient as some state-of-the-art TEGs that use high ZT thermoelectric materials. The active filler particle can be replaced by higher performance TE materials. These TE materials can be realized by improving the power factor or reducing thermal conductivity. Quantum well materials such as 0-dimensional (0-D) dots, 1-dimensional (1-D) wires, and 2-D thin-film materials have shown very high ZT by reducing thermal conductivity [16, 60, 93]. Carrier concentration tuning and band structure engineering can also help to improve the ZT at high temperature for skutterudites and chalcogenedies [3, 2, 82]. Since TEGs can provide perpetual power they are attractive option as a permanent battery for medical implantable applications. However, these TEGs should have almost no toxicity. So far almost all inorganic thermoelectric materials have some extent of toxicity. Recent research on organic based polymers and natural tetrahedrite is a good example of less toxic thermoelectric materials [6, 67]. They are attractive alternatives for use in medical applications.

Epoxy polymer-based composites slurries are used for printing TEGs. Epoxy used in this work starts degrading above 300°C. Therefore, these printed TEGs can be utilized for low-grade waste heat (<200°C) applications. To target high temperature waste heat the epoxy polymer has to be replaced by some aramid polymers that can sustain high temperatures [14]. To address the heat loss in natural convection, future work can focus on device design optimization with inbuilt heat sinks to maintain a large temperature difference. On several instances a degradation in device performance was observed over a period of time possibly due to formation of micro-cracks in the cured device. Reproducibility and yield improvement are areas that need attention.

In this work, we have demonstrated small scale dispenser printed TEGs for low power generation. Dispenser printing is a cost effective, additive manufacturing process that precisely deposits and patterns layered components onto various substrates. The printing methods are also scalable toward mass manufacturing, including traditional screen and flexographic printing techniques. Using mass manufacturing technique it is possible to fabricate large scale TEGs for large scale power generation.

Bibliography

[1] Paolo Baronti, Prashant Pillai, Vince WC Chook, et al. Wireless sensor networks: A survey on the state of the art and the 802.15. 4 and ZigBee standards. *Computer communications*, 30(7):1655–1695, 2007.

[2] Kanishka Biswas, Jiaqing He, Ivan D Blum, et al. High-performance bulk thermoelectrics with all-scale hierarchical architectures. *Nature*, 489(7416):414–418, 2012.

[3] Kanishka Biswas, Jiaqing He, Qichun Zhang, et al. Strained endotaxial nanostructures with high thermoelectric figure of merit. *Nature Chemistry*, 3(2):160–166, 2011.

[4] H. Bottner, J. Nurnus, A. Schubert, and F. Volkert. New high density micro structured thermogenerators for stand alone sensor systems. In *Thermoelectrics, 2007. ICT 2007. 26th International Conference on*, pages 306–309. IEEE, 2007.

[5] Harald Bottner, Joachim Nurnus, Alexander Gavrikov, et al. New thermoelectric components using microsystem technologies. *Microelectromechanical Systems, Journal of*, 13(3):414–420, 2004.

[6] Olga Bubnova, Zia Ullah Khan, Abdellah Malti, et al. Optimization of the thermoelectric figure of merit in the conducting polymer poly (3, 4-ethylenedioxythiophene). *Nature Materials*, 10(6):429–433, 2011.

[7] A Chen, D Madan, PK Wright, and JW Evans. Dispenser-printed planar thick-film thermoelectric energy generators. *Journal of Micromechanics and Microengineering*, 21(10):104006, 2011.

[8] Alic Chen, Michael Koplow, Deepa Madan, Paul K Wright, and James W Evans. Dispenser Printed Microscale Thermoelectric Generators for Powering Wireless Sensor Networks. ASME, 2009.

[9] Alic Chen, Deepa Madan, Mike Koplow, Paul K. Wright, and James W. Evans. Dispenser printed thermoelectric energy generators. *Technical Digest PowerMEMS 2009*, pages 277–280, 2009.

[10] GV Chester and A Thellung. The law of Wiedemann and Franz. *Proceedings of the Physical Society*, 77(5):1005, 1961.

[11] S Dalola, V Ferrari, M Guizzetti, et al. Autonomous sensor system with rf link and thermoelectric generator for power harvesting. In *Instrumentation and Measurement Technology Conference Proceedings, 2008. IMTC 2008. IEEE*, pages 1376–1380. IEEE, 2008.

[12] Simone Dalola, Marco Ferrari, Vittorio Ferrari, et al. Characterization of thermoelectric modules for powering autonomous sensors. *Instrumentation and Measurement, IEEE Transactions on*, 58(1):99–107, 2009.

[13] Rabindra N Das, Konstantinos I Papathomas, John M Lauffer, and Frank D Egitto. Influence of nanoparticles, low melting point (LMP) fillers, and conducting polymers on electrical, mechanical, and reliability performance of micro-filled conducting adhesives for Z-axis interconnections. In *Electronic Components and Technology Conference, 2007. ECTC'07. Proceedings. 57th*, pages 74–81. IEEE, 2007.

[14] J. De Abajo and J.G. De la Campa. Processable aromatic polyimides. In *Progress in Polyimide Chemistry I*, pages 23–59. Springer, 1999.

[15] Francis J. DiSalvo. Thermoelectric cooling and power generation. *Science*, 285(5428):703–706, 1999.

[16] Mildred S Dresselhaus, Gang Chen, Ming Y Tang, et al. New Directions for Low-Dimensional Thermoelectric Materials. *Advanced Materials*, 19(8):1043–1053, 2007.

[17] Y Du, KF Cai, H Li, and BJ An. The Influence of Sintering Temperature on the Microstructure and Thermoelectric Properties of n-Type Bi_2Te_{3-x} Se_x Nanomaterials. *Journal of electronic materials*, 40(5):518–522, 2011.

[18] Lianhua Fan, Bin Su, Jianmin Qu, and CP Wong. Effects of nano-sized particles on electrical and thermal conductivities of polymer composites. In *Advanced Packaging Materials: Processes, Properties and Interfaces, 2004. Proceedings.*, pages 193–199. IEEE, 2004.

[19] Michael A Fonseca, Mark G Allen, Jason Kroh, and Jason White. Flexible wireless passive pressure sensors for biomedical applications. In *Tech. Dig. Solid-State Sensor, Actuator, and Microsystems Workshop (Hilton Head 2006)*, 2006.

[20] Michael A Fonseca, Jennifer M English, Martin Von Arx, and Mark G Allen. Wireless micromachined ceramic pressure sensor for high-temperature applications. *Microelectromechanical Systems, Journal of*, 11(4):337–343, 2002.

[21] Wulf Glatz, Simon Muntwyler, and Christofer Hierold. Optimization and fabrication of thick flexible polymer based micro thermoelectric generator. *Sensors and Actuators A: Physical*, 132(1):337–345, 2006.

[22] Wulf Glatz, Etienne Schwyter, Lukas Durrer, and Christofer Hierold. Bi_2Te_3-based flexible micro thermoelectric generator with optimized design. *Journal of Microelectromechanical Systems*, 18(3):763–772, 2009.

[23] H J Goldsmid and R W Douglas. The use of semiconductors in thermoelectric refrigeration. *British Journal of Applied Physics*, 5(11):386, 1954.

[24] L. M. Goncalves, Pedro Alpuim, D Michael Rowe, J Higino Correia, and Carlos Couto. Thermoelectric properties of Bi_2Te_3/Sb_2Te_3 thin films. In *Materials science forum*, volume 514, pages 156–160. Trans Tech Publ, 2006.

[25] Silas E Gustafsson. Transient plane source techniques for thermal conductivity and thermal diffusivity measurements of solid materials. *Review of Scientific Instruments*, 62(3):797–804, 1991.

[26] Heon Phil Ha, Young Whan Cho, Ji Young Byun, and Jae Dong Shim. The effect of excess tellurium on the thermo electric properties of Bi_2Te_3-Sb_2Te_3 solid solutions. *Journal of Physics and Chemistry of Solids*, 55(11):1233–1238, 1994.

[27] Rebecca A Hauser, Julia A King, Rachel M Pagel, and Jason M Keith. Effects of carbon fillers on the thermal conductivity of highly filled liquid-crystal polymer based resins. *Journal of Applied Polymer Science*, 109(4):2145–2155, 2008.

[28] Terry Hendricks and William T Choate. Engineering scoping study of thermoelectric generator systems for industrial waste heat recovery. *US Department of Energy*, 20(0):6, 2006.

[29] Jason L Hill and David E Culler. Mica: A wireless platform for deeply embedded networks. *Micro, IEEE*, 22(6):12–24, 2002.

[30] Christine Ho, James Evans, Michael Mark, et al. Technologies for an autonomous wireless home healthcare system. In *Wearable and Implantable Body Sensor Networks, 2009. BSN 2009. Sixth International Workshop on*, pages 29–34. IEEE, 2009.

[31] Christine C Ho, Daniel Steingart, James Evans, and Paul Wright. Tailoring electrochemical capacitor energy storage using direct write dispenser printing. *ECS Transactions*, 16(1):35–47, 2008.

[32] KKB Hon, L Li, and IM Hutchings. Direct writing technology-advances and developments. *CIRP Annals-Manufacturing Technology*, 57(2):601–620, 2008.

[33] DB Hyun, JS Hwang, TS Oh, Jae-Dong Shim, and NV Kolomoets. Electrical properties of the 85% Bi_2Te_3-15% Bi_2Se_3 thermoelectric material doped with SbI_3 and CuBr. *Journal of Physics and Chemistry of Solids*, 59(6):1039–1044, 1998.

[34] Dow-Bin Hyun, Tae Sung Oh, Jong-Seung Hwang, and Jae-Dong Shim. Effect of excess Te addition on the thermoelectric properties of the 20% Bi_2Te_3-80% Sb_2Te_3 single crystal and hot-pressed alloy. *Scripta materialia*, 44(3):455–460, 2001.

[35] Frank P Incropera, Adrienne S Lavine, and David P DeWitt. *Fundamentals of heat and mass transfer*. John Wiley & Sons Incorporated, 2006.

[36] Abram Fedorovich Ioffe. *Semiconductor thermoelements and thermoelectric cooling*. Infosearch London, 1957.

[37] EP James, MJ Tudor, SP Beeby, et al. An investigation of self-powered systems for condition monitoring applications. *Sensors and Actuators A: Physical*, 110(1):171–176, 2004.

[38] Yi Jia, Ke Sun, Fredrick Just Agosto, and Manuel Toledo Quinones. Design and characterization of a passive wireless strain sensor. *Measurement Science and Technology*, 17(11):2869, 2006.

[39] T. Lida K. Miyazaki and H. Tsukamoto. Micro-fabrication of Bi_2Te_3 by using micro-jet. *Proceedings of 22nd International Conference on Thermoelectrics, France, 17-21 August*, page 641, 2003.

[40] Sung K Kang and S Purushothaman. Development of conducting adhesive materials for microelectronic applications. *Journal of Electronic Materials*, 28(11):1314–1318, 1999.

[41] N Keawprak, ZM Sun, H Hashimoto, and MW Barsoum. Effect of sintering temperature on the thermoelectric properties of pulse discharge sintered $(Bi_{0.24}Sb_{0.76})_2Te_3$ alloy. *Journal of alloys and compounds*, 397(1):236–244, 2005.

[42] Jason M Keith, Carl D Hingst, Michael G Miller, Julia A King, and Rebecca A Hauser. Measuring and predicting in-plane thermal conductivity of carbon-filled nylon 6, 6 polymer composites. *Polymer composites*, 27(1):1–7, 2006.

[43] Julia A King, Rebecca A Hauser, Amanda M Tomson, Isabel M Wescoat, and Jason M Keith. Synergistic effects of carbon fillers in thermally conductive liquid crystal polymer based resins. *Journal of composite materials*, 42(1):91–107, 2008.

[44] Bryan Kirking, Janet Krevolin, Christopher Townsend, Clifford W Colwell Jr, and Darryl D D'Lima. A multiaxial force-sensing implantable tibial prosthesis. *Journal of biomechanics*, 39(9):1744–1751, 2006.

[45] Dasheng Lee. Wireless and powerless sensing node system developed for monitoring motors. *Sensors*, 8(8):5005–5022, 2008.

[46] D.M. Lee, C.H. Lim, D.C. Cho, Y.S. Lee, and C.H. Lee. Effects of annealing on the thermoelectric and microstructural properties of deformed n-type Bi_2Te_3-based compounds. *Journal of Electronic Materials*, 35(2):360–365, 2006.

[47] B. Legendre, Chhay Hancheng, S. Bordas, and M.T. Clavaguera-Mora. Phase diagram of the ternary system Ge-Sb-Te I. The subternary GeTe, Sb_2Te_3, Te. *Thermochimica Acta*, 78:141–157, 1984.

[48] Eli S Leland, PK Wright, and Richard M White. A MEMS AC current sensor for residential and commercial electricity end-use monitoring. *Journal of Micromechanics and Microengineering*, 19(9):094018, 2009.

[49] Yi Li and CP Wong. Recent advances of conductive adhesives as a lead-free alternative in electronic packaging: materials, processing, reliability and applications. *Materials Science and Engineering: R: Reports*, 51(1):1–35, 2006.

[50] Yuheng Liu, Yuanhua Lin, Zhan Shi, Ce-Wen Nan, and Zhijian Shen. Preparation of $Ca_3Co_4O_9$ and improvement of its thermoelectric properties by spark plasma sintering. *Journal of the American Ceramic Society*, 88(5):1337–1340, 2005.

[51] Daoqiang Lu, Quinn K Tong, and CP Wong. Mechanisms underlying the unstable contact resistance of conductive adhesives. *Electronics Packaging Manufacturing, IEEE Transactions on*, 22(3):228–232, 1999.

[52] Daoqiang Lu and CP Wong. Effects of shrinkage on conductivity of isotropic conductive adhesives. *International Journal of Adhesion and Adhesives*, 20(3):189–193, 2000.

[53] Daoqiang Lu and CP Wong. A study of contact resistance of conductive adhesives based on anhydride-cured epoxy systems. *Components and Packaging Technologies, IEEE Transactions on*, 23(3):440–446, 2000.

[54] David Keith Chalmers MacDonald and Donald Tuomi. Thermoelectricity: an introduction to the principles. *Journal of The Electrochemical Society*, 110(8):206C–206C, 1963.

[55] JB Maclachlan, WH Kruesi, and DJ Fray. Intercalation of copper into bismuth telluride. *Journal of materials science*, 27(15):4223–4229, 1992.

[56] Deepa Madan, Alic Chen, Paul K Wright, and James W Evans. Dispenser printed composite thermoelectric thick films for thermoelectric generator applications. *Journal of Applied Physics*, 109(3):034904–034904, 2011.

[57] Deepa Madan, Alic Chen, Paul K Wright, and James W Evans. Printed Se-Doped MA n-Type Bi_2Te_3 Thick-Film Thermoelectric Generators. *Journal of electronic materials*, 41(6):1481–1486, 2012.

[58] Deepa Madan, Zuoqian Wang, Alic Chen, et al. Enhanced Performance of Dispenser Printed MA n-type Bi_2Te_3 Composite Thermoelectric Generators. *ACS applied materials & interfaces*, 4(11):6117–6124, 2012.

[59] Deepa Madan, Zuoqian Wang, Alic Chen, Paul K Wright, and James W Evans. High Performance Dispenser Printed MA p-type $Bi_{0.5}Sb_{1.5}Te_3$ Flexible Thermoelectric Generators for Powering Wireless Sensor Networks. *ACS applied materials & interfaces*, 2013.

[60] Arun Majumdar. Thermoelectricity in semiconductor nanostructures. *Science*, 303(5659):777–778, 2004.

[61] Kirk Martinez, Jane K Hart, and Royan Ong. Environmental sensor networks. *Computer*, 37(8):50–56, 2004.

[62] David S McLachlan, Michael Blaszkiewicz, and Robert E Newnham. Electrical resistivity of composites. *Journal of the American Ceramic Society*, 73(8):2187–2203, 1990.

[63] GR Miller and Che-Yu Li. Evidence for the existence of antistructure defects in bismuth telluride by density measurements. *Journal of Physics and Chemistry of Solids*, 26(1):173–177, 1965.

[64] GR Miller, Che-Yu Li, and CW Spencer. Properties of Bi_2Te_3-Bi_2Se_3 Alloys. *Journal of Applied Physics*, 34(5):1398–1400, 1963.

[65] Melvin N. Miller. Bounds for Effective Electrical, Thermal, and Magnetic Properties of Heterogeneous Materials. *Journal of Mathematical Physics*, 10(11):1988–2004, 1969.

[66] Akira Mita and Shinpei Takhira. A smart sensor using a mechanical memory for structural health monitoring of a damage-controlled building. *Smart Materials and Structures*, 12(2):204, 2003.

[67] Don Morelli and Xu Lu. Natural mineral tetrahedrite as a direct source of thermoelectric materials. *Physical Chemistry Chemical Physics*, 15:5762, 2013.

[68] James E Morris and Johan Liu. Electrically conductive adhesives: A research status review. In *Micro-and Opto-Electronic Materials and Structures: Physics, Mechanics, Design, Reliability, Packaging*, pages B527–B570. Springer, 2007.

[69] Ce-Wen Nan. Physics of inhomogeneous inorganic materials. *Progress in Materials Science*, 37(1):1–116, 1993.

[70] C. Navone, M. Soulier, M. Plissonnier, and A.L. Seiler. Development of $(Bi,Sb)_2(Te,Se)_3$-Based Thermoelectric Modules by a Screen-Printing Process. *Journal of Electronic Materials*, 39(9):1755–1759, 2010.

[71] Joseph A Paradiso and Thad Starner. Energy scavenging for mobile and wireless electronics. *Pervasive Computing, IEEE*, 4(1):18–27, 2005.

[72] Bed Poudel, Qing Hao, Yi Ma, et al. High-thermoelectric performance of nanostructured bismuth antimony telluride bulk alloys. *Science*, 320(5876):634–638, 2008.

[73] Ravi Prasher. Thermal interface materials: historical perspective, status, and future directions. *Proceedings of the IEEE*, 94(8):1571–1586, 2006.

[74] Harish Ramamurthy, BS Prabhu, Rajit Gadh, and Asad M Madni. Wireless industrial monitoring and control using a smart sensor platform. *Sensors Journal, IEEE*, 7(5):611–618, 2007.

[75] John A Rogers and Zhenan Bao. Printed plastic electronics and paperlike displays. *Journal of polymer science part A: Polymer Chemistry*, 40(20):3327–3334, 2002.

[76] FD Rosi, B Abeles, and RV Jensen. Materials for thermoelectric refrigeration. *Journal of Physics and Chemistry of Solids*, 10(2):191–200, 1959.

[77] Shad Roundy, Paul Kenneth Wright, and Jan M Rabaey. *Energy scavenging for wireless sensor networks: with special focus on vibrations*. Springer, 2004.

[78] D. M. Rowe. *Thermoelectrics Handbook: Micro to Nano*. Taylor and Francis/CRC, Boca Raton, Florida, 2005.

[79] DM Rowe and Gao Min. Design theory of thermoelectric modules for electrical power generation. *IEE Proceedings-Science, Measurement and Technology*, 143(6):351–356, 1996.

[80] Farhad Sarvar, David C Whalley, and Paul P Conway. Thermal interface materials-A review of the state of the art. In *Electronics Systemintegration Technology Conference, 2006. 1st*, volume 2, pages 1292–1302. IEEE, 2006.

[81] Kevin C See, Joseph P Feser, Cynthia E Chen, et al. Water-processable polymer- nanocrystal hybrids for thermoelectrics. *Nano letters*, 10(11):4664–4667, 2010.

[82] Xun Shi, Jiong Yang, James R Salvador, et al. Multiple-filled skutterudites: high thermoelectric figure of merit through separately optimizing electrical and thermal transports. *Journal of the American Chemical Society*, 133(20):7837–7846, 2011.

[83] G Jeffrey Snyder and Eric S Toberer. Complex thermoelectric materials. *Nature materials*, 7(2):105–114, 2008.

[84] Amir M Sodagar, Gayatri E Perlin, Ying Yao, Kensall D Wise, and Khalil Najafi. An implantable microsystem for wireless multi-channel cortical recording. In *Solid-State Sensors, Actuators and Microsystems Conference, 2007. TRANSDUCERS 2007. International*, pages 69–72. IEEE, 2007.

[85] Z Starỳ, J Horak, M Stordeur, and M Stölzer. Antisite defects in $Sb_{2-x}Bi_xTe_3$ mixed crystals. *Journal of Physics and Chemistry of Solids*, 49(1):29–34, 1988.

[86] Daniel Steingart, Christine C Ho, Justin Salminen, James W Evans, and Paul K Wright. Dispenser printing of solid polymer-ionic liquid electrolytes for lithium ion cells. In *Polymers and Adhesives in Microelectronics and Photonics, 2007. Polytronic 2007. 6th International Conference on*, pages 261–264. IEEE, 2007.

[87] M Strasser, R Aigner, C Lauterbach, et al. Micromachined CMOS thermoelectric generators as on-chip power supply. *Sensors and Actuators A: Physical*, 114(2):362–370, 2004.

[88] Marc Strasser, Robert Aigner, Martin Franosch, and Gerhard Wachutka. Miniaturized thermoelectric generators based on poly-Si and poly-SiGe surface micromachining. *Sensors and Actuators A: Physical*, 97:535–542, 2002.

[89] Vivek Subramanian, Jean MJ Fréchet, Paul C Chang, et al. Progress toward development of all-printed RFID tags: materials, processes, and devices. *Proceedings of the IEEE*, 93(7):1330–1338, 2005.

[90] Kenichi Takahata and Yogesh B Gianchandani. A micromachined capacitive pressure sensor using a cavity-less structure with bulk-metal/elastomer layers and its wireless telemetry application. *Sensors*, 8(4):2317–2330, 2008.

[91] Ee Lim Tan, Wen Ni Ng, Ranyuan Shao, Brandon D Pereles, and Keat Ghee Ong. A wireless, passive sensor for quantifying packaged food quality. *Sensors*, 7(9):1747–1756, 2007.

[92] Terry M Tritt and MA Subramanian. Thermoelectric materials, phenomena, and applications: A bird's eye view. *MRS bulletin*, 31(03):188–198, 2006.

[93] Rama Venkatasubramanian, Edward Siivola, Thomas Colpitts, and Brooks O'quinn. Thin-film thermoelectric devices with high room-temperature figures of merit. *Nature*, 413(6856):597–602, 2001.

[94] Christopher J Vineis, Ali Shakouri, Arun Majumdar, and Mercouri G Kanatzidis. Nanostructured thermoelectrics: big efficiency gains from small features. *Advanced Materials*, 22(36):3970–3980, 2010.

[95] F. Völklein, V. Baier, U. Dillner, and E. Kessler. Transport properties of flash-evaporated $(Bi_xSb_x)_2Te_3$ films I: Optimization of film properties. *Thin Solid Films*, 187(2):253 – 262, 1990.

[96] Z Wang, A Chen, R Winslow, et al. Integration of dispenser-printed ultra-low-voltage thermoelectric and energy storage devices. *Journal of Micromechanics and Microengineering*, 22(9):094001, 2012.

[97] Brett Warneke, Matt Last, Brian Liebowitz, and Kristofer SJ Pister. Smart dust: Communicating with a cubic-millimeter computer. *Computer*, 34(1):44–51, 2001.

[98] J Weber, K Potje-Kamloth, F Haase, et al. Coin-size coiled-up polymer foil thermoelectric power generator for wearable electronics. *Sensors and Actuators A: Physical*, 132(1):325–330, 2006.

[99] I. Webman, J. Jortner, and M.H. Cohen. Thermoelectric power in inhomogeneous materials. *Physical Review B*, 16:2959–2964, 1977.

[100] Joel Wilson, Vikas Bhargava, Andrew Redfern, and P Wright. A wireless sensor network and incident command interface for urban firefighting. In *Mobile and Ubiquitous Systems: Networking & Services, 2007. MobiQuitous 2007. Fourth Annual International Conference on*, pages 1–7. IEEE, 2007.

[101] CP Wong and Raja S Bollampally. Thermal conductivity, elastic modulus, and coefficient of thermal expansion of polymer composites filled with ceramic particles for electronic packaging. *Journal of Applied Polymer Science*, 74(14):3396–3403, 1999.

[102] X. Xi, G. Matijasevic, L. Ha, and D. Baxter. Fabrication of Thermoelectric Modules using Thermoelectric Paste and an Additive Technology. *Thermoelectric Materials 1998- The Next Generation Materials for Small-Scale Refrigeration and Power Generation Applications*, 545:143–148, 1998.

[103] Osamu Yamashita, Shoichi Tomiyoshi, and Ken Makita. Bismuth telluride compounds with high thermoelectric figures of merit. *Journal of Applied Physics*, 93(1):368–374, 2003.

[104] JY Yang, T Aizawa, A Yamamoto, and T Ohta. Effects of interface layer on thermoelectric properties of a pn junction prepared via the BMA-HP method. *Materials Science and Engineering: B*, 85(1):34–37, 2001.

[105] Isamu Yashima, Hiroshi Watanave, Takayasu Ogisu, Ryouma Tsukuda, and Susumu Sato. Thermoelectric Properties and Hall Effect of $Bi_2Te_{3-x}Se_x$ Polycrystalline Materials Prepared by a Hot Press Method. *Japanese journal of applied physics*, 37:2472, 1998.

[106] WM Yim, EV Fitzke, and FD Rosi. Thermoelectric properties of Bi_2Te_3-Sb_2Te_3-Sb_2Se_3 pseudo-ternary alloys in the temperature range 77 to 300 K. *Journal of Materials Science*, 1(1):52–65, 1966.

[107] WM Yim and FD Rosi. Compound tellurides and their alloys for peltier cooling-A review. *Solid-state electronics*, 15(10):1121–1140, 1972.

[108] M. Zakeri, M. Allahkarami, Gh. Kavei, A. Khanmohammadian, and M.R. Rahimipour. Low temperature synthesis of nanocrystalline Sb_2Te_3 by mechanical alloying. *Journal of Materials Science*, 43(5):1638–1643, 2008.

[109] Stefano Zampolli, Ivan Elmi, Enrico Cozzani, et al. Ultra-low-power components for an RFID Tag with physical and chemical sensors. *Microsystem Technologies*, 14(4-5):581–588, 2008.

[110] B Zhang, J Sun, HE Katz, F Fang, and RL Opila. Promising thermoelectric properties of commercial PEDOT: PSS materials and their Bi_2Te_3 powder composites. *ACS Applied Materials & Interfaces*, 2(11):3170–3178, 2010.

[111] L.D. Zhao, B.-P. Zhang, J.-F. Li, M. Zhou, and W.S. Liu. Effects of process parameters on electrical properties of n-type Bi_2Te_3 prepared by mechanical alloying and spark plasma sintering. *Physica B: Condensed Matter*, 400:11 – 15, 2007.

[112] Li-Dong Zhao, Bo-Ping Zhang, Wei-Shu Liu, and Jing-Feng Li. Effect of mixed grain sizes on thermoelectric performance of Bi_2Te_3 compound. *Journal of Applied Physics*, 105(2):023704, 2009.